The Dissertation Committee for Mohamad A. Zeidan certifies that this is the approved version of the following dissertation:

DIGITALLY ASSISTED TEST METHODOLOGY FOR RF RECEIVERS

Committee:

Jacob A. Abraham, Supervisor

Ranjit Gharpurey, Co-Supervisor

Gaurab Banerjee

Susanta Sengupta

Ahmed H. Tewfik

Nur A. Touba

DIGITALLY ASSISTED TEST METHODOLOGY FOR RF RECEIVERS

by

Mohamad A. Zeidan, B.E.; M.S.E.

Dissertation

Presented to the Faculty of the Graduate School of

The University of Texas at Austin

in Partial Fulfillment

of the Requirements

for the Degree of

Doctor of Philosophy

The University of Texas at Austin

December 2012

Dedication

إهداء

To my dear parents, who strove to educate me.

إلى وَالِدَيّ العَزِيزَيْن اللَّذيْن جَاهَدا فِي تعليمي.

To my wife, my love, and my friend and companion on this challenging long journey.

إلى زَوْجَتِي، حَبِيبَتِي و صَدِيقَتِي وَ رَفِيقَتِي عَلَى هَذَا الدَّرْب الصَّعْب الطَوِيل.

To my son Amin and daughter Serene, who were born during this endeavor.

إلى وَلَدَيّ أمين و سيرين، الذيْنِ أبْصَرا النُورَ خِلالَ هذهِ الدِراسَة.

Acknowledgements

Pursuing a Ph.D. degree is a very challenging and demanding experience, it is life changing. During this pursuit and throughout my life, from childhood and school years through college and beyond, there were people who helped shape my personality. They instilled scientific curiosity in me, encouraged my love of tinkering and nurtured it into a dream of becoming an engineer. These are people without whom I would not have been able to accomplish what I did and I am grateful to them for the different ways in which they have supported me.

I cannot sufficiently convey my gratitude to my parents, Amin and Nabila Zeidan, for their extreme sacrifices, material and otherwise. Their striving to provide me with the best education they could, from early childhood and through college, is nothing short of exemplary. I was also lucky to have my siblings, Hanadi, Khaled, Dania, and Rana (all older than me) in my family; their unconditional love and support made my childhood years wonderful. I was not only allowed to, but actually encouraged to tinker, to disassemble and break things and try to fix them, and to learn from my own mistakes. I have always felt the presence of their support and prayers with me, wherever I went. On my long and challenging Ph.D. journey, there is perhaps no person who supported me more ardently and sacrificed more dearly, day-in and day-out, than my wife, my love, and my companion, Afaf Zeidan. For that, I will be forever grateful.

I was very lucky to work under the supervision of my advisor, Professor Jacob A. Abraham; I thank him for his consistent support, guidance, and understanding throughout the course of my research. Working under Professor Abraham's direction and being part of his research group was a complete privilege. I would like to thank my co-advisor,

Professor Ranjit Gharpurey for his patience and guidance, and for his technical feedback. Thanks to the dissertation committee members: Drs. Gaurab Benerjee, Susanta Sengupta, Ahmed Tewfik, and Nur Touba, for their ideas and feedback. Thanks also to Drs. Baker Mohammad and Bassam Jamil for their encouragement, advice, and support of my work. Thanks to the Electrical and Computer Engineering staff for their assistance, especially Ms. Melanie Gulick and Ms. Debi Prather.

From my childhood years and throughout college, I must thank Mr. Abdel-Basset Fakhoury ("Ammo Abed") for being the mentoring neighbor he was. His involvement in my childhood school years runs deep, from the "infamous" multiplication-table exercise that his daughter Maria and I were often "coerced" to solve, to his un-orthodox fraction-teaching methods ("hmar w nos, w rebe' hmar, addeish?"). Abdel-Basset, Bozenna (aka "Bouba"), and Maria Fakhoury were not merely neighbors, they were family.

From my high-school years, I would like to thank my math teachers Mrs. Souad Hakim and Mr. George Issa, my physics teacher Dr. Kamel Dallal, and my chemistry teachers Mrs. Hoda Dbeibo and Mr. Assi Assi. They were more than teachers, they were educators. Their teaching methods increased my love of math and sciences, and their influence on my academic choices cannot be overstated.

From my undergrad years, I thank Dr. Ayman Kayssi, Dr. Shahwan Khoury, and Dr. Fuad Mrad. They each left a unique fingerprint on my engineering background and I am proud to have been a student in their classes.

Throughout my part-time studies, I was lucky to have wonderful colleagues at my full-time workplace. I especially thank Mr. Ziyad Doany and Mr. Michel Haddad for bringing me to the analog side of engineering and putting me on the "right track". Mr.

Ziyad Doany's mentoring during my internship at National Instruments equipped me with a load of analog tricks and techniques that would go a long way and help me throughout my career. I thank Mr. Ed Lowenstein, Mr. Jaffar Shah, Mr. George Topala, and Mr. Hon Yee for their insightful discussions, mentorship, and technical feedback on various topics throughout my career.

I would like to thank my management at Qualcomm Incorporated, particularly Mr. Kenneth Barnett, Mr. David Love, Mr. Stephan Bar, and Mr. Michael Ellison, and my current management in National Instruments, especially Mr. Jin Bains, Mr. Jason White, and Mr. Richard Maslowski, for their support of my research and work and for their understanding. I especially thank Mr. Richard Maslowski for taking the time to review and proof-read this dissertation.

Finally, foremost I thank God, The Loving and The Merciful, for the tremendous gifts he bestowed upon me, for giving me the mental and physical strength to go on with my studies, and for blessing me with the opportunity to meet all the wonderful people I mentioned above.

Digitally Assisted Test Methodology for RF Receivers

Mohamad A. Zeidan, Ph.D.

The University of Texas at Austin, 2012

Supervisors: Jacob A. Abraham and Ranjit Gharpurey

Addressing the high cost of RF instrumentation has motivated significant research activity, where researchers have proposed various non-standard and alternative test methods of RF circuits to mitigate high test cost. This dissertation describes a test methodology for RF receivers, whereby simple digital circuits comprise the core of the otherwise complex and costly broadband RF/analog signal generation. The proposed test methodology relies on a digital clock, commonly available to RF ICs for the purpose of digital communication, to generate the broadband RF stimulus needed for the receiver analog tests. The test method also utilizes commonly available baseband signal digitization (on-chip or off-chip) to acquire the baseband signal. It then relies on sophisticated, but inexpensive, signal processing to extract and compute standard RF

performance parameters, like gain, noise figure (NF), and input-referred third-order intercept point (IIP3). In addition, the test method can extract important baseband (BB) parameters like the BB filter 3 dB bandwidth (BW), filter rejection at specific BB frequencies, or the BB filter profile.

The motivation behind the proposed test methodology can be categorized as both architectural and cost reduction-oriented. Architecturally, the proposed test method aims at shifting the complexity involved in the test of RF receivers from the hardware (input) RF signal generation side to the signal processing done on the (output) baseband side. The process of shifting the complexity from the hardware design side to the signal processing side involves significant complex and sophisticated analysis, which is part of this dissertation. Cost-wise, the proposed test methodology enables the use of digital automatic test equipment (ATE) with limited baseband capability, instead of the full standard RF testers. Such a step reduces the initial tester cost and impacts the cost/sec figure spent on test for the life of the ATE tester, thus leading to test cost reduction.

Table of Contents

List of Tables

List of Figures

1 INTRODUCTION

1.1 Standard Testing of RF Receivers

RF receiver integrated circuits (IC) go through numerous tests during production to guarantee their performance. Such screening is necessary to reduce the number of defects at the final system-level assembly, where a non-functional or defective chip can render the whole system or device defective. Although the test sequence that an RF receiver undergoes in production can be long and composed of many steps at different settings, gain-states, and channel frequencies, it is ultimately comprised of just a few tests that aim to acquire a measure of performance of the RF receiver sensitivity, linearity, and gain. This evaluation of the test sequence consciously leaves out basic and necessary tests like the ones that check for correct digital communication with the chip, proper locking of the PLL, and others. Sensitivity describes the receiver's ability to detect small signals. The smaller the signals that the receiver can detect, while satisfying a minimum signal-to-noise ratio, the better the sensitivity. Linearity, on the other hand, describes the receiver's ability to cope with large signals, without sacrificing sensitivity performance or introducing spurious in-band components. Finally, gain on the receiver is understood as conversion gain, from the ratio of the receiver's baseband output to the receiver's RF input (more on receiver operation in Section 2.2). Several tests can be run to check for the sensitivity, linearity, and gain performance of the DUT, but commonly used ones are noise figure (NF), input-referred third-order intercept point (IIP3), and gain. The detailed procedure for each one of these tests is covered in Section 2.3.

1.2 Literature Overview

The high cost of RF instrumentation presents a major challenge in wireless system research and product development. Many researchers have investigated new methods of addressing RF test. Some have addressed the problem of signal generation, utilizing digital circuitry and sigma-delta modulators with low-pass [1], band-pass [2], and more recently with high-pass schemes to allow the generation of frequencies close to and beyond f_s the Nyquist rate [3] [4]. This approach is promising for RF signal generation, but it requires sophisticated modulator design and the presence of long bit streams. Moreover, unless the signal is limited to $f_s/2$, the natural loss in the higher Nyquist bands as well as the simultaneous presence of the first Nyquist band signal need to be addressed properly. Other researchers have addressed the issue of measurement and data acquisition through embedding RF power sensors [5] or amplitude detectors [6] to offer on-chip RF amplitude measurement, assisting in gain, linearity, or compression measurements. These approaches can also be utilized for the refinement of RF BIST, but they do not offer significant cost or area reduction, especially when it comes to RF signal generation. Some researchers have used alternate methods where complex RF specifications are predicted based on spectral features [7] or the response to specially designed stimuli that are applied to the Device Under Test (DUT) [8] [9], thereby, inferring the specifications rather than directly measuring them. This approach, while effective, sometimes requires a sophisticated and flexible crafting of external stimuli as well as knowledge of the behavioral models for the DUT. Signature-based tests using transient inputs with synchronized digitization of the DUT response have also been reported [10] [11], but they also rely on inferring performance parameters as opposed to directly measuring them. Test schemes, including built-in ones, with simplified hardware and sophisticated

signal processing have been attempted, but the approaches targeted low frequency analog circuits [12] or were specific to narrowband RF components and required stimulus band-pass filters [13]. Loopback test schemes have also been addressed, where only baseband signals are considered [14]. However, while loopback schemes can be employed in transceiver DUTs, they cannot be used for testing receiver-only DUTs like those used in broadcast applications. Moreover, having a method for testing broadband receivers using minimal RF hardware can be utilized in conjunction with loopback test schemes to facilitate and verify the receiver-transmitter parameter decoupling operation.

1.3 Motivation

The proposed RF receiver test methodology involves a system that comprises RF broadband multitone (MT) signal generation and characterization, baseband signal acquisition, and signal processing. Architecturally, the method aims to simplify the otherwise complex circuits needed for the RF signal generation at the cost of complicating the signal processing done on the acquired low-frequency baseband signal. The reasoning behind such a scheme is that the baseband signal processing, though complex, is less expensive. Moreover, the complex analysis that forms the basis for the signal processing is presented in this dissertation, thus significantly reducing the signal processing implementation complexity in general. On the other hand, while the cost reduction is ultimately measured in "dollars", it can be manifested in different ways. One aspect of cost reduction is related to the initial ATE tester cost, which dictates what the cost/sec value on the tester is, over the number of years of the tester service. Being able to use a basic digital tester with limited baseband capability instead of having to use a full

RF tester reduces the initial tester cost, and thus the equivalent cost for every second of test. Furthermore, aside from the reduction of the cost per unit time, the proposed methodology may help reduce the test time itself, thus resulting in further, multiplied, cost savings. The test time reduction may be attributed to the increased capability of adding multiple test sites with little or no effect on tester cost because of the additional test sites requiring only simple baseband capability. Furthermore, test time reduction may also be partially attributed to the fact that the MT signal generation scheme does not require frequency tuning, and thus eliminates the tuning and settling times associated with traditional RF signal generators. Finally, in the case of on-chip implementation of the signal generation scheme for BIST applications, the proposed methodology offers reduced area (cost) compared to traditional broadband signal generation schemes.

2 BACKGROUND

2.1 RF Signal Generation Methodology Fundamentals

In the proposed methodology we employ a periodic impulse train as the input waveform to the DUT. A periodic impulse train can be expressed as a Fourier series that is characterized by a discrete uniform multitone spectrum that extends to infinity in the frequency domain and has a frequency tone spacing that is the inverse of the time-domain signal period, [15], as shown in Fig. 2.1. With the periodic impulse (Comb) signal period being T, the corresponding multitone spectrum will have tones at nf_{clk}, where $f_{clk} = 1/T$. Mathematical analysis and practical aspects of this generation scheme are covered in detail in Chapter 3 under RF Signal Generation.

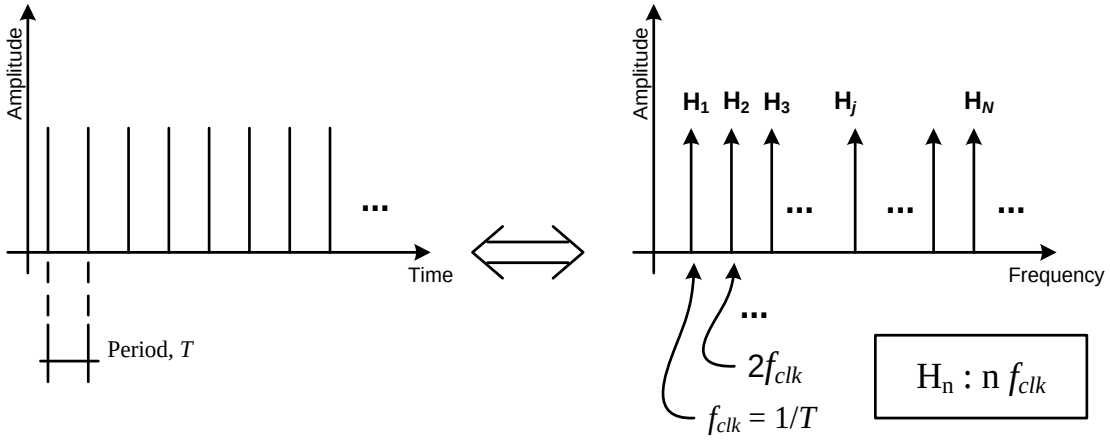

Fig. 2.1: Correspondence of time-domain periodic impulse (Comb) signal and frequency-domain multitone spectrum

2.2 RF Receiver Fundamentals

In this section we cover the RF receiver basics and fundamentals. We start by going over the receiver building blocks, and then we cover the general receiver operation before finally discussing the receiver's specific operation on a MT signal.

2.2.1 RF Receiver Building Blocks

At a high level, we consider the RF receiver's block diagram as consisting of 4 sub-blocks as shown in Fig. 2.2. The first is the synthesizer block that contains a controlled local oscillator (LO) that can be tuned to the center of any channel within the desired frequency band. The second is the RF front-end block, symbolized by a low-noise amplifier (LNA), whose task is to amplify the RF input signal with minimal addition of noise. The third block is the RF mixer, whose task is to multiply the amplified incoming RF signal with the LO, thus resulting in shifting the RF signal in frequency by ± the LO frequency. The fourth and last block is the output baseband filter block, whose task is to filter out the unwanted neighboring baseband channels, in addition to filtering out the much higher frequency components. Any variable gain functionality, as required is assumed to be embedded within the LNA and baseband filters.

2.2.2 RF Receiver General Operation

From the RF performance characterization perspective, the RF receiver/downconverter is a two-port device, with one RF input port and one baseband (BB) output port, where the baseband output port is composed of an in-phase (I) component and a quadrature (Q) component, as shown in Fig. 2.2. Unlike simpler RF or analog non-frequency-translating devices, the RF receiver's input and output signals can be at significantly different frequencies. The RF input port accepts signals across a wide range of frequencies and whose spectrum often includes multiple communication

channels within the receiver's bandwidth. The baseband port provides relatively low frequency signals, the highest frequency of which corresponds to half the bandwidth of a single channel, assuming direct downconversion. Downconversion is the process of capturing the information contained in a single desired channel in the RF spectrum and frequency translating it to baseband. The downconversion process starts by tuning the LO to a center frequency of a specific RF channel. The incoming RF signal then gets multiplied (mixed) with the LO, resulting in frequency translation of the RF signal band to DC or baseband. And finally, the baseband filter takes care of filtering out unwanted out-of-band signals.

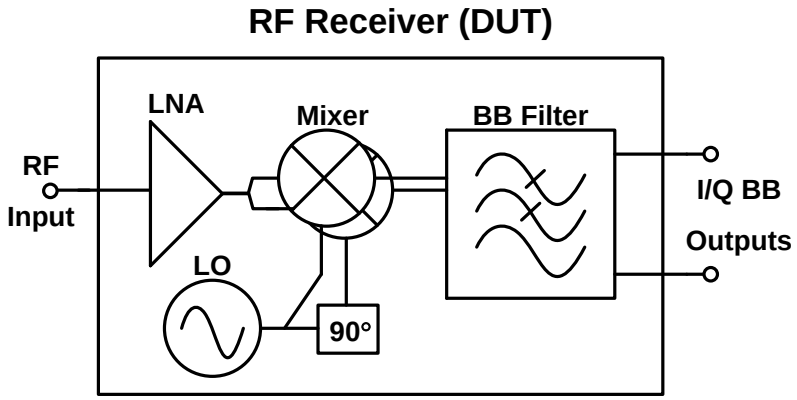

Fig. 2.2: RF receiver block diagram

2.2.3 RF RECEIVER OPERATION ON A MT SIGNAL

2.2.3.1 Overview

Consider the scenario where the MT signal described in Fig. 2.1 is used as the input to the DUT as shown in Fig. 2.3. Tuning the DUT LO to within, say 'x' kHz of one of the RF signal tones (termed Hj), results in a tone at the baseband frequency of 'x' kHz.

For a DUT baseband filter bandwidth (BB Filter BW) that is larger than 'x' and smaller than the RF MT signal tone spacing (i.e. 'x' < BB Filter BW < f_{clk}), the tone Hj shows up as the primary baseband signal while other tones are attenuated by the DUT BB filter. (See Fig. 2.3)

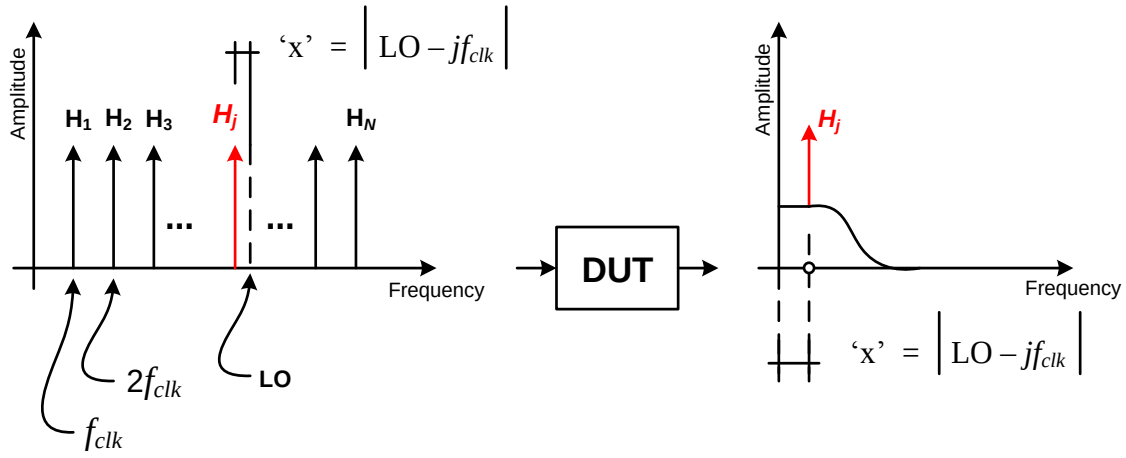

Fig. 2.3: DUT operating on the RF MT signal

2.2.3.2 Contrast to Traditional Operation

To understand the difference between the traditional use of a MT signal (an impulse or a periodic impulse signal) in the characterization of simple non-frequency-translating DUTs and in the proposed characterization of a receiver, we first consider Fig. 2.4, which demonstrates the traditional utilization of an impulse signal. In Fig. 2.4, the time domain perspective is shown on top, where the DUT (LNA or LPF…etc) takes an impulse signal as an input and generates a modified version of the impulse signal. The modification can consist of scaling as well as changing the shape of the impulse signal, e.g. by broadening out the impulse due to the limited device bandwidth.

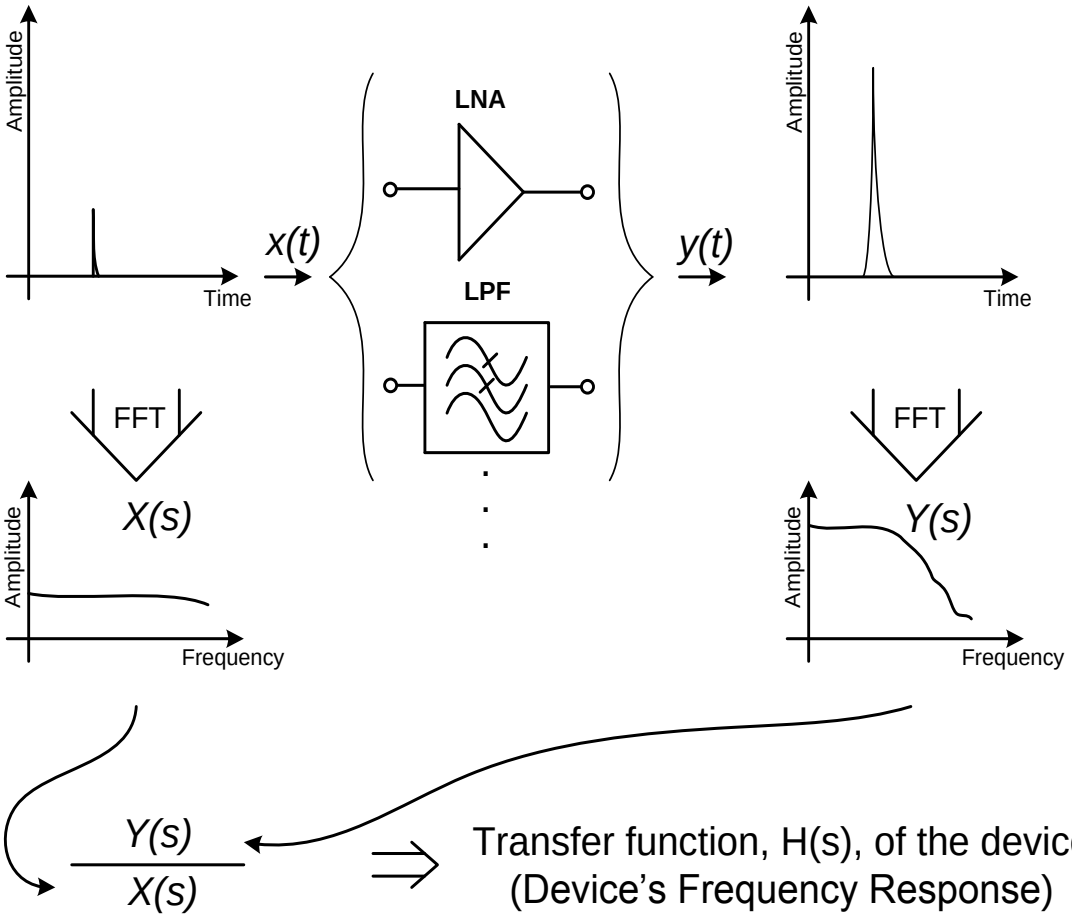

Fig. 2.4: Traditional characterization use of an impulse signal

Applying an FFT on the time-domain signals, at both the input and output, yields the respective spectra of the input and output signals. The input impulse signal spectrum is ideally perfectly flat with infinite frequency response; practically it is finite, but still flat with high frequency content relative to the output spectrum of the DUT. Dividing the output frequency response by the input frequency response yields the DUT transfer function, which is typically the characterization goal. On the other hand, we now consider Fig. 2.5, demonstrating the use of the same impulse signal on an RF receiver DUT.

Starting with the impulse signal spectrum, and knowing both where the DUT LO is tuned to within that spectrum, and how big the DUT BB filter BW is, we can decisively point out the portion of the spectrum that gets downconverted to baseband. Notice that the spectrum within the BB BW shown in *X(s)* (between the dashed red lines) is divided to two portions by the LO. Both portions get downconverted and overlap in the baseband spectrum shown in *Y(s)*. Moving from the frequency domain to the time domain, shown on top in Fig. 2.5, one can clearly see the contrast to the traditional use of the impulse signal. The output signal is not an impulse signal in nature, but a baseband signal representing only the portion of the impulse spectrum that got downconverted through the receiver to BB.

In the case of a MT signal (a periodic impulse), where the LO is tuned next to one of the MT tones, the portion of the spectrum within the BB BW is only that single-tone.

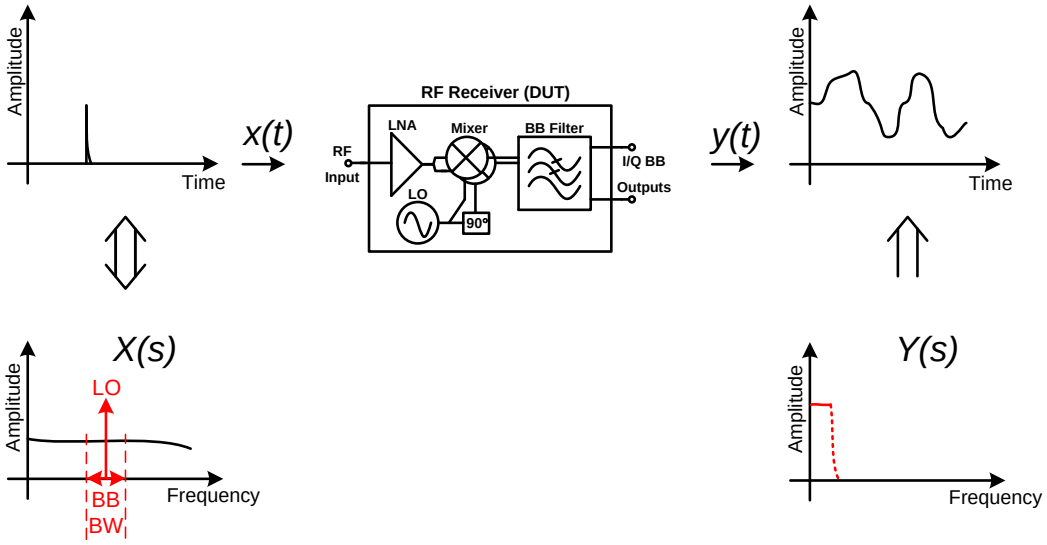

Fig. 2.5: Use of an impulse in the characterization of a receiver

Knowing the RF signal tone levels and measuring the downconverted tone level at the DUT baseband output, one would be able to calculate the conversion gain of the DUT at the frequency of the downconverted tone. Consequently, measuring the DUT gain at a broad range of RF frequencies is possible by tuning the DUT LO close to tones that correspond to these frequencies.

2.3 Standard RF Receiver Tests

2.3.1 TEST PROCEDURES

In this section, the standard procedure for performing receiver measurements is described; specifically, the measurements covered are gain, NF, and IIP3.

2.3.1.1 Gain

As alluded to in Section 2.2.3.2, the gain measurement involves providing the RF receiver DUT with a single tone at the desired RF frequency of characterization. Knowing what the input tone level is to a matched load in dBm, and assuming the DUT's single-tone baseband output is measured in V_{RMS} (Volts Root-Mean-Square) into a 50Ω load, the conversion gain in dB can be computed as follows:

$$Gain\,(dB) = 10Log_{10}\left(\frac{V_{RMS_{BB}}^2}{Z_0} \times \frac{1}{10^{-3}}\right) - P_{IN} \tag{2.1}$$

where $V_{RMS_{BB}}$ is the RMS voltage of the single-tone measured at the DUT's output, P_{IN} is the input power (tone level) in dBm, and Z_0 is the characteristic impedance, a property that relates to the ratio of the distributed inductance and capacitance in the signal operating medium. The common characteristic impedance for RF systems is 50 Ω, for audio/video systems is 75 Ω, and in free-space is $\sqrt{\mu_0/\varepsilon_0} \approx 377\Omega$. This procedure,

while standard and typically accurate for an impedance matched DUT (to within one or two tenths of a dB), is not a calibration-grade procedure, because it assumes that knowledge of the input power for a matched load would apply to the DUT with no error. A calibration-grade procedure, actually measures the input to the DUT using a calibration-grade power splitter (such as the one described in [16]), a calibration-grade power sensor (such as the ones described in [17], [18], or [19]), in addition to also measuring the output power (or voltage). Having touched on the difference between the standard and calibration-grade procedures, we emphasize that the standard procedure is the commonly used one on automatic test equipment (ATE) testing of RF IC receivers, while the calibration-grade procedure is typically used for instrumentation purposes (i.e. calibration of the instruments and ATEs). In our study and experimental work, we shall refer to the standard procedure for evaluating the proposed method's accuracy.

2.3.1.2 Noise Figure

The Noise Figure of a receiver is a measure of the noise that the receiver inherently adds to the incoming signal, and thus it is a measure of the degradation it causes to the signal-to-noise ratio (SNR). Similar to gain, NF can be computed in different ways, some more accurate than others. An accurate method to measure NF is the Y-Factor method, in which NF is calculated from two relative measurements done involving a calibrated noise source; details of the Y-Factor method can be found in [20] or [21]. Another method, often referred to as the gain-method [20], is used to measure NF by finding the noise density (in dBm/Hz) at the receiver input and comparing it to the fundamental noise floor expected at the input of a perfectly matched ideal receiver in a 1 Hz noise bandwidth. Some methods go to the extent of extracting the DUT noise density from below the measuring instrument's noise floor, by adding a noise floor calibration

step [22]. Regardless of the method used, quantifying NF requires the capability to measure noise density or to integrate noise power in a given bandwidth, which is discussed in detail in Section 3.3.3. In this dissertation, the gain method is one used as the standard reference method. Below are the details necessary for conducting the measurement procedure.

The theoretical fundamental (thermal) noise floor ($TFNF$) is expressed as:

$$TFNF = 10\log_{10}\left(\frac{KTB}{10^{-3}}\right) \tag{2.2}$$

where K is Boltzmann's Constant = 1.38×10^{-23} in SI units of Joules/K, T is temperature in K, and B is the noise bandwidth in Hz. For a NF standard measurement temperature of 290 K, the fundamental noise floor is -173.975 dBm in a 1 Hz bandwidth (Note that -174 dBm/Hz is more commonly used as a rule-of-thumb).

To measure the receiver's noise density at its input, a common method is to measure it at the baseband output and then use the conversion gain to refer it back to the receiver's input as follows:

$$ND_{Input} = ND_{Output} - G - 10\,Log_{10}(2) \tag{2.3}$$

where ND is the noise density in dBm/Hz and G is the receiver's conversion gain in dB. The subtraction of $10\,Log_{10}(2)$ or 3.01 dB is specific to direct-conversion receivers, to compensate for the fact that for such receivers, the receiver's output noise density reflects a doubling that occurs from the folding of the RF channel spectrum, as described in Section 2.2.3.2, when considering either of the I or Q channels separately. This procedure assumes that the signal is present at only one side of the LO, and that the noise of the image (other side of LO) is equal to that on the signal's side. The standard measurement,

thus, is technically a double side-band noise measurement emulating a single side-band one, and it is commonly understood as such in direct conversion or single-stage conversion receiver literature. It is worth noting that the input-referred noise-density measurement's accuracy is dependent on the accuracy of the gain measurement itself.

Knowing ND_{Input} from (2.3) and $TFNF$ from (2.2), NF can be expressed as:

$$NF\ (dB) = ND_{Input} - TFNF = ND_{Output} - G - 3.01 - TFNF \tag{2.4}$$

For practical purposes, the gain-method is more commonly used on ATEs for testing RF IC receivers, partially because it does not require a switching scheme to multiplex and connect the receiver's input to a calibrated noise source at one time and to a signal source at another. The switching mechanism would add its own anomalies and can defeat the purpose of a more accurate test methodology.

2.3.1.3 Input-Referred Third-Order Intercept Point

Input-Referred Third-Order Intercept Point, commonly abbreviated as IIP3 or ITOI, is a measure of the RF receiver's linearity. IIP3 is measured in dBm; the higher the IIP3 value, the better and more linear the DUT is. A standard method of characterizing IIP3 of a DUT is by presenting a two-tone signal centered at the desired RF frequency at its input, where the tones' levels are usually equal and where the frequency difference between the tones is relatively small and comparable to, but smaller than, the channel or BB filter BW. The procedural calculation of IIP3 is as follows:

$$IIP3\ (dBm) = \frac{3\,TT_{Output} - IMD_{Output}}{2} - G \tag{2.5}$$

where TT_{Output} is the average two-tone signal baseband output level in dBm, IMD_{Output} is the average baseband output level of the Inter-Modulation Distortion (IMD) tones in

dBm, and G is the receiver's conversion gain in dB. The two IMD tones are located to the left main tone and to the right of the right main tone, each spaced from the closest main tone by the frequency difference between the main tones, as illustrated in Fig. 2.6.

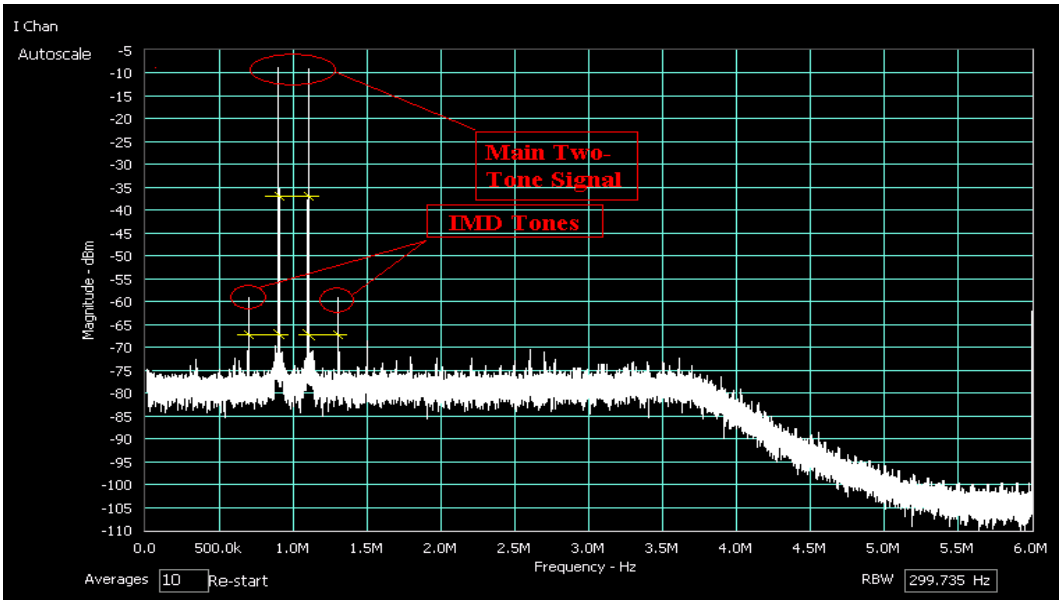

Fig. 2.6: Two-Tone and IMD signals as measured at DUT's baseband

2.3.2 TEST FUNDAMENTALS

This section covers the underlying principles of the tests discussed in Section 2.3.1 and touches on the fundamentals relating to the tested parameters.

2.3.2.1 Gain

2.3.2.1.1 Conversion Gain

In the case of an RF receiver DUT, the term gain implicitly indicates two things. Firstl gain indicates frequency conversion, as in "conversion gain", and second it indicates linearity, as in "linear gain". In the analysis that follows, as well as in the rest of this dissertation, frequency translation or conversion is considered understood, with the

input signal being an RF signal of frequency from a few MHz to many GHz, and the output signal being a baseband frequency that is typically limited from a few MHz to a few tens of MHz.

2.3.2.1.2 Linear and Non-Linear Gain

Let Y be the DUT baseband output, which includes linear and non-linear gain components as shown in (2.6). α_0 represents non-input related output signals (e.g. DC offset, noise, residual spurs…etc), α_1 represents the small-signal linear gain, and α_2 and α_3 are the considered non-linear gain components.

$$Y = \alpha_0 + \alpha_1 X + \alpha_2 X^2 + \alpha_3 X^3 \tag{2.6}$$

For a single-tone input $X = A\sin(w_1 t)$, the output Y is evaluated as:

$$Y = \alpha_0 + \alpha_1 A\sin(w_1 t) + \alpha_2 A^2 \sin^2(w_1 t) + \alpha_3 A^3 \sin^3(w_1 t) \tag{2.7}$$

But,

$$\sin^2(w_1 t) = \frac{1 - \cos(2w_1 t)}{2} \tag{2.8}$$

And,

$$\sin^3(w_1 t) = \frac{3\sin(w_1 t) - \sin(3w_1 t)}{4} \tag{2.9}$$

Substituting (2.8) and (2.9) into (2.7), we arrive at the expression for Y shown in (2.10) below.

$$Y = \left(\alpha_0 + \frac{\alpha_2 A^2}{2}\right) + \left(\alpha_1 A + \frac{3\alpha_3 A^3}{4}\right)\sin(w_1 t) - \frac{\alpha_2 A^2}{2}\cos(2w_1 t) - \alpha_3 A^3 \sin(3w_1 t) \tag{2.10}$$

The expression of the baseband output Y shown in (2.10), includes the main content at the expected frequency w_1 as well as signals resulting from the harmonic generation of w_1. Performing the gain measurement as described in Section 2.3.1.1 and using (2.1) assumes that the baseband signal is specifically a single-tone. In reality, even if the baseband signal is dominated by a single-tone, it contains other signals as well, such as noise. The gain measurement requires the ability to discern and extract single-tone information as detailed later on in Section 3.3.2. However, even if we zoom in on only the single-tone information in Y, as expressed in (2.10), we not only get the baseband output resulting from the linear gain, but also that due to non-linear gain. Considering only the single-tone content at w_1 of the baseband output, the gain of the DUT can be expressed as,

$$Gain = \frac{\alpha_1 A + \frac{3\alpha_3 A^3}{4}}{A} = \alpha_1 + \frac{3\alpha_3 A^2}{4} \tag{2.11}$$

Or in dB as follows:

$$Gain(dB) = 20Log_{10}\left(\alpha_1 + \frac{3\alpha_3 A^2}{4}\right) \tag{2.12}$$

The gain expressed in (2.12) is what one measures in reality when attempting to measure the linear gain. There is a third-order non-linear gain component whose frequency is that of the linear gain output that is added to the theoretical linear gain expressed in (2.13).

$$Gain_{Linear}(dB) = 20Log_{10}(\alpha_1) \tag{2.13}$$

2.3.2.1.3 Practical Forgiveness of Gain Measurement

The measured gain from (2.12) is typically designed to be close to the theoretical linear gain expressed in (2.13) over the signal range specified by the system. Consider the

following example, where the values are actual and taken from a real DUT that was characterized during the work of this dissertation. For a DUT whose $|\alpha_1| = 452$ and $|\alpha_3| = 269{,}000$ at a given frequency, one can compute the theoretical linear gain to be 53.1 dB, independent of the input signal level. The measured gain, on the other hand, is dependent on what the input signal is, as expressed in (2.12); the graph below shows two plots, one for the theoretical linear gain, which as expected reflects a flat constant level of ~53.1 dB, and a second for the measured gain as it changes versus the input signal level.

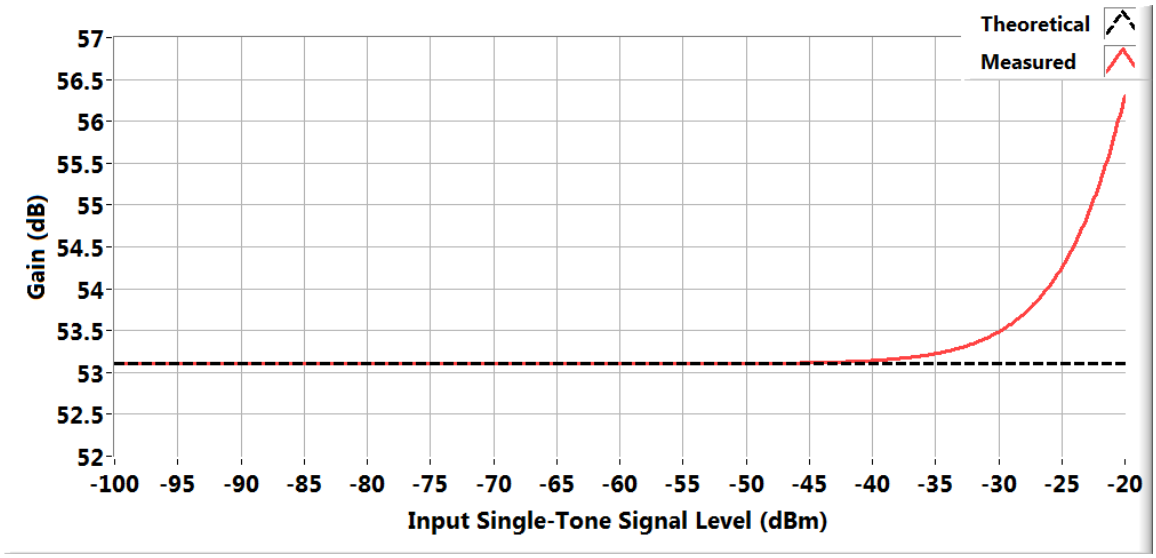

Fig. 2.7: Measured gain compared to theoretical linear gain vs. the input single-tone signal level

As one can see from Fig. 2.7, the design ensures that the measured gain remains to within 0.04 dB of the theoretical linear gain up to an input single-tone level of -40 dBm, which given the DUT gain, corresponds to an output baseband level of +13.1 dBm. In CMOS receiver DUTs using state-of-the-art technology nodes, an output of +13.1 dBm is a high number assuming a 50 Ω output. Signal compression or even DUT output stage saturation can take place before such a level is achieved. This is especially true if the

DUT is configured for high-sensitivity, as is this DUT, with a gain as high as 50 dB. For the applications considered here, a DUT whose gain is in the neighborhood of 50 dB may employ a signal level of less than -70 dBm. However, depending on the DUT's linearity, signals in the -80 dBm to -100 dBm range may be preferred. For an input of less than -70 dBm, the difference between measured gain and theoretical linear gain is less than a single thousandth of a 1 dB, which is why the measured gain is considered to be the linear gain, as long as the input single-tone level does not saturate or compress the DUT.

2.3.2.2 Noise Figure

2.3.2.2.1 Thermal Noise

Noise, otherwise understood as thermal or Johnson-Nyquist noise, is a random signal that results from the random motion of electrons at temperatures above absolute zero (0 K). While noise is typically inherent to the input signal of a receiver DUT, NF of a receiver quantifies the noise that the DUT adds to the signal, or in other words it quantifies the degradation in the signal quality or signal-to-noise ratio. The procedural calculation for noise figure presented in Section 2.3.1.2, in conjunction with the details on noise density evaluation discussed further ahead in Section 3.3.3, suffices for performing the NF measurement. However, below are some notes on the conditions that influence the accuracy of the NF measurement.

2.3.2.2.2 The Effect of the Source Used in Gain-Method

Because NF is generally tied to and meant to measure thermal noise, care should be taken when performing the measurement. This is especially true when using methods other than the standard Y-Factor method, where a signal can be present during the evaluation of noise density, even if outside the direct noise integration bandwidth. If the single-tone input signal used to compute the gain, as part of the gain-method, is not

turned off during noise density evaluation, then it becomes necessary to verify two things, in addition to making sure that the single-tone is outside of the integration bandwidth or that the single-tone bins are notched out and not considered when calculating the integrated noise power. First, it is necessary to ensure that the noise floor of the input signal itself is not dominating or contributing to the integrated noise density at the DUT output other than what a matched 50 Ω termination contributes, within the matching constraints that are discussed in detail next, in Section 2.3.2.2.3. This is not typically challenging because of the signal levels used in receiver testing, where for the case considered here, -90 dBm or -100 dBm is a common signal level; at such levels it is not uncommon to have zero excess noise and have the source's output noise floor be limited to what the fundamental noise floor is for the specific source output impedance. Second, it is necessary to ensure that the band range over which the noise is integrated is farther out from the single-tone signal frequency, enough for the single-tone signal's phase noise not to "leak" into the noise integration bandwidth. Phase noise close to the single-tone is composed of flicker $(1/f)$ noise and higher order $1/f^n$ noise. At sufficiently large spectral distance from the single-tone, the phase-noise becomes dominated by thermal noise. While the single-tone's phase noise at baseband can be dominated by or resulting from the DUT's LO phase noise after mixing, and is thus a property of the DUT, it is not appropriate to roll its effect in the noise figure measurement, which strictly relates to thermal noise.

2.3.2.2.3 The Error Due to Source Mismatch

As mentioned earlier, the source that is connected to the input of the receiver DUT is supposed to emulate a perfect 50Ω source, as only then the $TFNF$ would be exactly as found to be in Section 2.3.1.2, for a 50Ω DUT. In this section, the

mathematical analysis quantifying the NF error due to source impedance deviation from a perfect 50Ω, and thus due to the error in the used $TFNF$ value, is presented, and the results of a mathematical simulation that uses the latter analysis are used to demonstrate the error range involved, given practical source impedance value ranges.

Fig. 2.8 shows the signal source-DUT interface as it pertains to the "delivery" of the "noise signal", Vs. The value of $TFNF$ is derived from the thermal noise of the source resistance, Rs, the real part of the source impedance, Zs. The ideal DUT input impedance is modeled as a noiseless 50Ω resistor. The thermal noise generated within the source resistance is presented in (2.14)

$$Vs = \sqrt{4KTBRs} \tag{2.14}$$

where, K, T, and B are as previously defined for (2.2) in Section 2.3.1.2, Rs is the real part of the source impedance Zs, and where Vs is in $V_{RMS}/\sqrt{Hz}$. Performing the voltage division between the source impedance and the ideal DUT 50Ω input resistor, to compute the noise voltage delivered to the DUT results in $V_{Noise\ DUT}$ as shown in (2.15).

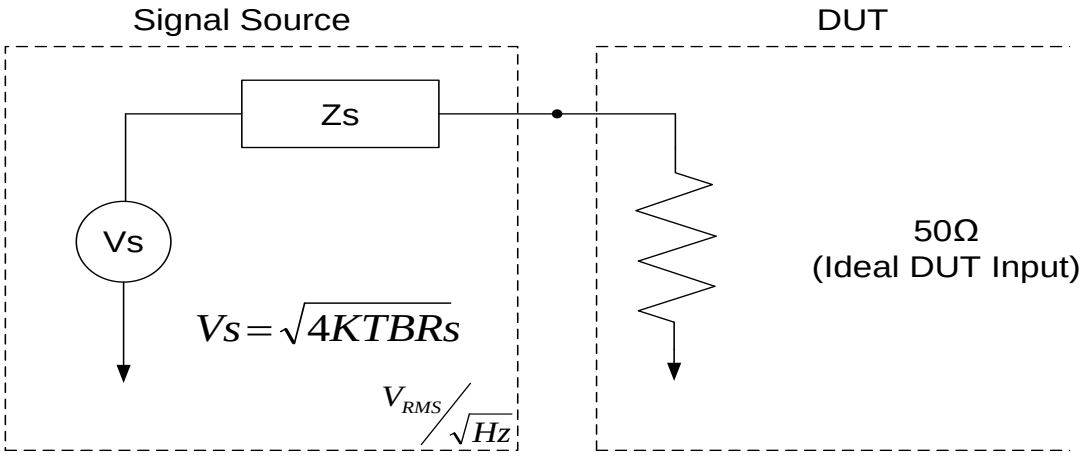

Fig. 2.8: Noise Delivery from Signal Source to DUT

$$V_{Noise\,DUT} = \frac{50}{Zs + 50}\sqrt{4KTBRs} \tag{2.15}$$

The noise power density delivered to the DUT, in dBm/Hz, can be computed in terms of Zs (and its real part Rs) from the delivered noise voltage as follows, where B is 1 Hz, T is 290°K, and K is $1.3806503 \times 10^{-23}$ Joules/°K.

$$\begin{aligned} P_{Noise_{DUT}} &= 10Log_{10}\left(10^3 \frac{V^2_{Noise_{DUT}}}{50}\right) \\ &= 10Log_{10}\left(2 \times 10^5 \frac{KTBRs}{(Zs + 50)^2}\right) \end{aligned} \tag{2.16}$$

The error in NF gain-method measurement resulting from the computation using the ideal $TFNF$ instead of the delivered noise from the actual source can be assessed by computing the delivered noise for the particular source impedance and then comparing it to the ideal $TFNF$. A mathematical simulation was built towards this end, and the source impedance Zs was swept based on a practical range of associated Voltage Standing Wave Ratio (VSWR) or Reflection Coefficients (Γ). Fig. 2.9 and Fig. 2.10 show the noise density (or $TFNF$) at the input of an ideal DUT and the error in $TFNF$ compared to ideal, respectively, versus the source impedance real and imaginary parts, which correspond to a VSWR that ranges from 1:1 (ideal) to ~ 2:1, or a |Γ| that ranges from 0 (ideal) to 0.33 with swept phase. A VSWR of 2:1 is not particularly good, per se, and thus it is worse than most typical source impedances in the realm of 50Ω systems, and it corresponds to a return loss of around 9.5 dB. Even with a source impedance that is as bad as having a VSWR of 2:1 or return loss of 9.5 dB, the error in NF or $TFNF$ still does not exceed 0.5 dB as demonstrated in Fig. 2.11.

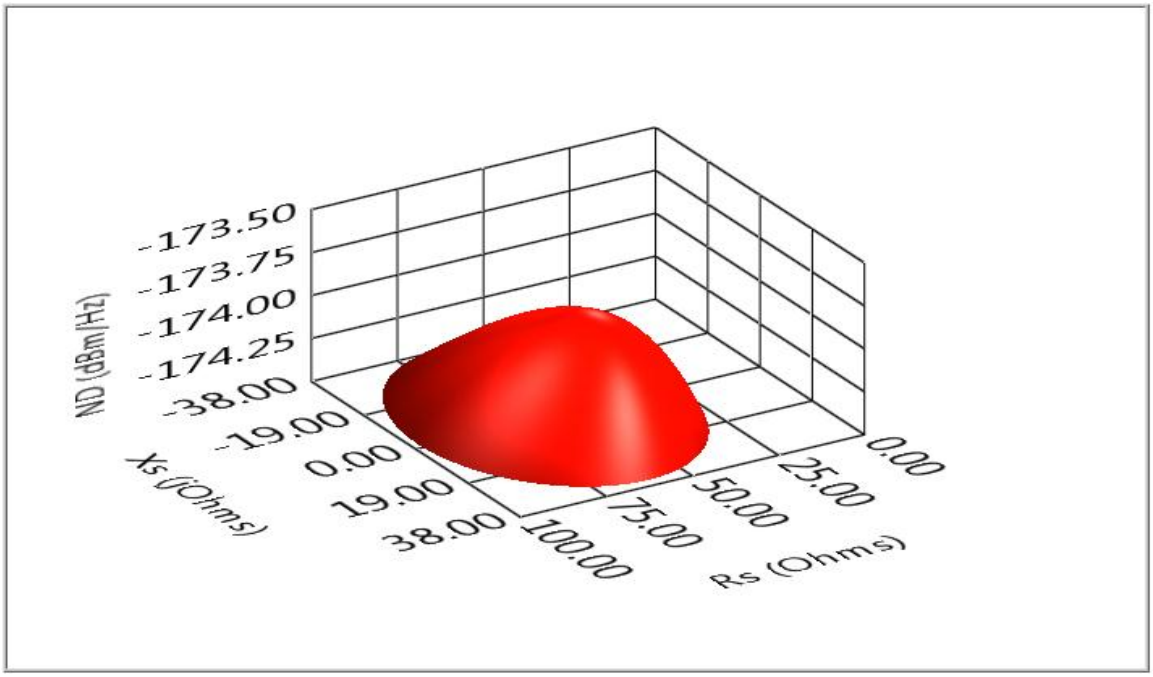

Fig. 2.9: Noise density at the ideal DUT input vs. source impedance

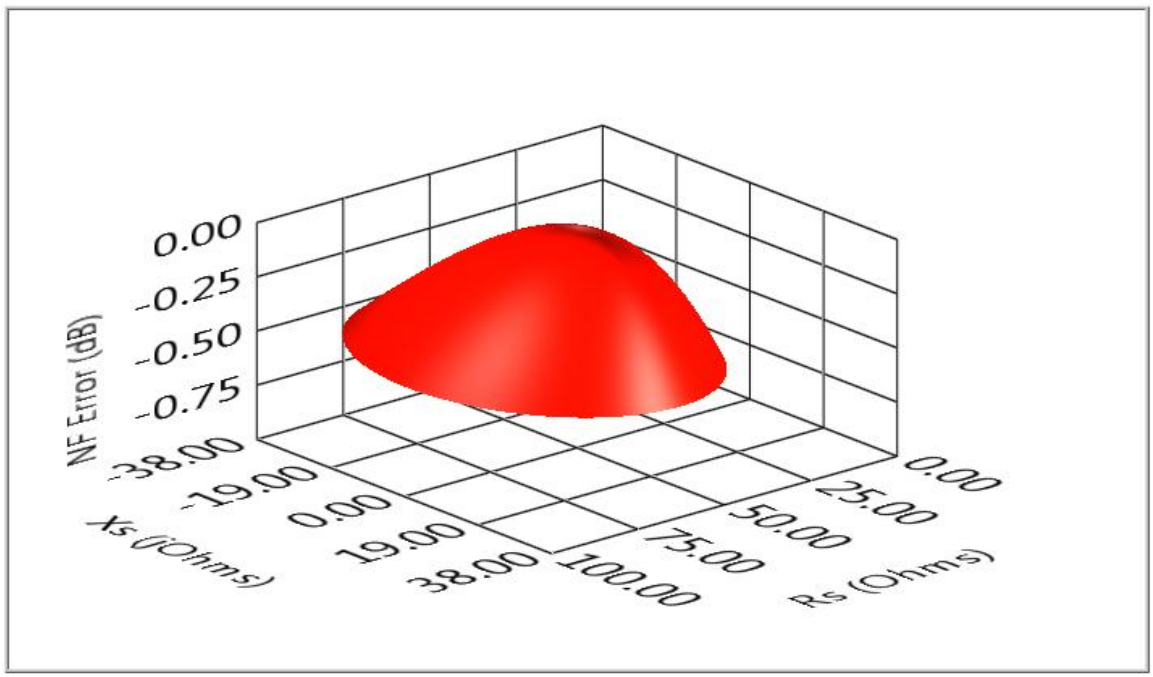

Fig. 2.10: NF error (or TFNF error) vs. source impedance

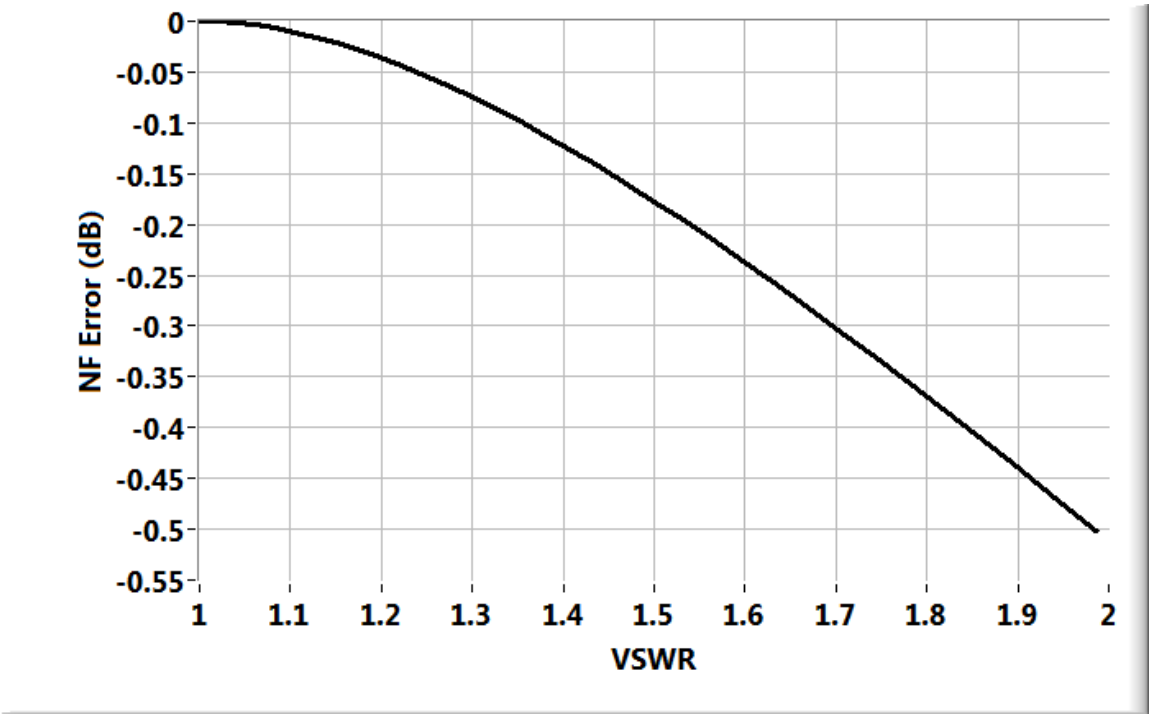

Fig. 2.11: NF error vs. VSWR

2.3.2.3 Input-Referred Third-Order Intercept Point

2.3.2.3.1 IIP3 or ITOI a Measure of Non-Linearity

Input-referred third-order intercept point, otherwise abbreviated as IIP3 or ITOI, is a measure of device non-linearity, particularly third-order non-linearity. Thus, as shall be discussed in this section, IIP3 relates to the third-order non-linear gain component α_3, shown in (2.6). In the next section, mathematical analysis is presented, which ties the IIP3 of a device to its fundamental, linear and non-linear, gain components. Additionally, the analysis serves to shed light and make sense of the IIP3 measurement procedure presented in Section 2.3.1.3.

2.3.2.3.2 Tying IIP3 to Gain Components

Performing a similar analysis to that done in Section 2.3.2.1.2, we start by considering the input being a two-tone signal, where the two tones are of equal magnitudes. Formulated accordingly, $X = A(\sin(w_1 t) + \sin(w_2 t))$, where w_1 and w_2, the angular frequencies of the two tones, are already presented for baseband analysis and take into account the frequency translation by the LO from RF to baseband. Substituting X into (2.6) yields the following:

$$\begin{aligned} Y = {} & \alpha_1 A(\sin(w_1 t) + \sin(w_2 t)) + \alpha_2 A^2(\sin(w_1 t) + \sin(w_2 t))^2 \\ & + \alpha_3 A^3(\sin(w_1 t) + \sin(w_2 t))^3 \end{aligned} \tag{2.17}$$

Expanding (2.17) yields (2.18).

$$\begin{aligned} Y = {} & \alpha_1 A[\sin(w_1 t) + \sin(w_2 t)] \\ & + \alpha_2 A^2[\sin^2(w_1 t) + \sin^2(w_2 t) + 2\sin(w_1 t)\sin(w_2 t)] \\ & + \alpha_3 A^3[\sin^3(w_1 t) + \sin^3(w_2 t) \\ & + 3\sin^2(w_1 t)\sin(w_2 t) + 3\sin^2(w_2 t)\sin(w_1 t)] \end{aligned} \tag{2.18}$$

Using (2.8) and (2.9), in addition to the transformation equations presented in (2.19) and (2.20), (2.18) can be rewritten into (2.21).

Below is the transformation equation for the $\sin(\,)\sin(\,)$ term.

$$2\sin(w_1 t)\sin(w_2 t) = \cos\big((w_1 - w_2)t\big) - \cos\big((w_1 + w_2)t\big) \tag{2.19}$$

The transformation shown in (2.20) applies to both the $\sin^2(\,)\sin(\,)$ terms of (2.18).

$$\begin{aligned} & \sin^2(w_1 t)\sin(w_2 t) \\ & = \frac{\sin\big((2w_1 - w_2)t\big) - \sin\big((2w_1 + w_2)t\big) + 2\sin(w_2 t)}{4} \end{aligned} \tag{2.20}$$

Finally, (2.21) expresses Y in terms of first-order sine and cosine elements, which represents tones at various frequencies.

$$
\begin{aligned}
&Y \\
&= \alpha_1 A(\sin(w_1 t) + \sin(w_2 t)) \\
&+ \alpha_2 A^2 \left(\frac{1 - \cos(2w_1 t)}{2} + \frac{1 - \cos(2w_2 t)}{2} + \cos\big((w_1 - w_2)t\big) \right. \\
&\left. - \cos\big((w_1 + w_2)t\big) \right) \\
&+ \alpha_3 A^3 \left(\frac{3\sin(w_1 t) - \sin(3w_1 t)}{4} + \frac{3\sin(w_2 t) - \sin(3w_2 t)}{4} \right. \\
&+ 3\frac{\sin\big((2w_1 - w_2)t\big) - \sin\big((2w_1 + w_2)t\big) + 2\sin(w_2 t)}{4} \\
&\left. + 3\frac{\sin\big((2w_2 - w_1)t\big) - \sin\big((2w_2 + w_1)t\big) + 2\sin(w_1 t)}{4} \right)
\end{aligned}
\tag{2.21}
$$

For the purpose of IIP3 computation, we are interested in two tones, the tone at w_1, which is representative of the tone at w_2 due to symmetry, and the tone at $(2w_1 - w_2)$, which is similarly representative of the tone at $(2w_2 - w_1)$. (2.22) shows the component of Y that is at w_1, while (2.23) shows the component that is at $(2w_1 - w_2)$.

$$
Y_{@W_1} = \left(\alpha_1 A + \frac{9\alpha_3 A^3}{4} \right) \sin(w_1 t) \tag{2.22}
$$

$$
Y_{@(2w_1 - w_2)} = \frac{3\alpha_3 A^3}{4} \sin\big((2w_1 - w_2)t\big) \tag{2.23}
$$

Following the procedure laid out in Section 2.3.1.3, the tone levels, both the main and the IMD, are to be computed in dBm. Expressing the IMD tone level in dBm is shown in (2.24), where $(3\alpha_3 A^3/4)$ is V_{Peak} of the IMD tone and where Z_0 is the load impedance that the DUT output is driving, which in a 50Ω system is nominally 50Ω. This would be the value of IMD_{Output} shown in (2.5).

$$
\left| Y_{@(2w_1 - w_2)} \right| (dBm) = 10 Log_{10} \left(\left| \left(\frac{3\alpha_3 A^3}{4} \right)^2 \frac{10^3}{2Z_0} \right| \right) \tag{2.24}
$$

Similarly, expressing the main tone level in dBm is shown in (2.25). This would be the value of TT_{Output} shown in (2.5).

$$\left|Y_{@w_1}\right|(dBm) = 10Log_{10}\left(\left|\left(\alpha_1 A + \frac{9\alpha_3 A^3}{4}\right)^2 \frac{10^3}{2Z_0}\right|\right) \tag{2.25}$$

Continuing with the procedure, the remaining term of (2.5) is G, whose expression for measured value is found in (2.12) and that for theoretical value is found in (2.13). Thus, the IIP3 measured value can be computed as shown in (2.26).

$$\begin{aligned} &IIP3(dBm) \\ &= \frac{30Log_{10}\left(\left|\left(\alpha_1 A + \frac{9\alpha_3 A^3}{4}\right)^2 \frac{10^3}{2Z_0}\right|\right) - 10Log_{10}\left(\left|\left(\frac{3\alpha_3 A^3}{4}\right)^2 \frac{10^3}{2Z_0}\right|\right)}{2} \\ &- 20Log_{10}\left(\left|\alpha_1 + \frac{3\alpha_3 A^2}{4}\right|\right) \end{aligned} \tag{2.26}$$

Simplifying the IIP3 expression in (2.26) results in the final measured IIP3 form of (2.27).

$$IIP3(dBm) = 10Log_{10}\left(\left|\frac{(4\alpha_1 + 9\alpha_3 A^2)^3 10^3}{6Z_0\alpha_3(4\alpha_1 + 3\alpha_3 A^2)^2}\right|\right) \tag{2.27}$$

2.3.2.3.3 Measured vs. Theoretical IIP3

Whereas (2.27) shows the expression for the IIP3 measured value, the IIP3 theoretical value, not including secondary effects, is presented in this section and compared to the measured value. For the theoretical IIP3 computation, the gain used for the purpose of referring the IP3 value to the DUT input is the theoretical linear gain, and the output main tone level value used is simply the input main tone level multiplied by the theoretical linear gain. Thus, the theoretical IIP3 value is computed as shown in (2.28), following the same structure as in (2.26).

$$IIP3(dBm) = \frac{30Log_{10}\left(\left|(\alpha_1 A)^2 \frac{10^3}{2Z_0}\right|\right) - 10Log_{10}\left(\left|\left(\frac{3\alpha_3 A^3}{4}\right)^2 \frac{10^3}{2Z_0}\right|\right)}{2} - 20Log_{10}(\alpha_1) \quad (2.28)$$

Simplifying the expression in (2.28) results in (2.29), which is the more common form of IIP3, especially if Z_0 is replaced with 50Ω, where it becomes simply $10Log_{10}\left(10\left|\frac{4\alpha_1}{3\alpha_3}\right|\right)$.

$$IIP3(dBm) = 10Log_{10}\left(\left|\frac{4\alpha_1 10^3}{6\alpha_3 Z_0}\right|\right) \quad (2.29)$$

Comparing the measured IIP3 value to the theoretical value results in the plots shown in Fig. 2.12. In a similar manner to how gain behaves, measured IIP3 tracks the theoretical IIP3 for values of the input two-tone signal level specified by the system. For the -40 dBm per tone case, the difference is less than 0.14 dB. For the -43 dBm per tone case, which corresponds to a -40 dBm overall two-tone signal level, the difference is around 0.07 dB. Finally, the difference drops below one thousandth of a dB for levels below -61 dBm. In the following section, the gain measurement is revisited; analysis is done with the two-tone input signal instead of the single-tone input used in Section 2.3.2.1.3.

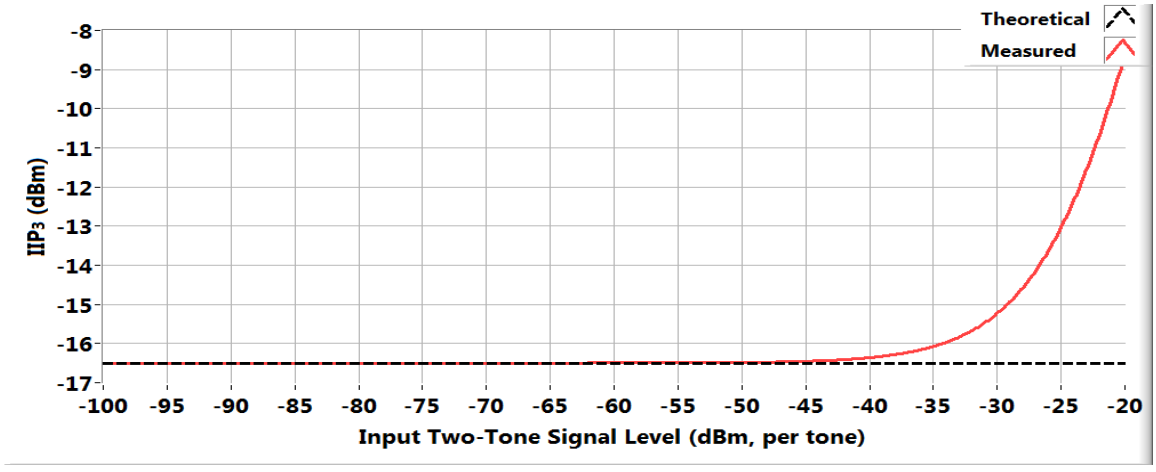

Fig. 2.12: Measured IIP3 value compared to the theoretical value vs. the input two-tone signal level

2.3.2.3.4 Revisiting the Forgiveness of Gain Measurement

Notice that the component of Y that is at w_1 shown in (2.22) is different from that shown in (2.10), although the input signal directly (linearly) corresponding to the output tone at w_1 did not change. It remained as $A\sin(w_1 t)$, exactly as presented in Section 2.3.2.1.2. This change, a 3-time multiplication of the non-linear component, means that Fig. 2.7 needs to be revisited for the case where a two-tone input signal is used and where one of the tones is used for measuring gain, in the presence of the second tone. Fig. 2.13 is the version of Fig. 2.7 that compares the measured gain to the theoretical linear gain versus the input tone level when a two-tone signal is at the input of the DUT. While Fig. 2.13 reflects an earlier separation between the theoretical and measured gain, the difference at an input of -40 dBm per tone is still only ~ 0.12 dB, which while being 3 times the 0.04 dB of difference reflected in Fig. 2.7 is still small. Moreover, working from the output stage limitation of handling strong signals, one can argue that for an apple-to-apple comparison, the condition of a -40 dBm single-tone input ought to be compared to that of a -43 dBm two-tone signal, to maintain the same power at the output. In this case, the difference seen between the measured and theoretical gain of the DUT is less than 0.06 dB. For levels up to around -55 dBm, the difference remains under one thousandth of a dB.

2.3.2.3.5 The IIP3 Measurement Procedure

The DUT's output stage typically gets compressed and even experiences "hard-clipping" well before the main tone level becomes dominated by its third order component presented in (2.22). That is why it is standard practice to consider the IIP3 as that expressed in (2.29), where the linear gain and linear-gain-amplified main tones are considered. The linearly-extrapolated main and IMD tone levels intersect, because while

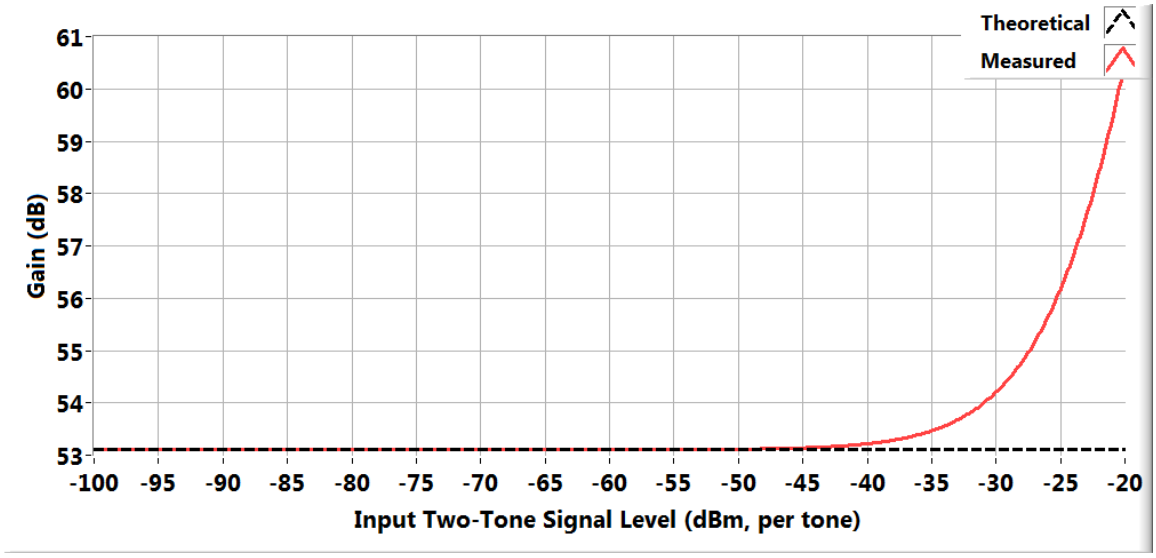

Fig. 2.13: Measured gain compared to theoretical linear gain vs. the two-tone signal tone's level

the IMD tone starts lower than the main tone, it grows at a faster rate versus the input signal level. In Fig. 2.14 one can see the IMD tone rate growing at a 3:1 rate compared to the input, while the main tone is growing at a 1:1 rate with the input. This also means that the IMD tone grows at a 3:1 rate compared to the output main tone in the dB scale. This applies to the practical range where the main tone's level $(\alpha_1 A + 9\alpha_3 A^3/4)$, shown in (2.22), is dominated by the $(\alpha_1 A)$ component. And given the IMD tone's level of $(3\alpha_3 A^3/4)$, it is clear why the main tone grows at 1:1 with the input signal level A and the IMD tone grows at cubic rate of A. However, since the levels are plotted in dBm, the logarithm function demonstrates the cubic rate as a 3:1 slope, while keeping the 1:1 rate unchanged.

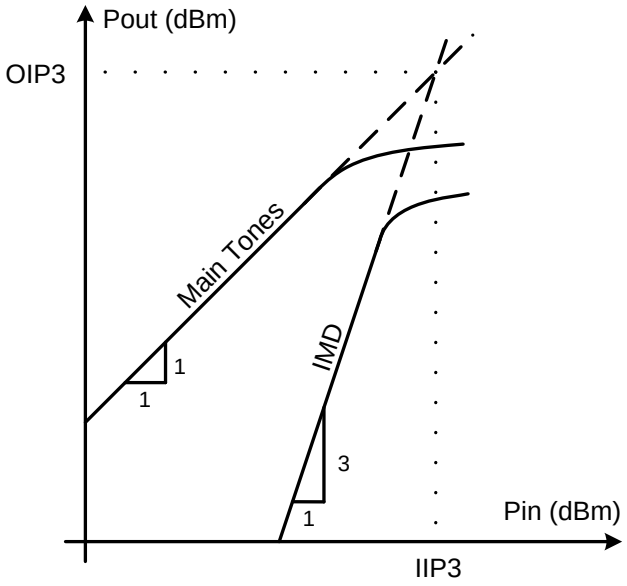

Fig. 2.14: IIP3/OIP3 resulting from 3:1 IMD3 and 1:1 Main/Wanted Tones Growth Rates

From the graph above, one can express the IMD tone level in dBm as follows:

$$Y_{IMD}(dBm) = 3X + C_{IMD} \tag{2.30}$$

where X is the input signal level in dBm and where C_{IMD} is a constant that can be determined by knowing the IMD level Y_{IMD} in dBm at any given input X in dBm. The main tone level is similarly expressed as follows:

$$Y_{Main}(dBm) = X + C_{Main} \tag{2.31}$$

where C_{Main} is also a constant that can be found at any given input X by knowing the main tone level Y_{Main}, as $(Y_{Main} - X)$. Thus, C_{Main} is essentially the DUT gain G in dB. IIP_3 is the input X itself when Y_{IMD} and Y_{Main} become at the same level, when the plots shown in Fig. 2.14 above intersect.

$$3X_{IIP3} + C_{IMD} = X_{IIP3} + C_{Main} \tag{2.32}$$

And, X_{IIP3} can be written as:

$$X_{IIP3} = \frac{C_{Main} - C_{IMD}}{2} \tag{2.33}$$

Substituting the value of C_{Main} and C_{IMD} from (2.30) and (2.31) at a given point P, results in (2.34).

$$X_{IIP3} = \frac{\left(Y_{Main_P} - X_P\right) - \left(Y_{IMD_P} - 3X_P\right)}{2} = \frac{Y_{Main_P} - Y_{IMD_P}}{2} + X_P \tag{2.34}$$

By adding and subtracting C_{Main} to the right side of (2.34), one can rewrite (2.34) into (2.35).

$$\begin{aligned} X_{IIP3} &= \frac{Y_{Main_P} - Y_{IMD_P}}{2} + (X_P + C_{Main}) - C_{Main} \\ &= \frac{3Y_{Main_P} - Y_{IMD_P}}{2} - C_{Main} \end{aligned} \tag{2.35}$$

Since C_{Main} is nothing but the DUT gain G in dB, (2.35) is essentially the procedural IIP3 calculation shown in (2.5), where Y_{Main_P} and Y_{IMD_P} are the main and IMD tone levels in dBm at a given input level. In (2.5) these are termed TT_{Output} and IMD_{Output}, respectively.

3 BUILDING BLOCKS OF THE TEST METHODOLOGY

3.1 Overview

As discussed below, the proposed methodology comprises digital-based RF signal generation and characterization, common baseband signal acquisition and baseband measurements, and signal processing. The methodology seeks to reduce the complexity in RF receiver generation for receiver testing. Consequently, with the digital-based signal generation implemented on the DUT load-board, the methodology enables less expensive digital testers with limited baseband capability to test RF receivers and extract RF parameters, which are otherwise impossible to measure on such ATEs. This chapter covers in detail the hardware as well as the measurement building blocks of the presented test methodology.

3.2 RF Signal Generation

3.2.1 TOPOLOGY

A simple digital circuit is proposed for the broadband MT generation scheme. At the core of it is a 2-input XOR gate, whose first input is sourced by a digital clock and whose second input is sourced by a delayed version of the same clock, as shown in Fig. 3.1. The delay can be implemented using 2 cascaded inverters if the multitone signal generator (MTSG) is designed on chip, or using controlled traces with calculated different lengths if the implementation is on a load board, as in the experimental case covered in this dissertation and explained in detail in Section 3.2.3.2. Alternatively, the delay can be implemented using a single inverter in front of one of the inputs of an AND gate, as described in [13]. The delay corresponds to the MTSG signal's designed pulse

width, and thus for very small delays, the MTSG signal approaches a periodic impulse. Practically, any time-domain impulse signal involves a non-zero pulse width and non-zero rise-time as well as other anomalies, which alter the transformation shown in Fig. 2.1. This results in a limited and non-uniform corresponding spectrum with a well-known $Sinc(x)$ shaping superimposed on the tonal spectrum, where $x = \pi f D$, with f being the frequency and D being the delay illustrated in Fig. 3.1. D also corresponds to the pulse width. However, in this application the pulse width is designed to be sufficiently small such that the first $Sinc(x)$ null occurs at sufficiently high frequency such that the MTSG output signal can be approximated by a periodic impulse, whose relatively-flat spectrum is composed of multiple tones in the band of operation. Furthermore, while the MTSG signal tones are theoretically harmonics of twice the input clock frequency (Fig. 3.1b, $T_2 = T_1/2$), in reality they are harmonics of the input clock frequency itself. This is because the rising and falling edges of the digital logic are not symmetrical. Therefore, the impulse generated at the output of the XOR gate is different for the rising input clock edge compared to the falling input clock edge. So, instead of having an impulse train of twice the input clock frequency, we have a pseudo-impulse signal whose frequency is that of the input clock, and whose period contains two distinct impulses, one corresponding to the rising edge of the input clock and one to the falling edge. On the other hand, the AND gate implementation discussed in [13] inherently results in a pulse train of frequency equal to the clock frequency, because the pulse is generated on only the rising edge of the original, un-delayed and un-inverted clock. Because the AND gate implementation requires only one inverter to implement the delay, as opposed to 2 inverters required for the XOR gate implementation, the AND gate implementation can achieve narrower pulses, corresponding to smaller delays, and thus can more closely approach the ideal impulse train if logic is used to implement the delay.

However, where controlled impedance trace length difference is used to implement the delay, the AND gate method cannot be used, as it requires at least one inverter to be used at the AND gate input. For the work of this dissertation, the XOR gate implementation was chosen, in conjunction with length difference of two traces with controlled impedance for implementing the delay.

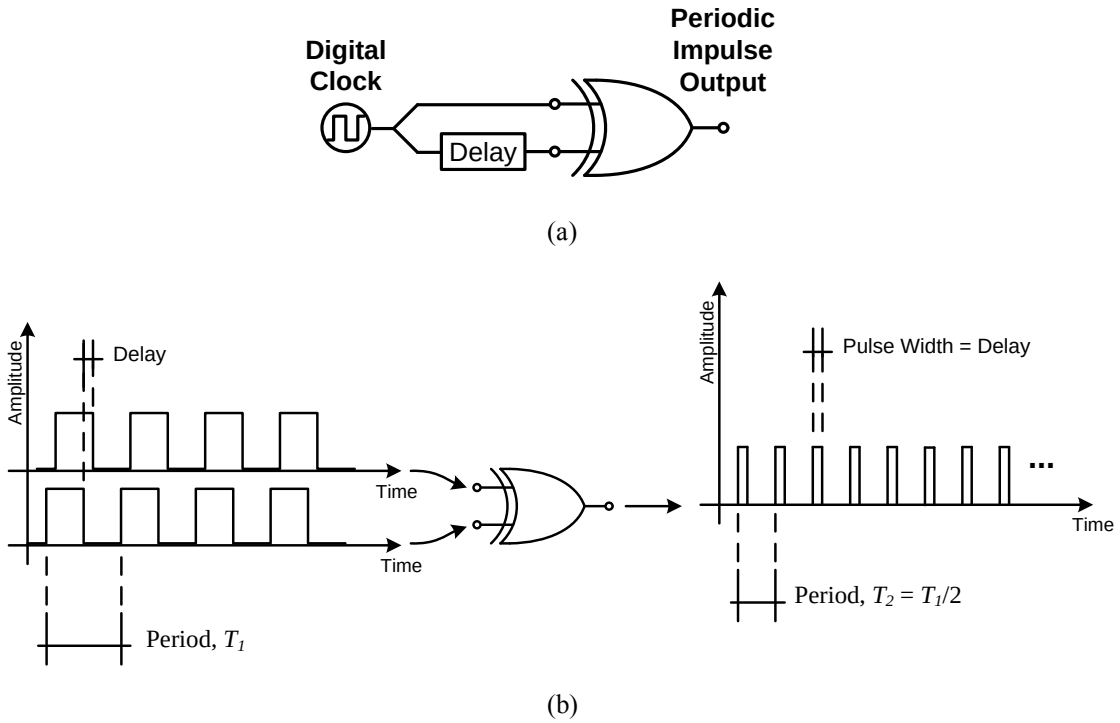

Fig. 3.1: Multitone Signal Generator (MTSG) (a) MTSG block diagram (b) MTSG operation demonstration

Another aspect of the RF signal generation block is the RF Digital-Step Attenuator (DSA) that allows for providing the test system with multiple RF input levels. RF DSAs are commonly available for board use and have been implemented on chips for over a decade. They are composed of cascaded "power-of-2" resistive attenuators that can be switched in and out resulting in nominal attenuation values that range between 0

dB and 63 dB, with available typical attenuation step or resolution of 1 dB, 0.5 dB, or 0.25 dB. For the experimental work covered in Section 3.2.3, two 5-bit off-the-shelf RF DSA parts were cascaded to achieve a 0 dB to 62 dB attenuation range with a 1 dB step size. For an on-chip implementation, the design of the RF DSA needs to be considered separately, [23] [24].

3.2.2 PRACTICAL CONSIDERATIONS AND SIMULATION RESULTS

The spectrum of a practical periodic impulse signal like the MTSG's output is limited in bandwidth and is non-uniform, as mentioned earlier. However, it can still be useful in the testing of RF receivers in the low-GHz range, where the spectrum can be flat to within 1 dB. The peak voltage of harmonic tones of a 1V peak pulse train with first order transient behavior, whose pulse width is W_{pulse}, frequency is f_0, and whose equal edge rise and fall time is t_r, can be expressed as follows:

$$\left|V_{peak}\right| = \left|\frac{2f_0 W_{pulse} Sinc\left(\pi f W_{pulse}\right)}{1 + j2\pi f t_r / a}\right| \tag{3.1}$$

where f is the harmonic tone frequency and a is a constant that relates the rise and fall time of a first order system to its bandwidth. For a 10% to 90% rise and 90% to 10% fall time definition α equals 2.1972245. The expression of $\left|V_{peak}\right|$ is derived based on an ideal pulse train of a pulse width W_{pulse} applied to a first order low-pass filter, whose bandwidth is determined by the desired rise/fall time t_r. Fig. 3.2 illustrates the harmonic tones' peak envelope and relates the envelope's characteristics to the signal parameters discussed above.

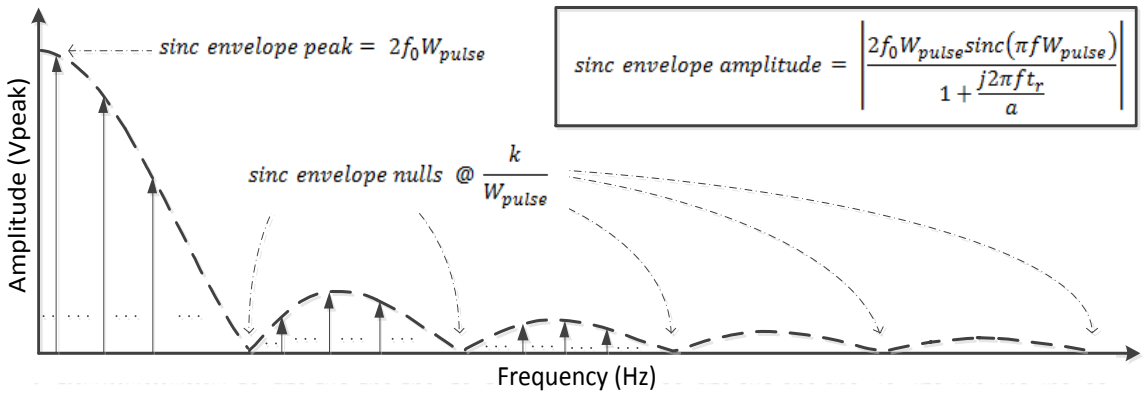

Fig. 3.2: MTSG Sinc envelope illustration

Using the expression for $|V_{peak}|$ in (3.1), a 3-D plot of the harmonic tone frequency corresponding to 1 dB flatness is presented versus the pulse width W_{pulse} and the rise and fall time, t_r. Fig. 3.3a shows a 3D view of the 1 dB flatness frequency response versus W_{pulse} and t_r, while Fig. 3.3b shows the planar projection, with the value of the 1 dB flatness frequency in GHz being color coded per the graph legend. The flatness of the MTSG response is dependent on both W_{pulse} and t_r.

Whereas the maximum level corresponding to the fundamental tone of the MTSG signal can be seen from the expression of $|V_{peak}|$ in (3.1) to depend on the pulse train frequency f_0, the pulse width W_{pulse}, and the rise/fall time t_r, its dependence on t_r is very weak for practical values of t_r and W_{pulse}. In fact, for values of t_r that are on the order of or smaller than 10 times W_{pulse}, the dependence of the maximum level on t_r is sufficiently negligible that it can be ignored without practical implications. Even for t_r values ranging up to 100 times the desired W_{pulse}, the maximum MTSG level varies by only 0.5 dB versus t_r. This is caused by the slow rise/fall time starting to significantly reduce the energy contained in the pulse. However, such large rise/fall times are not useful for RF applications as they severely affect the flatness of the MTSG spectrum and

limit its bandwidth much before the effect on the maximum level becomes significant. Fig. 3.4 presents the MTSG maximum level corresponding to a 10 MHz pulse train, expressed in dBm into a 50 Ω load. Fig. 3.4a shows the 3-D view, which demonstrates the max level's near-perfect independence of t_r, for the range of W_{pulse} and t_r shown. Fig. 3.4b shows the projection of the 3-D plot and presents the max level versus W_{pulse}.

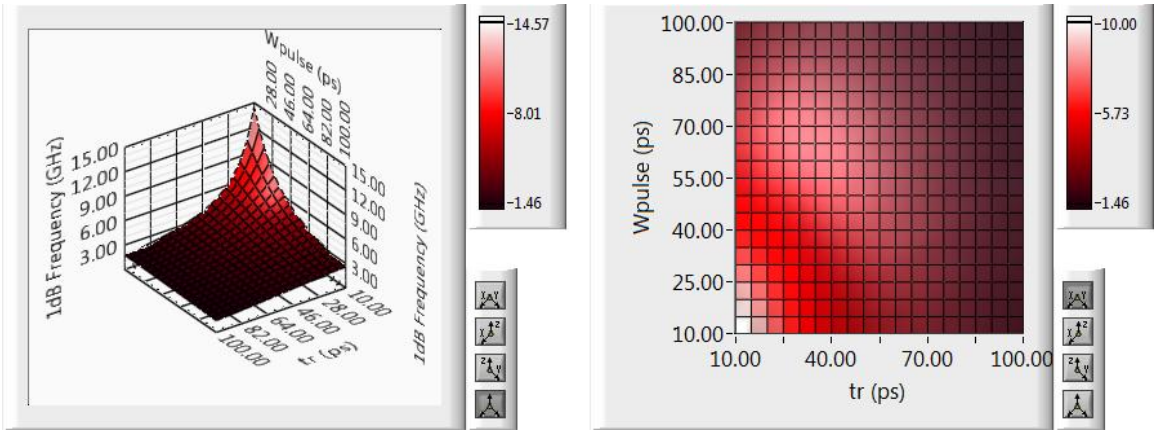

(a) (b)

Fig. 3.3: MTSG 1 dB flatness frequency versus W_{pulse} and t_r (a) 3D View (b) Projection

For load board applications, the variation encountered is primarily in rise/fall time, which has a negligible effect on the maximum level. The reason is that the delay is best implemented on board via a calculated difference in controlled trace length feeding the clock to the two inputs of the XOR gate, as mentioned earlier. The tolerance in trace length (even considering the effective electrical length that takes into account the dielectric constant variation across the board) is typically negligible and much smaller than that corresponding to the cascaded inverters implementation's variation. This results in a load board MTSG source that has low part-to-part performance variation in terms of the fundamental tone level and also has a sufficiently flat response up to at least 1 GHz.

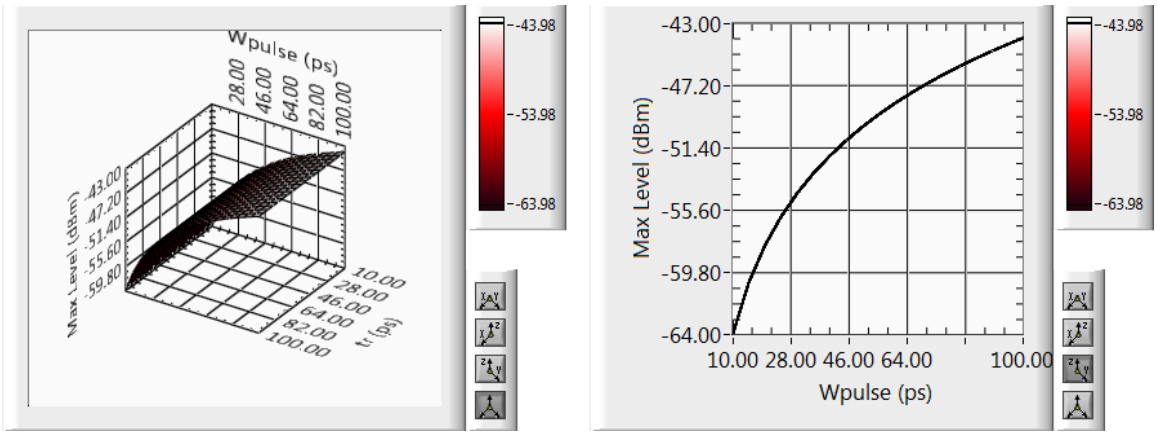

(a) (b)

Fig. 3.4: MTSG max harmonic tone level in dBm (a) 3D view (b) Projection

Using moderately demanding delay and rise-time means (μ) and conservative standard-deviations (σ) chosen based on [25] and [26] ($\mu_{rise\text{-}time}$ = 100 psec, $\sigma_{rise\text{-}time}$ = 8 psec, μ_{delay} = 100 psec, and σ_{delay} = 8 psec) a Monte-Carlo simulation was run to show the histogram of the 1 dB flatness frequency and the max level resulting from the interaction of varying W_{pulse} and t_r simultaneously. The simulation is a statistical perturbation of the lowest 1 dB flatness point presented in Fig. 3.3, corresponding to a 100 psec rise/fall time and a 100 psec pulse width. Fig. 3.5 shows that the 1.46 GHz mean 1 dB flatness varies from around 1.2 GHz to 1.7 GHz given the perturbations in rise/fall time and pulse width. The max level varies by less than ±2 dB from the expected mean. For load board implementation, the MTSG can simply be characterized once per board and the results can serve as calibration inputs for the testing of many DUTs, and thus the limited variation of the response flatness and the max level is not critical or necessary. However, for a possible BIST implementation, since calibration of individual on-chip MTSGs is not feasible or practical, the knowledge of the MTSG level and response is based on pre-production DUT characterization, which generates a mean response for on-chip MTSGs

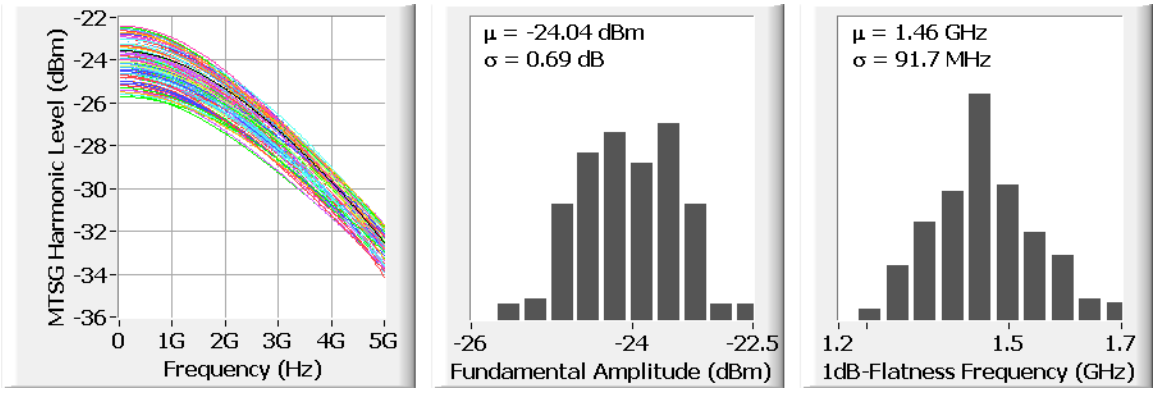

(a) (b) (c)

Fig. 3.5: MTSG Monte Carlo simulation on combined effect of rise-time (a) MTSG harmonic level (b) Fund. ampl. histogram (c) 1 dB-freq. histogram

that can be used as a reference response, and thus the limited variation in max level and response flatness becomes critical.

Note that while Fig. 3.5a shows continuous profiles for the MTSG harmonic levels, it is considered understood that the tones at which the DUT can be tested exist at only harmonic frequencies of f_{clk}. Consequently, if the DUT is to be tested at specific frequencies, then f_{clk} is to be chosen such that its harmonics cover these specific frequencies. In many cases, analog performance of wideband DUTs does not have to be evaluated at very specific frequencies, and thus the use of existing clock works well to cover the range of interest with acceptable frequency resolution.

3.2.3 Hardware Implementation and Experimental Results

3.2.3.1 Hardware Implementation Overview

The RF signal generation topology described above was implemented in hardware and its performance was characterized. The hardware implementation was done on a test board using off-the-shelf parts. A Texas Instruments (TI) 2-input XOR gate

SN74LVC1G86 (datasheet, [27]) was used for the core signal generation and a MACOM MAAT-SS-0002 (datasheet, [28]) 5-bit digital step RF attenuator was used for the level control. The choice of the digital attenuator for the experimental section, as MAAT-SS-0002, was driven by the requirement of being able to solder the part in a simple lab environment, in addition to its specifications being sufficient for the application at hand. If a professional-grade lab and soldering capability is readily available or higher bandwidth or higher step-resolution is required, then using other off-the-shelf digital attenuators like PE43703 from Peregrine Semiconductor (datasheet, [29]) can be considered. While rise-time is inherently set by the used XOR gate, and hence was mostly uncontrollable, the delay corresponding to the desired pulse-width was designed by calculating the trace length difference as covered in Section 3.2.3.2, next.

3.2.3.2 Designing and Implementing the Delay as a Trace Length Difference

On a controlled-impedance trace, the signal propagates as a wave at a certain speed, v_p, also known as velocity of wave propagation. In free-space the signal (wave) speed is given by the speed of light, that is $1/\sqrt{\varepsilon_0\mu_0} = 299{,}792{,}458\ \mathrm{m/sec}$, where ε_0 and μ_0 are the permittivity and permeability of free-space (vacuum), respectively. In a given medium, the wave propagation velocity $v_p = 1/\sqrt{\varepsilon\mu}$, where ε and μ are the effective permittivity and permeability of the propagation medium, respectively. Knowing the signal speed, and knowing how much time (delay) is needed, the length that the signal should undergo can be calculated by:

$$L_{trace} = v_p \times t_{delay} \tag{3.2}$$

Where L_{trace} is the trace length that the signal should traverse, v_p is the signal speed, and t_{delay} is the desired time delay. Thus, to be able to design a trace length

corresponding to a desired delay, one needs to know what the wave propagation velocity is in the specific propagation medium.

On the circuit boards employed for this work, the effective magnetic permeability can be assumed to be the same as that of free space. The effective dielectric permittivity however can be significantly different from that of free space. For the MTSG hardware implementation, a standard FR4 material with relative dielectric constant (ε_r) of 4.8 was used.

Knowing the relative dielectric constant of the board material along with the details of the controlled-impedance trace geometry one can calculate the effective dielectric constant. For a Coplanar-with-Ground transmission line structure, which is the structure used in the work of this dissertation, the effective dielectric constant ε_e can be calculated as follows, ignoring the effect of trace thickness, which is typically negligible, especially in the low-GHz range [30]:

$$\varepsilon_e = \frac{1 + \varepsilon_r \frac{K\left(\sqrt{k'}\right)}{K(k)} \frac{K(kl)}{K\left(\sqrt{kl'}\right)}}{1 + \frac{K(k')}{K(k)} \frac{K(kl)}{K(kl')}} \tag{3.3}$$

where,

$$k = \frac{W}{W + 2G} \tag{3.4}$$

and

$$k' = \sqrt{1 - k^2} \tag{3.5}$$

and

$$kl = \frac{\tanh\left(\frac{\pi W}{4H}\right)}{\tanh\left(\frac{\pi(W + 2G)}{4H}\right)} \tag{3.6}$$

and

$$kl' = \sqrt{1 - kl^2} \tag{3.7}$$

and the function $K(\,)$ is the Elliptical Integral of the first kind, and finally where H, W, and G are the height of the board dielectric material, the trace width, and the air-gap between the trace and the surface ground, respectively, as shown in Fig. 3.6.

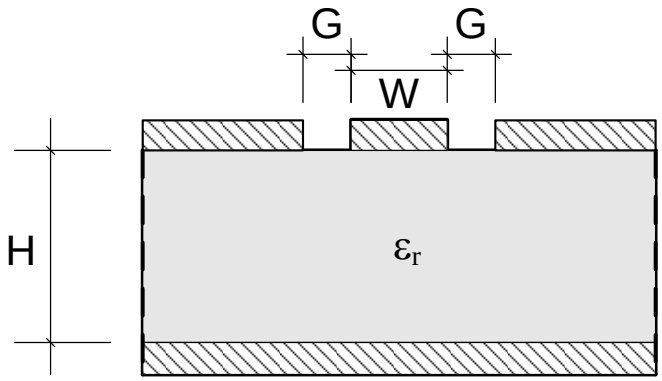

Fig. 3.6: Coplanar-with-Ground Transmission Line Cross-Section

For the MTSG hardware implementation, H was set by the board to 62 mils or 1.5748 mm, G was chosen to be 10 mils or 0.254 mm, and W was designed to be 52 mils or 1.3208 mm corresponding to a 50 Ω characteristic impedance (50.36 Ω actual designed) according to (3.8).

$$Z_0 = \frac{60\pi}{\sqrt{\varepsilon_e}\left(\frac{K(k)}{K(k')} + \frac{K(kl)}{K(kl')}\right)} \tag{3.8}$$

For the values above, the resulting effective dielectric constant on the board was found to be $\varepsilon_e = 0.626\varepsilon_r = 3.005$. Thus, the signal propagation velocity on the board can be calculated as $299{,}792{,}458/\sqrt{3.005} = 172{,}941{,}198.7\ m/sec$. Designing for ~75 psec delay (72.34 psec actual designed) resulted in a physical trace length (difference) of 12.51 mm or 492.5 mils, according to (3.2), and as shown in Fig. 3.7. The "cascaded

inverter" delay implementation block shown in Fig. 3.7 was ultimately not used for the work of this dissertation.

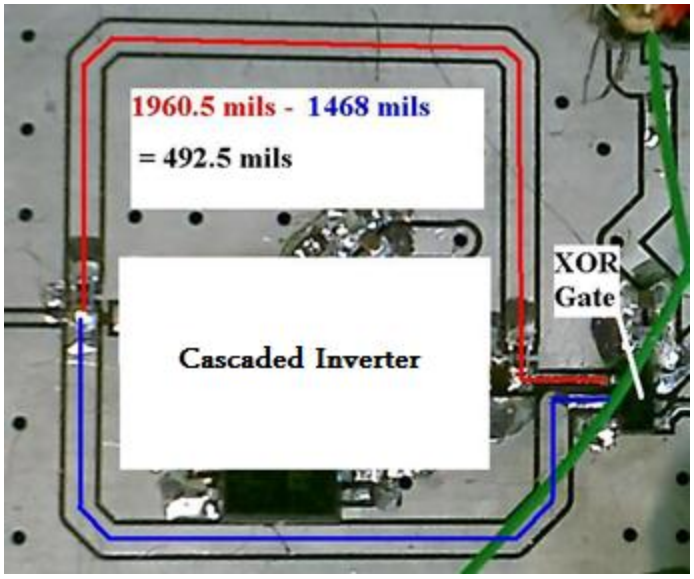

Fig. 3.7: MTSG Hardware Implementation with Trace-Length-Difference as Delay

3.2.3.3 Experimental Results

Feeding the MTSG hardware with a 10 MHz clock and characterizing the harmonics' amplitudes and phases across both the various DSA attenuation levels and frequency, we arrived at the graphs shown in Fig. 3.8. Fig. 3.9 shows the differences in amplitude levels experienced between a couple MTSG circuits upon characterization.

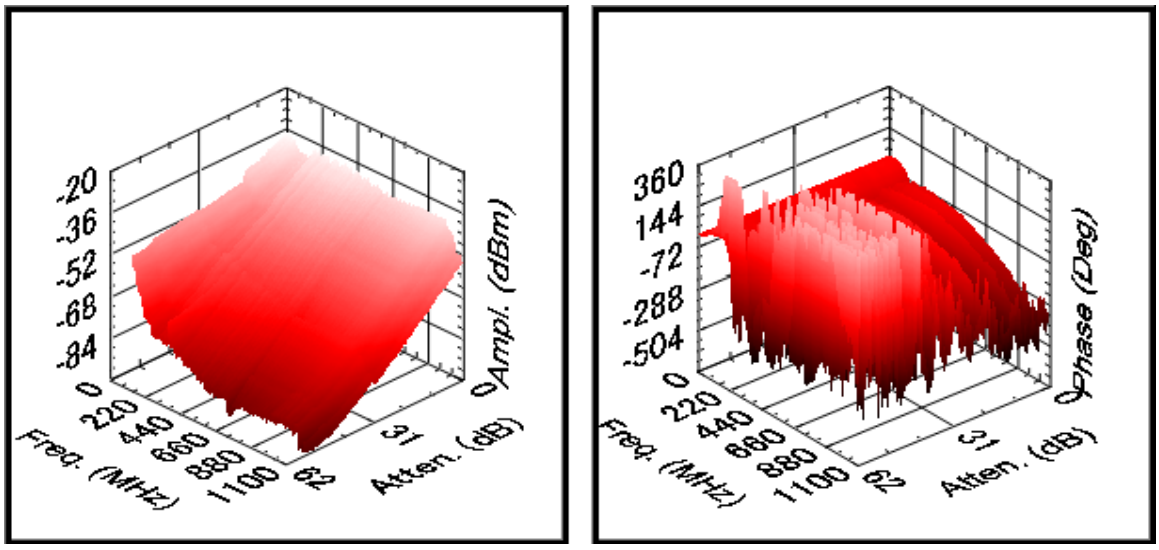

(a) (b)

Fig. 3.8: MTSG Tone Amplitude and Phase Characterization (a) Amplitude (b) Phase

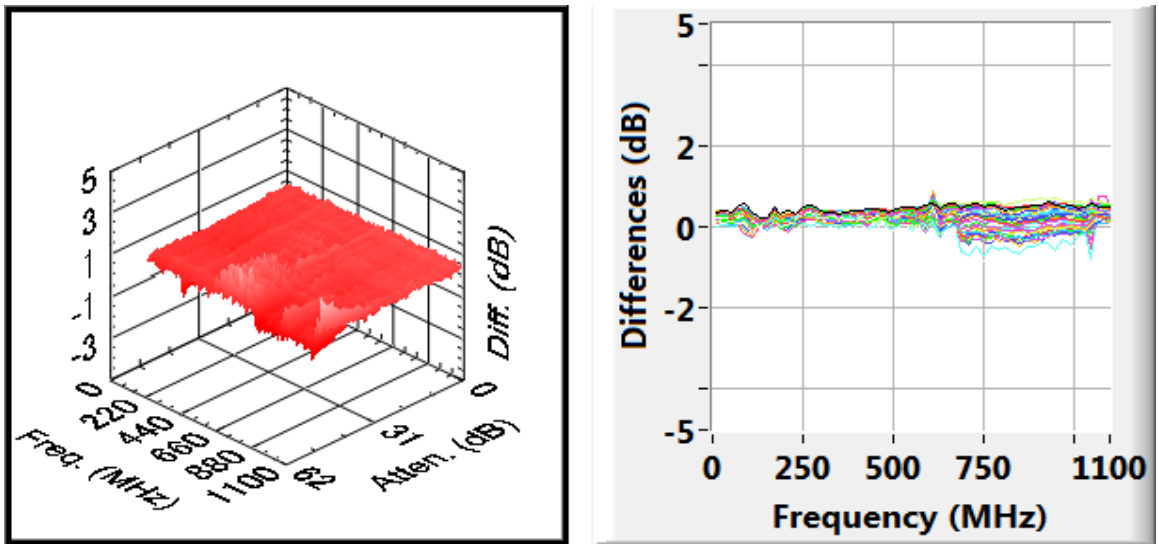

(a) (b)

Fig. 3.9: MTSG Part-to-Part Amplitude Differences (b) 3-D (b) Stacked 2-D

3.3 Basic Baseband Measurements

3.3.1 OVERVIEW

After the baseband signal is acquired, whether through an on-chip Analog-to-Digital Converter (ADC) or through an off-chip digitizer or signal acquisition instrument, two basic measurements are needed for the proposed test methodology: single-tone level extraction and noise density evaluation. These measurements are done at static MTSG settings (i.e. at a given MTSG attenuation setting). Both measurements require some basic signal processing including the Discrete Fourier Transform (DFT) or the Fast Fourier Transform (FFT is an efficient algorithm for performing DFT). This signal processing does not have to be done on-chip, even if the digitization is on-chip. The digitized signal time-domain samples can be transferred off-chip to the test platform, which can then handle the processing required. The test software on most test platforms includes libraries whose functions facilitate making these measurements. However, for the completeness of the presented methodology, we cover these measurements in detail over the next two sections, presenting all the needed analysis and assuming no availability of ready-made functions. The procedure of each measurement shall be general, although for the purpose of the experimental portion of this work it is applied specifically to a baseband signal, as explained earlier.

3.3.2 SINGLE-TONE LEVEL EXTRACTION

3.3.2.1 Operation Flow

Fig. 3.10 shows the flow chosen in the experimental setup discussed in this study. As shown in Fig. 3.10, amplitude scaling is first performed on the time-domain signal, followed by applying a Hann window. Then the DFT of the resulting time-domain signal is computed. Finally, processing of the DFT bins is performed to find the needed single-

tone parameters: the exact tone's frequency, amplitude, and phase. Note that from here onwards, we shall use the general term DFT, with FFT being understood as a common implementation method.

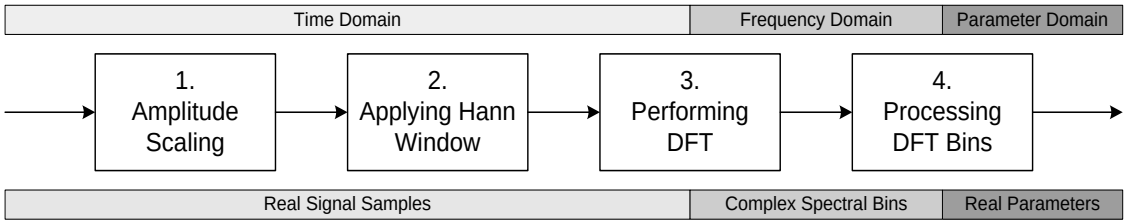

Fig. 3.10: Single-tone level extraction flow

3.3.2.2 Amplitude Scaling

The amplitude scaling step aims at preparing the time-domain signal samples for the DFT step, using the "Energy Theorem" to properly scale the time-domain samples, so that the resulting DFT spectrum correctly corresponds to the time domain signal level. The basis for this scaling step starts with the fundamental definition of the DFT and Inverse-DFT (IDFT), presented below, where $\{A_m\} = \{A_0, A_1, A_2, \dots A_{N-1}\}$ is the DFT block of the N time-domain samples $\{a_n\} = \{a_0, a_1, a_2, \dots a_{N-1}\}$

$$\begin{cases} DFT: \quad A_m = \sum_{n=0}^{N-1} a_n e^{-\frac{j2\pi mn}{N}} \\ IDFT: \quad a_n = \frac{1}{N} \sum_{m=0}^{N-1} A_m e^{\frac{j2\pi mn}{N}} \end{cases} \tag{3.9}$$

Derived from the definitions in (3.9), the Energy Theorem, also known as the Rayleigh Energy Theorem, is a special form of Parseval's Theorem which states that:

$$\sum_{n=0}^{N-1}|a_n|^2 = \frac{1}{N}\sum_{m=0}^{N-1}|A_m|^2 \tag{3.10}$$

Simple operations on (3.10) yield a more useful form, where the root-mean-square (RMS) value of the time-domain samples a_n is expressed as follows

$$a_{RMS} = \sqrt{\frac{1}{N}\sum_{n=0}^{N-1}|a_n|^2} = \sqrt{\frac{1}{N^2}\sum_{m=0}^{N-1}|A_m|^2} = \frac{1}{N}\sqrt{\sum_{m=0}^{N-1}|A_m|^2} \tag{3.11}$$

For a single-tone, the DFT spectrum bins, A_m, contain only two non-zero equal elements corresponding to the single-tone and its image above and with-respect-to the Nyquist $(F_s/2)$ frequency. Consequently, the single-tone level that will show up in the DFT spectrum (referring to one of the two equal tones, the single-tone within the Nyquist rate) can be found as follows

$$a_{RMS} = \frac{1}{N}\sqrt{2|A_m|^2} \rightarrow |A_m| = \frac{Na_{RMS}}{\sqrt{2}} \tag{3.12}$$

So, for 1000 samples of a $1V_{RMS}$ sine wave, the level of the tone that shows up in the DFT spectrum is ~ 707.1, and in order to obtain a value of 1 (corresponding to the $1V_{RMS}$) we need to divide the spectrum values (or pre-divide the time-domain samples) by 707.1. In general, the acquired time-domain samples in this first scaling operation step are multiplied by $\sqrt{2}/N$ before proceeding to the next steps and ultimately to the DFT operation.

3.3.2.3 Applying Hann Windowing

Applying a window to a time-domain signal, also known as "windowing", is done by multiplying the time-domain sample block by an array of values of the same size, called a window. Windows of all kinds have non-zero values in the middle, with

continuous tapering towards zero edges. Windowing is meant to remove discontinuities between the consecutive acquired frames or sample blocks. Discontinuities in the acquired time domain signal frames result in high-frequency spectral content, which otherwise does not exist in the actual signal. To understand the effect of windowing, first observe Fig. 3.11, which demonstrates the non-continuous, non-synchronous acquisition of a sine waveform. The black signal is the actual sine signal whereas the thick red signal demonstrates the acquired frames.

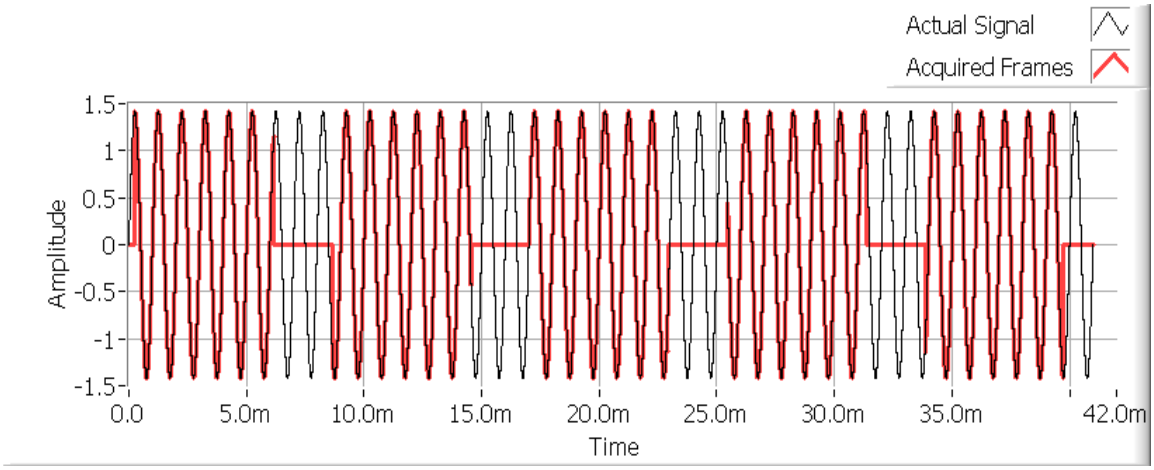

Fig. 3.11: Non-continuous non-synchronous acquisition of a sine wave

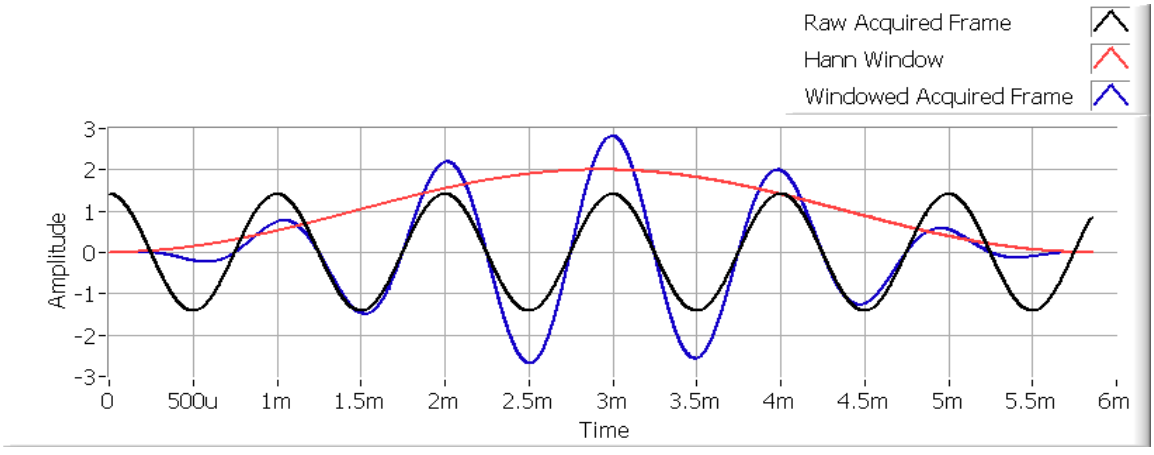

Fig. 3.12: Windowing of a single acquired frame

Note how the digitized (acquired) signal is not phase-continuous across frames, which is expected in standard non-synchronous digitization. Fig. 3.12 shows the windowing operation applied to one of the acquired frames, where the black signal is the raw acquired frame, the red plot is the Hann window itself, and the blue plot is the windowed acquired frame. Note how the windowed plot is zero-valued on the frame edges, so that consecutive frames become continuous. The value of the used Hann window in the center is designed such that the integration over the window span yields unity. Since the standard Hann window is mathematically defined to have a peak of unity (unlike the area-normalized Hann window shown in (3.13), the standard Hann window has a 0.5 multiplier for the entire expression), the integration across the window span (i.e. from n = 0 to N-1) yields $(N-1)/2$, half the area corresponding to a standard flat window. Hence, the properly scaled Hann window that achieves unity integration value is the area-normalized Hann window, which is shown in (3.13). As such, the window does not change the overall energy content of the signal.

$$W_{Hann}(n) = \left(1 - \cos\left(\frac{2\pi n}{N-1}\right)\right) \tag{3.13}$$

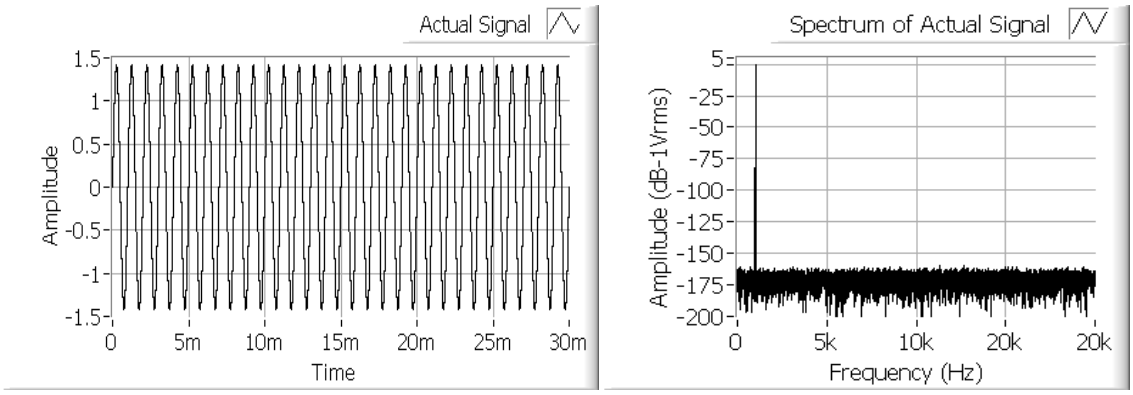

Fig. 3.13: The actual sine wave signal and its spectrum

Fig. 3.13 shows the actual sine wave signal along with its corresponding spectrum. Fig. 3.14 shows the concatenated raw (non-windowed) acquired frame signal along with its "rich" spectrum (i.e having false high-frequency content). Finally, Fig. 3.15 demonstrates how windowing addresses the problem seen in Fig. 3.14 to a great extent.

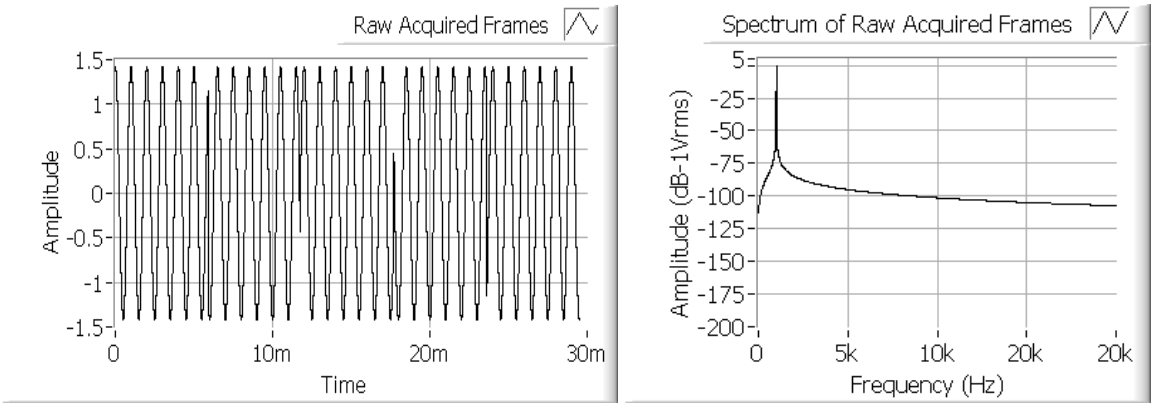

Fig. 3.14: The concatenated raw (non-windowed) acquired frame signal and its spectrum

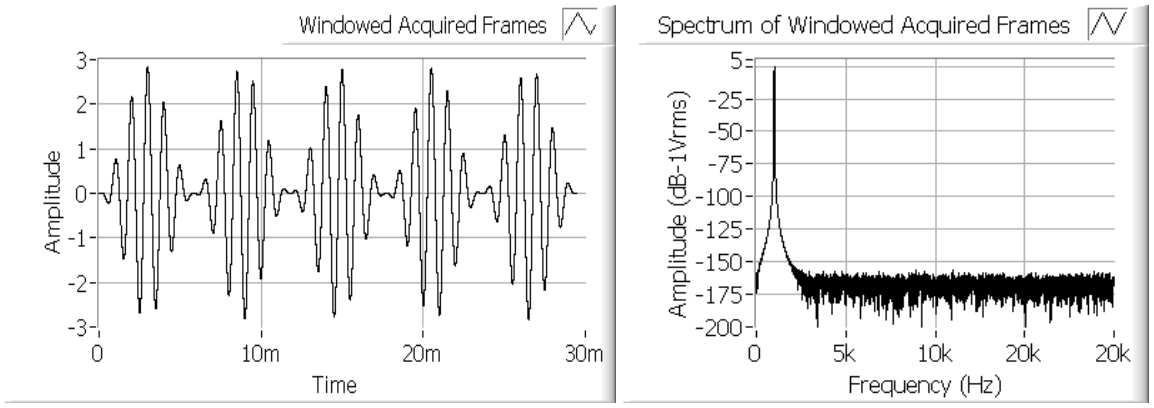

Fig. 3.15: The concatenated windowed acquired frame signal and its spectrum

3.3.2.4 Performing DFT and Processing the DFT Bins

3.3.2.4.1 Generating a proper spectrum

After the time domain samples, referred to in Section 3.3.2.2 as $\{a_n\}$, get scaled by $\sqrt{2}/N$ as described right after (3.12), and after they get windowed properly by multiplying the time domain samples by the Hann windows presented in (3.13), as described in Section 3.3.2.3, the spectral DFT bins, $\{A_m\}$, are computed in accordance to (3.9). Before proceeding to the actual single tone extraction, two things are done to the spectrum to make it a proper spectrum of a real signal. First, the imaginary spectrum (above the Nyquist rate, $F_s/2$) is ignored or discarded. Second, the DC bin value is corrected.

Regarding the removal of the spectrum elements corresponding to frequencies above $F_s/2$, it should be noted that for an odd number of samples N, the spectrum does not contain any bin that corresponds to exactly $F_s/2$. For the case when N is odd, the number of spectral bins to consider or keep are the first $(N+1)/2$ samples. These samples would not include any bins corresponding to above $F_s/2$. For instance, if $N = 31$, then the number of considered bins would be 16, and starting from the first bin, corresponding to DC or zero Hz, the 16th bin would correspond to $\frac{15}{31}F_s$. However, this 16th bin covers or represents the spectrum of bandwidth $F_s/31$ centered about it, so it does account for the spectrum up to $\frac{15}{31}F_s + \frac{\frac{1}{2}F_s}{31} = \frac{15.5}{31}F_s = \frac{Fs}{2}$, which is exactly the Nyquist rate. For the case where N is even, the spectral bins do include a bin that corresponds to exactly $F_s/2$. Whether or not to include such a bin is a dilemma, because the bin centered at $F_s/2$ covers spectrum above the Nyquist rate in addition to spectrum of equal bandwidth below the Nyquist rate. The common standard, which is also used in the work of this dissertation is that for even N, the number of considered bins is $N/2$,

thus stopping short of including the Nyquist, $F_S/2$, bin. For example, for $N = 32$, the number of considered bins is 16, which makes the last bin centered at $\frac{15}{32}F_S$. Even with this last bin covering a bin bandwidth of $\frac{F_S}{32}$, the highest covered frequency would be $\frac{15}{32}F_S + \frac{\frac{1}{2}F_S}{32} = \frac{15.5}{32}F_S < \frac{F_S}{2}$. Needless to say, having an odd number of samples yields a better and easier to interpret spectrum. As for the DC bin value correction, the DC bin represents only half the size of a standard bin, because it stops at zero on the lower end and is itself centered at zero. Consequently, the corrected value of the DC bin should halve the bin power corresponding to halving the bin bandwidth, and thus the new DC bin value is the original "amplitude" value divided by $\sqrt{2}$.

3.3.2.4.2 Single-Tone Extraction

The next step is to process the available DFT bins to find the single tone's exact amplitude, phase, and frequency. Extracting the single tone's information accurately is not as trivial as it may appear. Firstly, the spectrum may contain more than one tone, and in challenging cases, an abundance of tones, whose levels exceed that of the tone whose information is desired. Secondly, because of the coarse nature of the spectrum bins, where each bin corresponds to a specific discrete frequency, the desired tone's frequency can be such that there is no single bin that exactly corresponds to it (i.e. the desired tone frequency is in between bins). Such misalignment between the desired tone's actual frequency and the closest bin frequency, not only results in a frequency error should the bin frequency be used as the tone frequency, but also results in an amplitude and a phase error if the bin's amplitude and phase are used to represent the tone's amplitude and phase. There are a few ways to address the issue of discrete bins representing the continuous spectrum, including a single tone that may lie anywhere in the spectrum. Taking the weighted average for both frequency and amplitude is one method. Another

common method is interpolation. Such interpolation methodologies can usually be found ready-to-use in software analytical toolkits that contain signal processing. The specific interpolation methodology covered in this dissertation is a popular and accurate sinc-based interpolation, where $\mathrm{sinc}(x) = \sin(x)/x$, which is implemented in the *Extract Single Tone Information VI* within LabVIEW™, [31].

The sinc-based interpolation bases the single tone extraction on the highest spectral bin in the neighborhood of the desired tone along with its two neighboring bins, the adjacent lower frequency bin to the left and the adjacent higher frequency bin to the right. Fig. 3.16 demonstrates the bins forming the single tone desired for extraction. Note that the single tone is not treated as a single bin, as once assumed in Section 3.3.2.2 to formulate (3.12). This is due to the windowing effect on the spectrum, which causes the single tone to be spread across multiple bins. As designated in Fig. 3.16, the highest spectral bin is A_{MAX}, while the neighboring bins are A_L and A_R, to the left and right, respectively. Before presenting the calculation needed for extracting the single tone parameters, we make the following definitions. $\{A_m\}$ represents the spectral bins ranging from A_0 to A_{N-1}; the indices (0 through N-1) correspond to the frequency, ranging from 0 (or DC) to $F_s[(N-1)/N]$. Thus, a bin index i corresponds to a specific frequency, $F_s\, i/N$. For real signals, the bin corresponding to frequencies above $F_s/2$ are ignored, as discussed earlier in Section 3.3.2.4.1. A frequency resolution term is formally defined herein as $F_{Res} = F_s/N$, which indicates the bandwidth represented in each spectral bin. This is the bandwidth that a bin covers as also previously alluded to in 3.3.2.4.1. A search window, W_{search}, within which the single tone is expected, is also defined herein. The search window is useful where the spectrum is expected to contain tones other than the desired one. The methodology presented below excludes some corrections that are

typically implemented in signal processing toolkits, such as [31], to account for aliasing near DC and $F_s/2$, which are not needed in the work of this dissertation. Also, note that the single-tone detected phase is necessarily an absolute phase, the phase at which the time domain sine wave starts, as captured. For instance, if the sine wave starts at exactly the zero-crossing prior to its positive cycle, then its phase is zero. If it starts at exactly its positive peak then its phase is 90°. If it starts at exactly its negative peak then its phase is 270° or -90°. Similar conditions can be deduced for other phases.

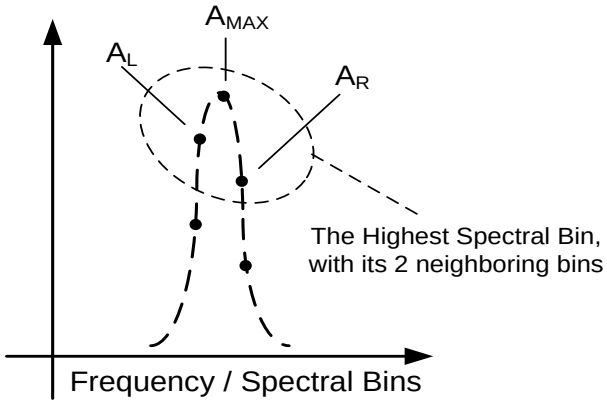

Fig. 3.16: The single-tone represented by multiple spectral bins

Below is the algorithm used for accurately extracting the single-tone parameters:

- If $|A_L| = |A_R|$
  - A_{MAX} represents the desired single-tone precisely
  - The desired single-tone frequency = $F_s\ i_{MAX}/N$
  - The desired single-tone peak amplitude = $|A_{MAX}|\sqrt{2}$
  - The desired single-tone phase = $< A_{MAX} + 90°$

  Where i_{MAX} is the index or bin number of A_{MAX}, $|A_{MAX}|$ is the magnitude of A_{MAX}, and $< A_{MAX}$ is the phase of A_{MAX} in degrees
- If $|A_L| > |A_R|$
  - The actual single-tone lies between A_L and A_{MAX}

- The desired single-tone frequency = $F_s(i_{MAX} + FII_L)/N$
- The desired single-tone peak amplitude = $|A_{MAX}|\sqrt{2}\left(\frac{1-FII_L^2}{\mathrm{sinc}(\pi FII_L)}\right)$
- The desired single-tone phase = $< A_{\lfloor i_{MAX}+FII_L \rfloor} - 180°[(FII_L + 1) - \lfloor FII_L + 1 \rfloor] + 90°$

Where $< A_{\lfloor i_{MAX}+FII_L \rfloor}$ is the phase of the $\lfloor i_{MAX} + FII_L \rfloor^{th}$ bin, $[(FII_L + 1) - \lfloor FII_L + 1 \rfloor]$ is simply the fractional, non-integer portion of $(FII_L + 1)$, and where FII_L is the left Fractional Interpolation Index = $\left(\frac{|A_{MAX}|}{|A_L|} - 2\right)/\left(\frac{|A_{MAX}|}{|A_L|} + 1\right)$

- If $|A_L| < |A_R|$
  - The actual single-tone lies between A_{MAX} and A_R
  - The desired single-tone frequency = $F_s\ (i_{MAX} + FII_R)/N$
  - The desired single-tone peak amplitude = $|A_{MAX}|\sqrt{2}\left(\frac{1-FII_R^2}{\mathrm{sinc}(\pi FII_R)}\right)$
  - The desired single-tone phase = $< A_{\lfloor i_{MAX}+FII_R \rfloor} - 180°[(FII_R + 1) - \lfloor FII_R + 1 \rfloor] + 90°$

  Where FII_R is the right Fractional Interpolation Index = $\left(2 - \frac{|A_{MAX}|}{|A_R|}\right)/\left(\frac{|A_{MAX}|}{|A_R|} + 1\right)$

3.3.3 NOISE DENSITY EVALUATION

3.3.3.1 Operation Flow

The noise density evaluation operation flow is very similar to that of single tone extraction described in Fig. 3.10, except for the last step, where processing of the DFT bins is done. Thus, for the first three steps shown in Fig. 3.10, refer to Section 3.3.2. The last step, processing of the DFT bins to integrate the noise density, is covered next in Section 3.3.3.2, with all the nomenclature and analysis developed in Section 3.3.2 being maintained and understood.

3.3.3.2 Processing of the DFT Bins

Evaluating noise density (ND) is done over a desired band of interest with specific beginning (F_{start}) and end (F_{stop}) frequencies. Given these frequency band limits, the evaluation of noise density can be done as shown below given the following necessary definitions. A_i is the DFT bin at index i referenced to $1V_{RMS}$ (according to the amplitude scaling done in Section 3.3.2.2). i_{start} and i_{stop} are the indices of the spectral bins corresponding to the closest frequencies to F_{start} and F_{stop}, respectively.

$$ND\left(dBm/_{Hz}\right) = 10\log_{10}\left(\frac{10^3 \sum_{i=i_{start}}^{i_{stop}} |A_i|^2}{Z_0\left(\left(F_{stop} - F_{start}\right) + BW_C\right)W_C}\right) \tag{3.14}$$

where Z_0 is the system impedance (i.e. 50 Ω), BW_C is a compensation factor for the bandwidth error resulting from computing the noise bandwidth exactly as $\left(F_{stop} - F_{start}\right)$, due to misalignment between each of F_{start} and F_{stop} and the band edges defined by the closest spectral bin, and where W_C is a compensation factor for the equivalent noise bandwidth of the used window (i.e. Hann window, in this case) being other than that of a flat window.

To properly express BW_C, first consider Fig. 3.17, which shows the various scenarios of such misalignment. The blue shaded areas shown in Fig. 3.17 are frequency bands whose energy is included in the $\sum_{i=i_{start}}^{i_{stop}} |A_i|^2$ expression in (3.14), but which are not accounted for in the expression of noise bandwidth $\left(F_{stop} - F_{start}\right)$. Assuming the noise density does not change significantly over the bandwidth of a single spectral bin, the noise density can be corrected by adding the BW_C term to the noise bandwidth $\left(F_{stop} - F_{start}\right)$ term when calculating the noise density. $F_{Res} = F_s/N$, as defined in Section 3.3.2.4 earlier. BW_C is expressed in (3.15), below.

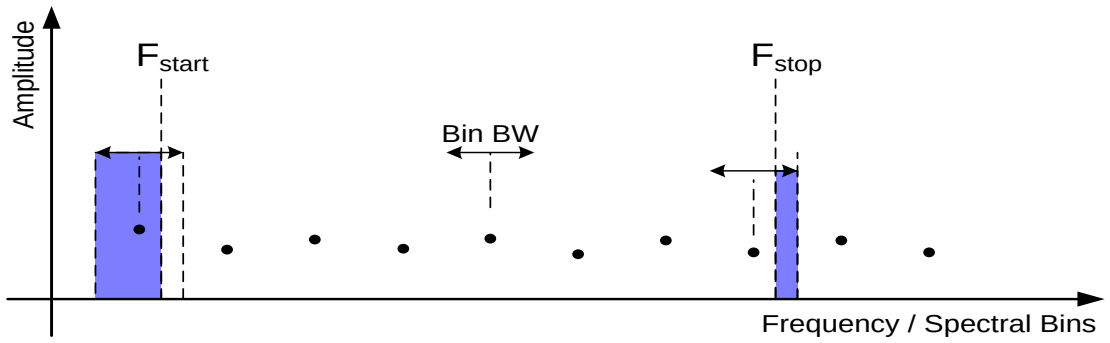

(a)

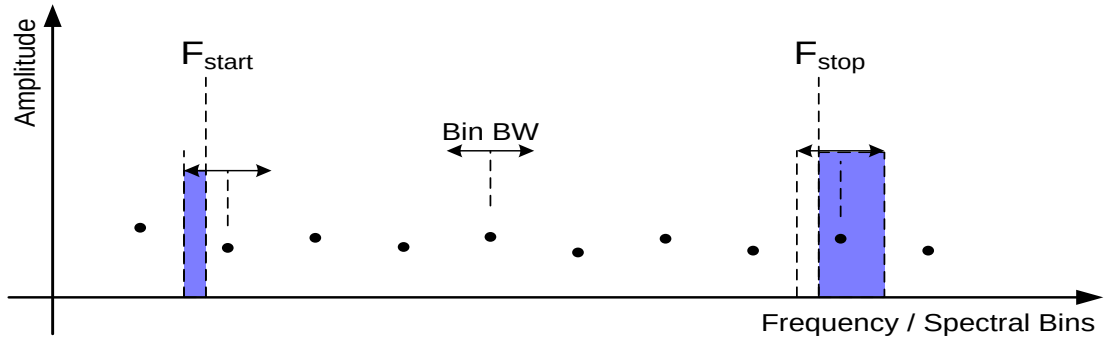

(b)

Fig. 3.17: BW_{error} demonstrated for each of F_{start} and F_{stop} in the two possible scenarios (a) higher than and (b) lower than the closest spectral bin

$$BW_C = F_{Res}\left\{\left(\frac{F_{start}}{F_{Res}} - \frac{2\left[\frac{F_{start}}{F_{Res}}\right] - 1}{2}\right) + \left(\frac{2\left[\frac{F_{stop}}{F_{Res}}\right] + 1}{2} - \frac{F_{stop}}{F_{Res}}\right)\right\} \quad (3.15)$$

where the bracket operator, [ ], in $\left[\frac{F_{start}}{F_{Res}}\right]$ and $\left[\frac{F_{stop}}{F_{Res}}\right]$ indicated rounding to the nearest integer value, with one exception when the operand is an (integer + 0.5) (e.g. 9.5, 10.5, 11.5…etc), in which case, it rounds up for $\frac{F_{start}}{F_{Res}}$ and rounds down for $\frac{F_{stop}}{F_{Res}}$. Accordingly, in the case where F_{start} or F_{stop} are equidistant to bordering bins (i.e. lie exactly in the middle of two bins), the index of the higher bin should be considered as i_{start} in the case of F_{start} while the index of the lower bin should be considered as i_{stop} in the case of F_{stop}.

Regarding the term W_C, it is to compensate for the fact that windowing, while crucial to the process of presenting signal spectra and to extracting single-tone information, actually alters some signal properties, including the noise density level of the signal. Each type of window has an Equivalent Noise BW (ENBW) associated with it, and this ENBW factor can be used to extract correct noise density level from the FFT of the windowed signal. For the Hann window used in the work of this dissertation, ENBW is 1.5. There is more information on ENBW in Hann and other windows in [32].

3.4 Transient Phase-Shift Measurement

3.4.1 Introduction and Operation Flow

Phase shift measurements have been extensively discussed in the literature. The use cases for such measurements range from electro-mechanical systems [33], to power systems and energetics [34], to optical and laser systems [35], and more. Many proposed methods require significant hardware and/or sophisticated instruments. Some methods require the use of heterodyne and sometimes multi-channel receivers [36] [37] [38]. Others require stepped phase modulators and microwave detectors [39]. Some present a system utilizing audio amplifiers, attenuators, bolometers, and synchronous differential null detectors [40]. Other methods address the accuracy aspect and present special calibration schemes using "phaso-meters" [41]. Estimation of the phase-shift between two sine waves (of the same frequency) using Farey Fractions has been proposed in another method. In this method digital circuitry is utilized to generate pulses associated with the sine waves as well as a higher frequency reference pulse. The ratio of counted pulses results in an approximate value of the phase-shift between the two sine waves [42]. Most of the methods described above require significant additional hardware to

perform the phase-shift measurement. Also, they all require the simultaneous presence of the signals (sine waves) whose phase difference is to be found. Finally, they all require that both signals have the same frequency, or that the device under test (DUT) through which the phase-shift occurs is not a frequency-translation device. More recently, specialized instruments such as VNAs were used within custom systems utilizing swept-frequency phase-coherent sources and receivers in measuring phase shifts in mixers [43]. This method requires frequency normalization, phase stitching, and computation of a calibration mixer response for comparison to a measured response. This is in addition to the specialized and sophisticated instrumentation described above, which is necessary if an absolute measure of the phase response of the mixer is desired. However, this is not the case in the problem addressed in this dissertation.

The measurement needed in the methodology's toolbox, as will be further clarified Section 4.3.2, is supposed to capture and assess the phase-shift that the down-converted single tone signal at baseband undergoes as the attenuation level of the RF MTSG signal at the receiver input is changed. Thus, unlike the previous two basic measurements discussed in Section 3.3, this measurement takes place not at a static MTSG level, but exactly during the transition from one MTSG level to another. This is why the measurement is referred to as a transient phase-shift measurement. This measurement is the most sophisticated among all three discussed herein, and it involves 3 stages: an acquisition and transition detection stage, a coherent sine synthesis stage, and a phase-shift computation stage.

3.4.2 ACQUISITION AND TRANSITION DETECTION

3.4.2.1 Signal Acquisition and Event Synchronization

As alluded to in Section 3.4.1, the transition that causes the to-be-measured phase-shift is event-induced, since it results from the MTSG attenuation level change. Thus, to ensure that a baseband signal acquisition contains a transition, one has to either properly synchronize the acquisition with the MTSG level transition event or run signal acquisition asynchronously and continuously in a software thread parallel to that controlling the MTSG transition (with the MTSG transition also taking place continuously back and forth between two given attenuation levels) and monitor the acquired signal for a transition to take place. Because the acquired data is used to compute the phase-shift that the single tone signal underwent, it is important to have an acquired record that sufficiently spans the signal before and after the transition. It is not sufficient to acquire the signal right after the transition or even exactly during the transition, as will be further discussed in Section 3.4.2.5.4. As a result of the latter requirement, synchronous signal acquisition cannot be triggered by the MTSG attenuation level change event unless a properly buffered acquisition is set up for the operation, since the acquisition needs to include a long enough data record of the signal before the transition to accurately compute the phase shift as discussed in 3.4.2.5.4. Alternatively, MTSG level change events can be pre-padded with an acquisition trigger followed by a specific delay that ensures that the pre-transition record length is adequate.

3.4.2.2 Synchronous Triggered Acquisition

As briefly mentioned 3.4.2.1, there are two general methods to address the synchronous acquisition problem. The first method is to have the MTSG level change event trigger buffered acquisition that contains data record preceding the trigger point.

The second method is to have the MTSG level change event be pre-padded with standard (non-buffered) acquisition followed by properly chosen delay. Fig. 3.18 demonstrates the first method, where the MTSG level change event simultaneously triggers the MTSG transition and the buffered acquisition. D_{AcqT2S} designates the delay between the acquisition event trigger and the actual (buffered) acquisition start time. $D_{TranT2S}$ designates the delay between the MTSG level change event trigger and the actual transition start time. The latter two delays result partially from system software latencies and need to be accounted for if such a synchronous acquisition approach is used.

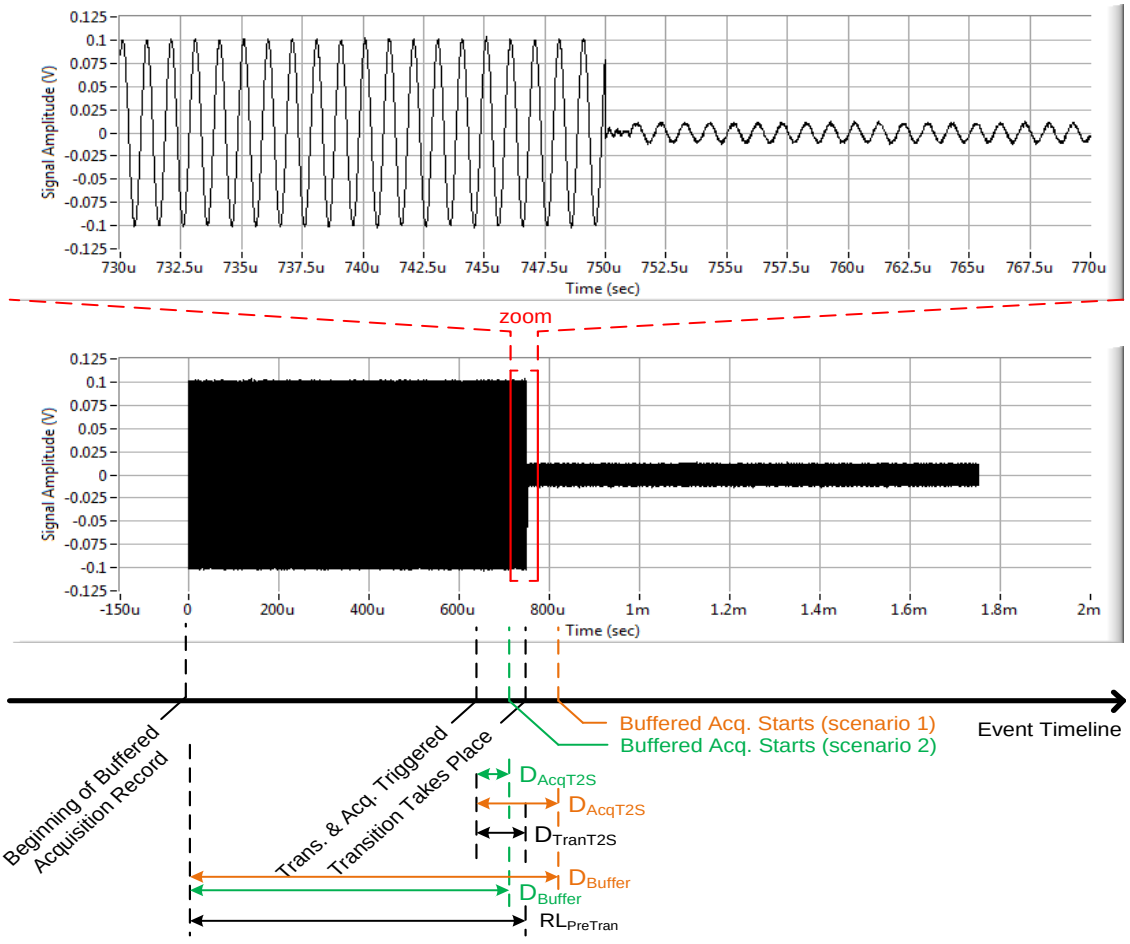

Fig. 3.18: Phase-Transition and buffered acquisition event timeline

Using Fig. 3.18, we formulate the needed buffer length for capturing an adequate pre-transition record length. Fig. 3.18 shows two possible scenarios (colored in green and orange) concerning the timing of the actual buffered acquisition start in relation to the actual transition start. We consider these two scenarios so as not to assume any particular inequality between D_{AcqT2S} and $D_{TranT2S}$. Considering scenario 1 (orange), where $D_{AcqT2S} > D_{TranT2S}$, it follows that for a desired pre-transition record length $RL_{PreTran}$, the buffer depth D_{Buffer} should be expressed as in (3.16) below.

$$D_{Buffer} \geq RL_{PreTran} + (D_{AcqT2S} - D_{TranT2S}) \tag{3.16}$$

Considering scenario 2 (green), where $D_{AcqT2S} < D_{TranT2S}$, D_{Buffer} can be expressed as in (3.17) below. Note, that (3.16) and (3.17) are the same inequalities, only written differently for easier correlation to Fig. 3.18.

$$D_{Buffer} \geq RL_{PreTran} - (D_{TranT2S} - D_{AcqT2S}) \tag{3.17}$$

Fig. 3.19 demonstrates the second synchronous acquisition method, where the MTSG level change event is primed with standard (non-buffered) acquisition followed by a carefully chosen delay, $D_{Acq2Tran}$. Note that the delay is defined to start from the acquisition trigger, and not from when the actual acquisition starts, and its end defines the transition trigger. From Fig. 3.19 one can express $D_{Acq2Tran}$ as in (3.18) below.

$$D_{Acq2Tran} \geq RL_{PreTran} - D_{TranT2S} + D_{AcqT2S} \tag{3.18}$$

The expression for $D_{Acq2Tran}$ is no different from the expression of D_{Buffer} in either of its scenarios. Thus, whichever method of synchronous acquisition is used, knowing the inherent delays involved is necessary to design the acquisition for proper coverage of the pre-transition record length according to (3.16), (3.17), or (3.18).

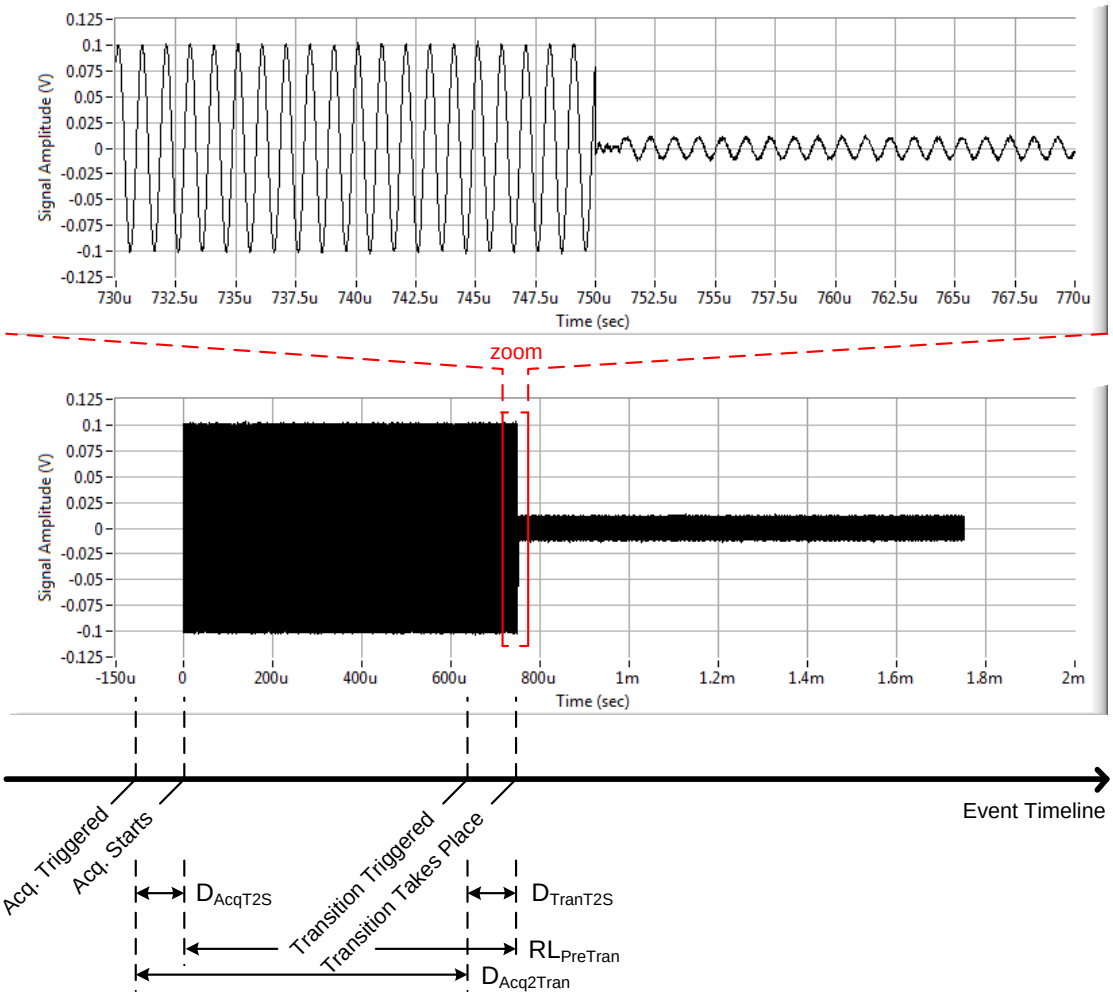

Fig. 3.19: Phase-transition and acquisition-primed transition event timeline

3.4.2.3 Asynchronous Parallel Acquisition

As introduced in Section 3.4.2.1, the asynchronous operation is where the MTSG transition and the signal acquisition events run in parallel, independent threads. While this method relieves the timing constraints, it can be less efficient than the synchronous method, due to the possible acquisition of frames that may not include a transition, which then have to be discarded. However, careful setting of acquisition parameters that will be discussed in detail in Section 3.4.2.5 can greatly improve the method's efficiency. In the

experimental work of this dissertation, the asynchronous method was the one chosen and implemented as the easier and less hardware-demanding of the available options.

3.4.2.4 Transition Detection

3.4.2.4.1 Overview

As defined in Section 3.4.2.2, properly designed synchronous acquisition methods automatically guarantee a transition event getting captured in acquired signal frames. The transition detection aspect of the methodology is thus primarily discussed for the asynchronous acquisition's sake, since an acquired frame does not necessarily contain a transition, as mentioned in Section 3.4.2.3. The asynchronous method relieves the timing constraints and shifts the complexity to post-acquisition signal processing. This signal processing has to be fast in determining whether an acquired frame contains a transition or not and if so, whether the transition occurs sufficiently centered in the acquired record, so that it includes enough signal data before and after the transition to accurately compute the transient phase-shift as further discussed in 3.4.2.5.4. A custom signal processing method was developed for this transition-detection purpose. While the goal is to detect the transition to measure the resulting phase-shift, it is also given that such a transition does induce an amplitude change as well, because in the end it is resulting from the MTSG attenuation level change. Thus, this developed transition detection method is amplitude based and uses a small number of operations. It is experimentally shown to be efficient and fast in making a decision on whether a captured frame contains a desired transition, with sufficient pre- and post-transition waveform length.

3.4.2.4.2 Windowed-RMS Stage

The transition detection method operates on the time domain baseband signal and can be divided into two stages. The first stage takes in the raw baseband signal, such as

the one shown in the zoomed-in plot in Fig. 3.20, and computes its RMS envelope. This changes a sine signal transition, which involves an amplitude and a phase change as well as a potential transient that contains higher frequency contents, to a simpler step function-like signal, such as the one shown in Fig. 3.21. The specific example shown in Fig. 3.20 and Fig. 3.21 correspond to around a -1 dB step. The RMS envelope computation done in the first stage requires operating on a specific window size, W_{RMS}, which is a fixed

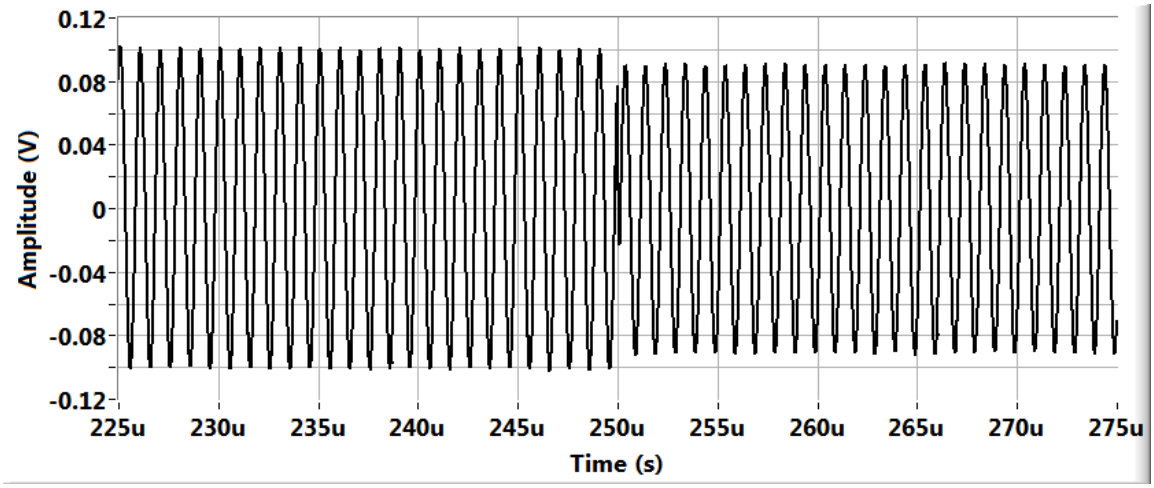

Fig. 3.20: Raw baseband signal zoomed-in at transition

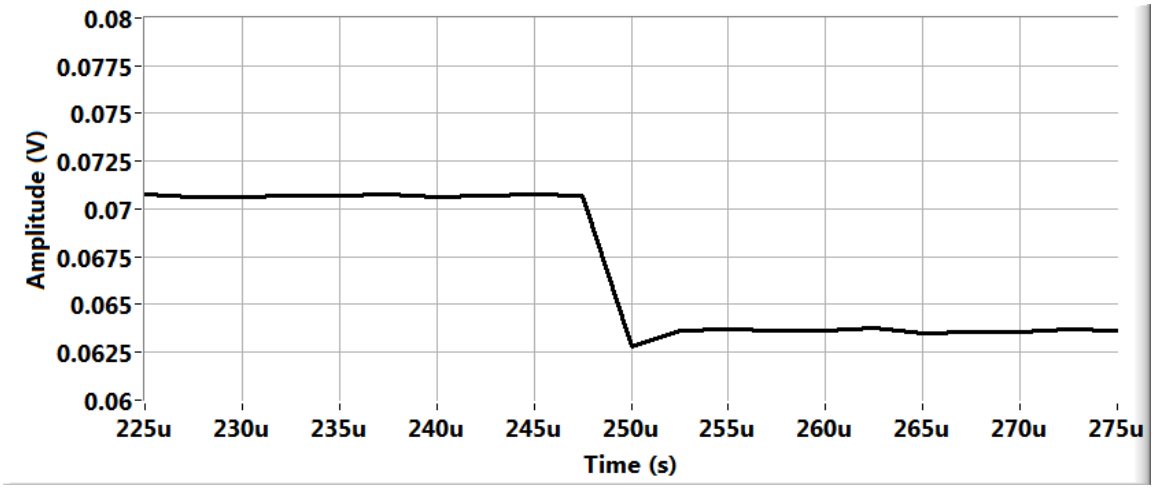

Fig. 3.21: Processed baseband signal zoomed-in at transition

number of samples. It is an integer number of half-cycles of the fundamental baseband frequency, as computed in (3.19), where F_{Samp} is the baseband sampling frequency, F_{BB} is the fundamental baseband frequency, and where k is an integer multiplier. From the raw baseband waveform, each block of W_{RMS} samples are taken and replaced with their single equivalent RMS value, sequentially.

$$W_{RMS} = k\frac{F_{Samp}}{2F_{BB}} \tag{3.19}$$

For completeness, the RMS value is defined as the root-mean-square of the input block or array of W_{RMS} elements. Thus, each block or array of W_{RMS} elements first goes through a squaring function, then the mean/average of the resulting squares is computed, before a square-root is applied to the single resulting mean/average value.

This means that for a number of acquired frame samples N_{AcqFrm}, which is the total number of points in the non-zoomed-in version of Fig. 3.20, the processed waveform whose zoomed-in version is in Fig. 3.21 contains only N_{PrcFrm} samples.

$$N_{PrcFrm} = \frac{N_{AcqFrm}}{W_{RMS}} \tag{3.20}$$

The choice of the integer multiplier k shown in (3.19), while not very critical to the success of the detection event, determines or influences two things. First, it directly affects the RMS window size used. This determines the time resolution of the processed signal frame, as indirectly indicated in (3.20), where the same acquired signal time is divided in the case of the processed waveform over a smaller number of points, and where each of the processed waveform signal points represents W_{RMS} points of the raw acquired waveform signal. Second, it affects the processing time needed to determine whether a captured frame contains a proper transition or not.

3.4.2.4.3 FOM Computation Stage

The second stage of the transition detection method operates on the step function-like waveform signal represented in the processed frame. It computes a single value, FOM_{Trans}, which is a figure of merit for the processed frame, whose value increases with the appropriateness of the transition included in the waveform and is theoretically (excluding noise effect) zero if a transition is not present.

$$FOM_{Trans} = \frac{\sigma_{PrcFrm}}{\mu_{PrcFrm}} \tag{3.21}$$

The terms σ_{PrcFrm} and μ_{PrcFrm} are the standard deviation and the mean, respectively, of all the points of the step-like waveform in the processed frame. To visualize how the value of FOM_{Trans} corresponds to the appropriateness of the waveform transition, consider the plot shown in Fig. 3.22. The FOM_{Trans} (unit-less) is plotted versus the location of the transition within the waveform (in % of the total waveform length), where the transition location is swept from 0.1% to 99.9% in steps of 0.1%, and where 0.1%

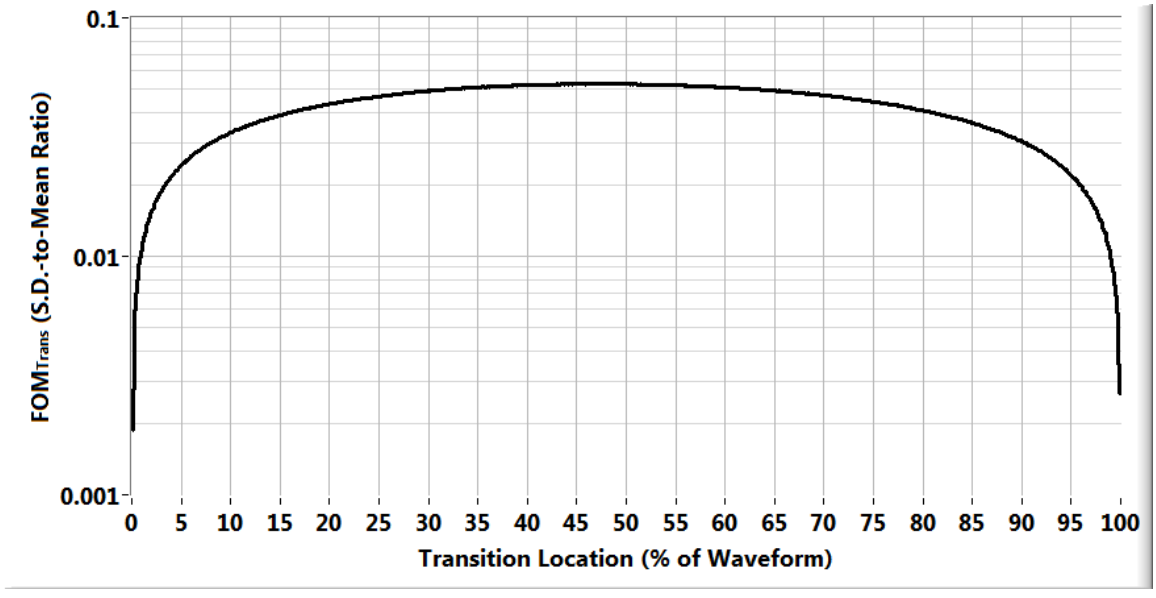

Fig. 3.22: FOM_{Trans} vs. the location of the transition within the waveform

means that the transition occurred almost at the beginning of the frame and 99.9% means that the transition occurred almost at the end of the frame. As can be seen in Fig. 3.22, the value of FOM_{Trans} is maximized when the transition is centered within the processed frame and drops to low values when the transition occurs towards either of the processed frame ends. Consequently, one can specify a threshold for FOM_{Trans}, above which the processed frame, and thus the acquired frame, is considered acceptable, as it contains a transition sufficiently-centered within the acquired frame. Quantifying how well-centered (within an acquired frame) the transition is relates to the frame length and to the minimum pre- and post-transition data records required for accurate phase-shift computation, as discussed in 3.4.2.5.4. For example, if the pre- or post-transition portions of the acquired frame need to be at least 100 μsec each and the frame length is 0.5 msec, then the FOM_{Trans} threshold can be chosen as the larger of the FOM_{Trans} values shown in Fig. 3.22 at 20% and 80%, which for the -1 dB step example considered herein is 0.0435. Note that while the FOM_{Trans} plot shown in Fig. 3.22 looks symmetrical, it actually is not. Furthermore, the FOM_{Trans} plot would be flipped horizontally about a vertical axis that passes through the 50% transition location if the step sign changes. Thus, for a +1 dB step, the FOM_{Trans} value at 20% becomes that at 80% and vice-versa, leaving the larger of the two the same as in the -1 dB step case.

While the experimental work of this dissertation utilized a MTSG hardware scheme that offers a 1 dB level stepping capability, FOM_{Trans} for steps other than 1 dB is computed for a selection of stepping schemes. Results are presented in Fig. 3.23 and Fig. 3.24, where the transition location is swept from 1% to 99% with a 1% step. Note that the FOM_{Trans} algorithm yields more symmetrical results for smaller step transitions. This means that for higher level transitions, the transition location ends up being biased

to either a higher or lower percentage of the acquired frame, for down or up transitions, respectively.

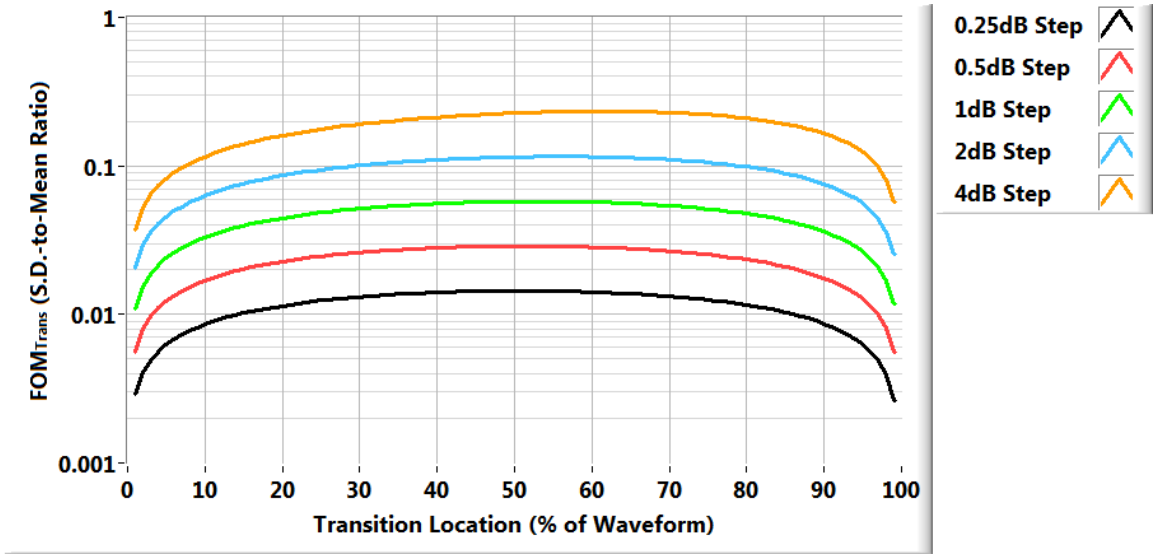

Fig. 3.23: FOM_{Trans} vs Trans. Loc. for various stepping schemes (stacked)

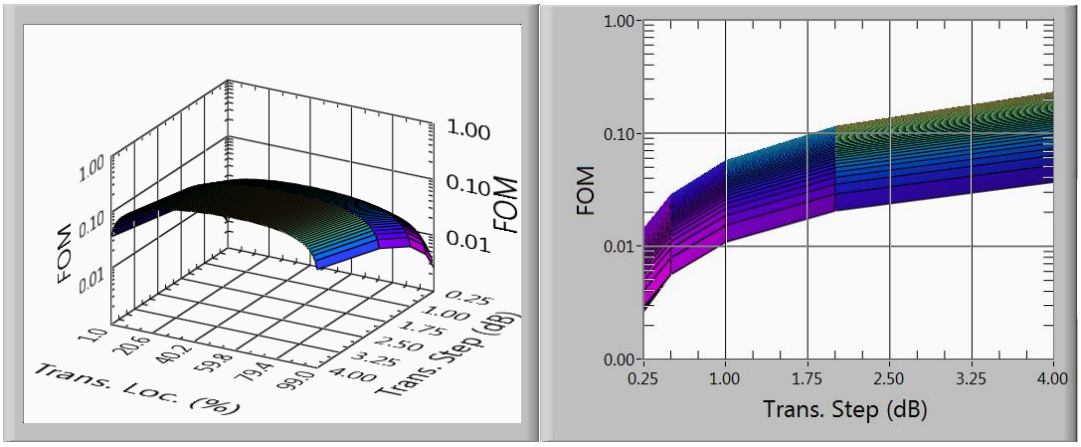

Fig. 3.24: FOM_{Trans} vs Trans. Loc. for various stepping schemes (3-D)

For an acceptable 20% minimum requirement on pre- and post-transition data, this algorithm works well up to at least 10 dB gain steps. For gain-transitions beyond 10 dB, the FOM definition can be improved to yield a symmetric profile versus the transition location at the cost of a slight increase in computation time. The expression for FOM_{Trans_Sym}, the improved and symmetric FOM, is presented in (3.22)

$$FOM_{Trans\_Sym} = \frac{\sigma_{PrcFrm}}{\mu_{PrcFrm}} \times \frac{\sigma_{1/PrcFrm}}{\mu_{1/PrcFrm}} \tag{3.22}$$

where $\sigma_{1/PrcFrm}$ and $\mu_{1/PrcFrm}$ are the standard deviation and the mean, respectively, of the inverse of all the points of the processed step-like waveform. The symmetric FOM computation takes only slightly more than the standard FOM computation because the change is at the processed waveform level, which contains relatively a small number of points. Fig. 3.25 shows the symmetric FOM, FOM_{Trans_Sym}, for 6 levels, with 8 dB, 16 dB, and 32 dB added on the upper end to the transition levels simulated earlier . Note that in Fig. 3.25, all FOM plots shown are symmetrical.

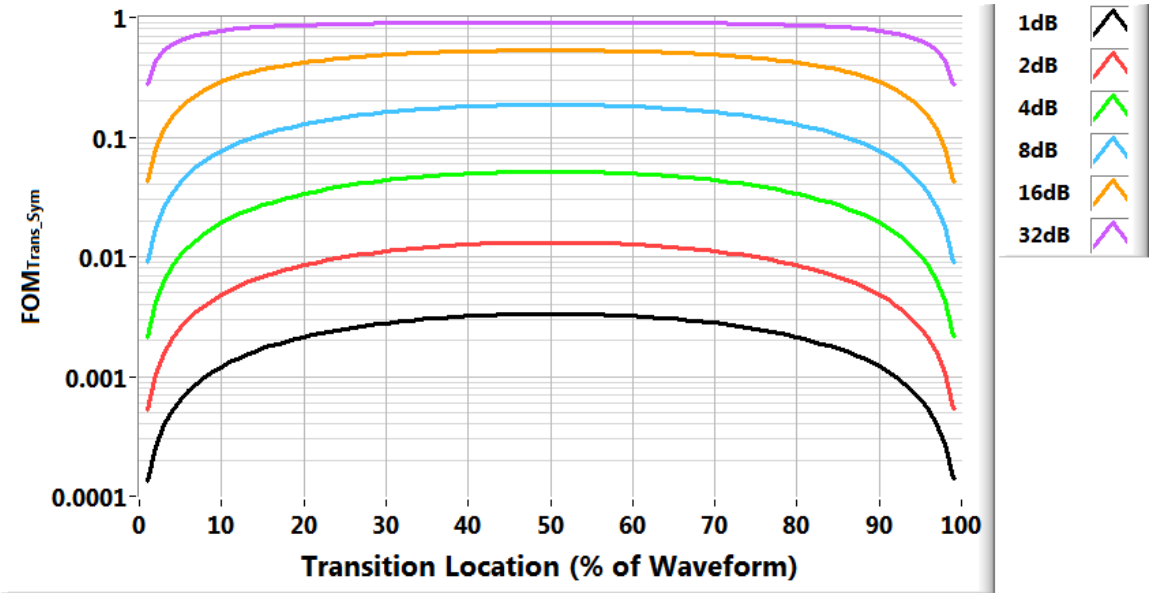

Fig. 3.25: FOM_{Trans_Sym} for transition levels up to 32 dB

Fig. 3.26 shows plots of the symmetric FOM for the same transition levels considered in Fig. 3.25, but with noise considered in the simulation. The FOM of each of the transition levels is shown in 11 SNR cases (10 dB, 11 dB, 12 dB…20 dB). The SNR in the simulation is defined as the signal-to-noise ratio, where the considered signal is the smaller of the pre- and post-transition signals. The results demonstrate the robustness of the method, where the results of the FOMs for all SNRs from 10 dB to 20 dB overlap, with the exception of the 1 dB transition (lowest group of plots shown in Fig. 3.26) whose plots corresponding to the various SNRs diverge below the 10% and above the 90% transition location. Even for a 1 dB transition, the detection method works well for detecting transitions more centered than 10% to 90%.

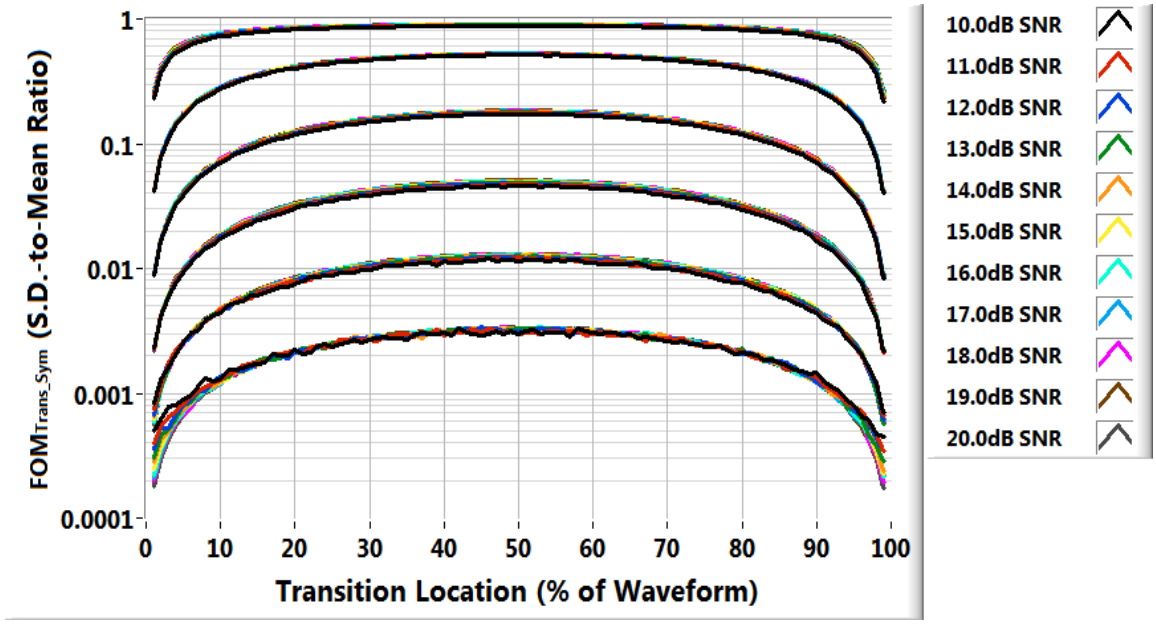

Fig. 3.26: FOM_{Trans_Sym} for transition levels up to 32 dB, each considered with 11 SNR cases (10 dB to 20 dB with 1 dB steps)

3.4.2.5 Acquisition and Transition Detection Efficiency

3.4.2.5.1 Overview

In this section, the efficiency of frame acquisition and transition detection is studied, where the key element considered is the time it takes to arrive at a successful acquisition; that is an acquisition containing an appropriate, centered enough transition. Similar to Section 3.4.2.4 on transition detection, this section on the efficiency of acquisition and transition detection pertains primarily to the asynchronous scheme, as the synchronous methods, if designed as discussed in Section 3.4.2.2, guarantee success on each acquisition, albeit requiring timing and triggering as also discussed in the same section.

3.4.2.5.2 Transition Event Thread

As introduced in Section 3.4.2.1 and further defined in Section 3.4.2.3, the asynchronous acquisition scheme consists of two parallel threads that run independently, requiring no synchronicity, triggering lines, or special timing. One of the threads is the one that controls the transition events on the MTSG hardware. This thread simply contains the software that controls and switches the MTSG attenuation level back and forth between the two desired and consecutive attenuation levels. The frequency of switching the MTSG hardware in this thread is arbitrary. It is only limited on the upper end by the hardware rise/fall and settling times on the digital-step attenuators and by the computer/controller capability to control the MTSG hardware fast enough. The digital-step attenuators used have rise/fall and settling times in the μsec range, as listed in [28] and [29]. Consequently, the transition event can be designed to have a frequency in the tens or perhaps a hundred kHz, if the computer/controller permits. For simplicity, and not to seek to push limits of this aspect of the previously mentioned hardware, an upper limit

of 10 kHz is arbitrarily chosen. Thus, the first thread, controlling the MTSG transition events, can be designed (programmed) to switch periodically at any frequency at or lower than 10 kHz.

3.4.2.5.3 Acquisition Event Thread

The other thread is the one in which consecutive acquisition and transition detection takes place. This thread contains the software that continuously acquires frames of the baseband waveform, processes each of these frames, and makes a decision on whether the captured frame actually contains a transition in the desired manner, as discussed in Section 3.4.2.4. If a transition is found it halts the loop and delivers the captured frame, otherwise it continues looping. The frequency at which this thread can run is dependent on more elements compared to the previously discussed transition event thread. To understand the constraints on how fast this thread can run, consider one period of this thread. Every period of this thread, when it is looping, consists of three time slots. First, there is a timeslot for sampling the waveform. Second, there is a timeslot for transferring or communicating the sampled waveform frame to the computer (assuming a standard digitization method is used, without needing to use a state-of-the-art real-time digitizer that streams directly to the computer). Third, there is a timeslot for processing the frame data and making the decision on whether the captured frame contains the needed transition information. However, using a digitizer with onboard memory, such as the one used in the experimental work of this dissertation (NI PXI-5142), results in technically having only one time slot, the acquisition time slot, with the data transfer and processing occurring during the same time the next acquisition is taking place. This requires that the signal processing (i.e. the decision making in regards to transition detection appropriateness) is relatively fast. Even if the transfer and processing takes

longer than an acquisition time slot, the process can typically continue for many acquisition cycles before the digitizer onboard buffer gets full.

3.4.2.5.4 Acquired Frame Length Criterion

The minimum acquisition time is related to the minimum number of cycles needed before and after the transition, and ultimately on the total number of samples needed. As alluded to earlier, simply acquiring a couple of cycles before and after the transition does not result in an accurate phase-shift measurement, primarily due to phase-noise translated into cycle-to-cycle jitter. Fig. 3.27 and Fig. 3.28 show the measured phase-shift and associated amplitude-step vs. the number of considered cycles (pre- and post-transition). This data is a result of an empirical experiment, in which a single acquired frame was post-processed to generate 500 frames. The first frame contains only 1 cycle on each side of the transition and then gradually the number of cycles is increased by 1 on each side of the transition until reaching 500 cycles and then the measurement is done on each. From Fig. 3.27, it is clear that the measured phase settles at a final value as more cycles are considered in the measurement. From the same data, one can also see that in this case, 100 cycles are sufficient to yield a good measurement, accurate to within ~ 0.1 degree of the final value. Thus, for a 20% minimum requirement of pre- and post-transition data on the transition detection algorithm, the frame length will need to be 500 cycles long for the considered example, which for the used 1 MHz baseband signal is 0.5 msec. For the timing diagram discussed next, the second and third time slots are not considered, or assumed hidden behind the acquisition time as discussed earlier. This assumption is fair as long as the number of acquisitions needed is such that the digitizer's onboard memory is sufficient. A single acquisition of the ones discussed here (i.e. 0.5 msec long) comprises 50kS at the 100MS/s rate of the NI PXI-5142 digitizer. The

onboard memory (64MB and 256MB options available) allows for at least 32MS, which translates to at least 640 0.5 msec-acquisitions, which is a couple of orders of magnitude more than what is needed for an optimized asynchronous acquisition, as shall be seen later on.

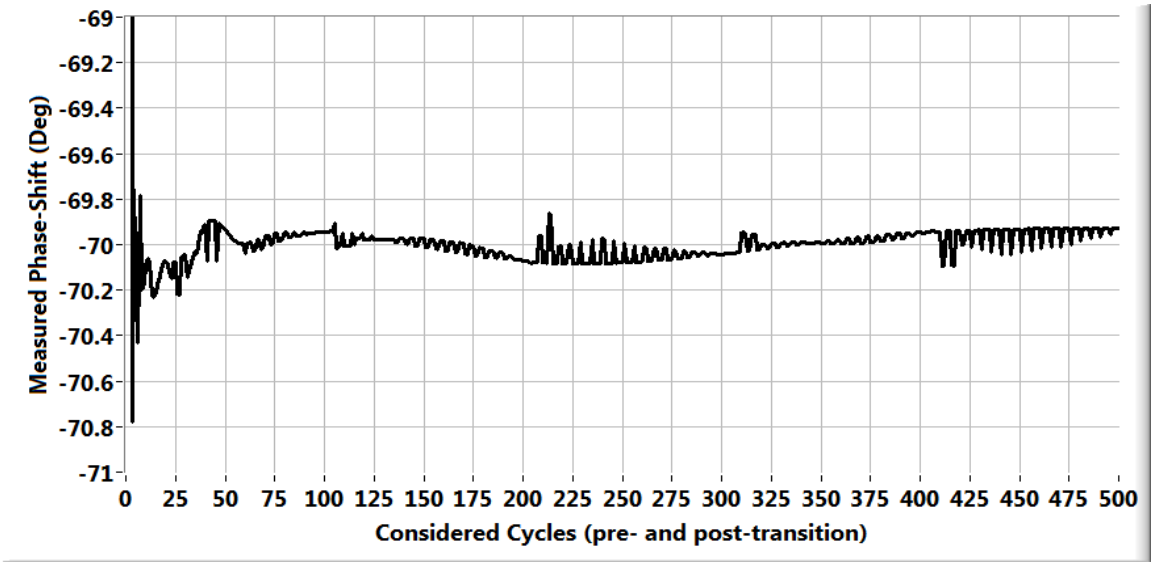

Fig. 3.27: Measured phase-shift vs. number of considered cycles

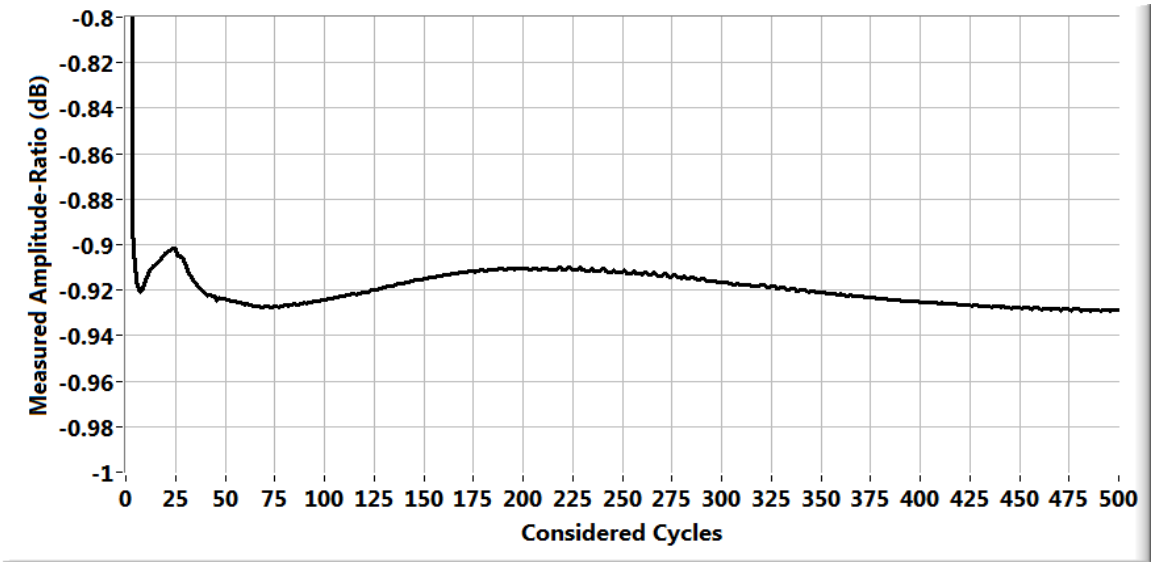

Fig. 3.28: Measured gain-step vs. number of considered cycles

3.4.2.5.5 Transition and Acquisition Event Timeline

Fig. 3.29 shows an event timeline where acquisition events (or acquired frames) are presented at consecutive rectangular blocks, whose time span is 0.5 msec each, and where transition events are presented as impulses. The frequency of the acquisition event blocks, f_{Acq}, is determined by the acquisition length needed, which was found earlier to be 0.5 msec. Thus, the acquisition events repeat at a 2 kHz rate. The transition event frequency, f_{Trans}, which is controlled by the first thread, is arbitrary as discussed earlier, and thus can be used to optimize the asynchronous acquisition efficiency as long as it does not exceed the hardware limit of 10 kHz, set earlier. However, given the acquisition repeat frequency of 2 kHz, the transition event frequency can also not exceed 2 kHz, in order not to have a case where one acquisition contains two transitions. Note that the two events shown on the timeline in Fig. 3.29 are non-coherent. Consequently, for a given transition event frequency, such as the one shown in Fig. 3.29, the entire transition event plot can be shifted laterally in time (left or right) for up to a whole cycle of the transition event. The actual coincidence of a transition event in the middle of (or well-centered in) the first acquisition cycle cannot be used to judge acquisition efficiency. In fact, to find the optimum f_{Trans}, the phase of each simulated transition event should be swept from 0 to 360 degrees (in steps of 1 or 0.1 degrees, for example) and at each phase the first transition event in time that lies within the successful transition threshold (say 20% to 80% of acquired frame) gets reported. The first successful capture time for a given f_{Trans} is considered as the worst-case time across all the swept phases for that given f_{Trans}. This is because in this asynchronous scheme, there is no control over the phase at which the transition event starts relative to the acquisition event.

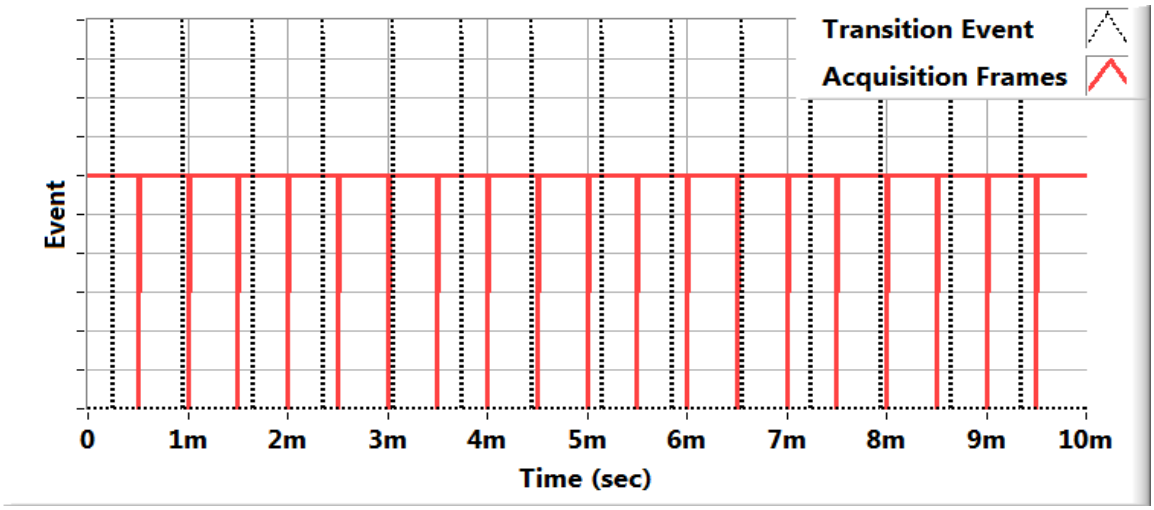

Fig. 3.29: Event timeline showing acquisition and transition events

Because of the asynchronous nature of the acquisition, it is possible, for a non-optimized acquisition to theoretically take infinite time before a successful acquisition takes place. An example of the latter scenario is demonstrated in Fig. 3.30, where a bad choice of 2 kHz was made for f_{Trans}. The reason why 2 kHz is a bad choice for f_{Trans} (as well as 1 kHz, 666.67 Hz, 500 Hz... etc), is that for a few starting phases, which correspond to where the first transition event occurs at either edge of the first acquired

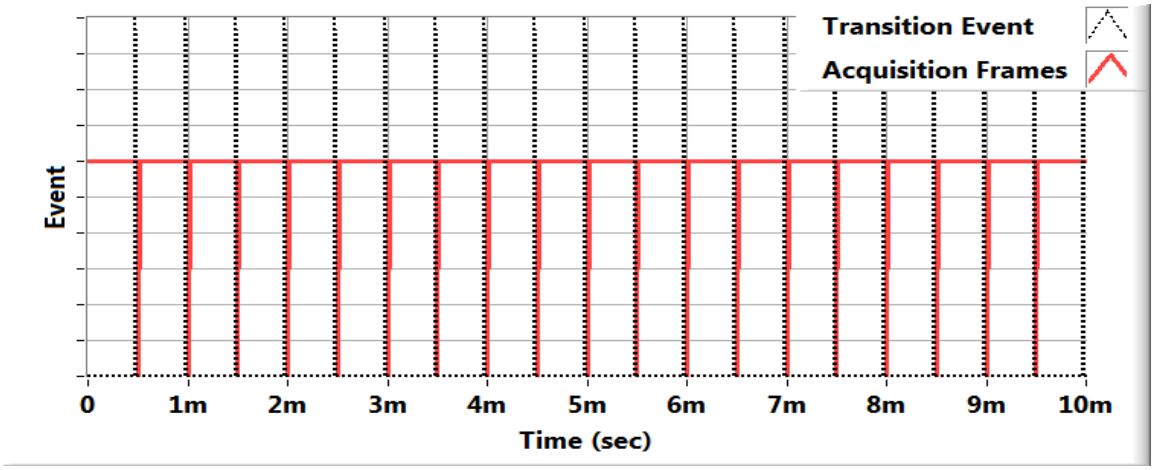

Fig. 3.30: Event timeline showing bad transition event frequency choice

frame, the transition event continues to always occur at the same location within the acquired frame, because f_{Acq} is an integer-multiple of chosen f_{Trans}. There are starting phases where the same 2 kHz f_{Trans} yields a first successful acquisition in less than 0.5 msec, but that should not be considered in the optimization process. Only the worst-case phase should be considered because there is no control over the start phase between the two events.

Fig. 3.31 shows the worst-case (in regards to start phase) first successful capture time versus the transition frequency, f_{Trans}. For each of the points shown in Fig. 3.31, a 0-to-360 degrees phase sweep was made to find the worst-case first successful capture time. For the given problem, with 0.5 msec acquisition time and 20%-to-80% transition-location threshold, the optimum transition frequency was found to be 1430 Hz, the minimum shown in Fig. 3.31. Fig. 3.32 shows the first successful capture times for a f_{Trans} of 1430 Hz versus the swept initial phase; a similar plot can be shown for each of the f_{Trans} points shown in Fig. 3.31. Note that the first successful capture time can be as low as 100 μsec, just enough to get the 20% threshold on the lower edge of the first acquired frame, or as high as 1.3 msec, which is the value reported in Fig. 3.31, and which lies in the third acquisition. In conclusion, while the scheme proposed is asynchronous, requiring no special triggering or timing, as introduced in Section 3.4.2.3, it was demonstrated in this section to provide efficient transition detection when the transition event frequency is chosen methodically. By properly designing the transition event frequency, not only can lengthy transition detection attempts or "harmonic race conditions" be easily avoided, but it can also be designed such that there is a cap on the maximum number of acquisitions needed before a successful one is achieved, and this

cap can be optimized to as few as three acquisitions, for a 0.5 msec acquired frame length and 20%-to-80% transition-location threshold.

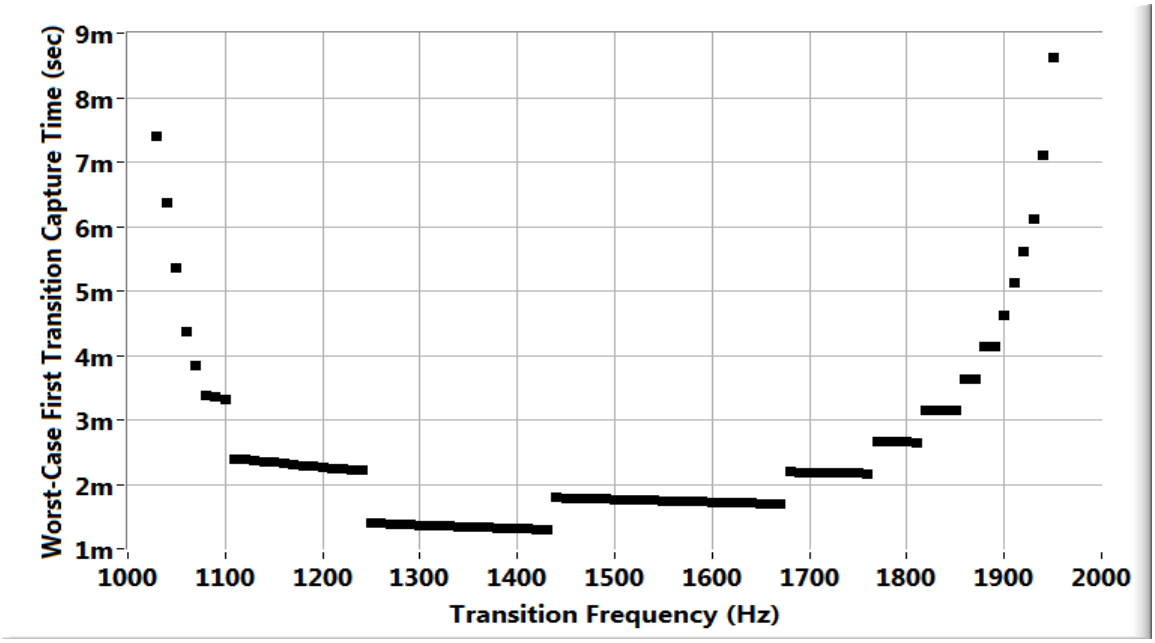

Fig. 3.31: First successful acquisition time vs. transition frequency

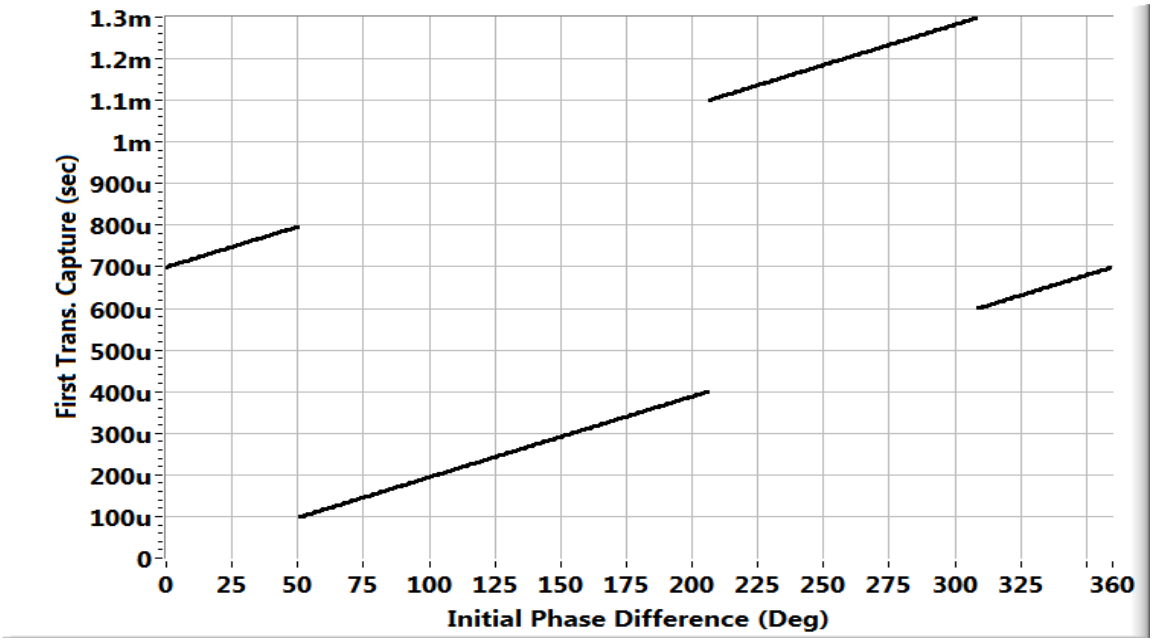

Fig. 3.32: First successful capture time vs. initial phase for 1430 Hz

3.4.2.5.6 Analysis of Event Timeline

In this section, the analysis needed to find the worst-case first successful acquisition time for a given transition frequency, f_{Trans}, is presented. From the results of the previous section, Section 3.4.2.5.5, it can be seen that the worst-case first-successful acquisition time versus f_{Trans} cannot be expressed in a single continuous function, as it is piecewise continuous as shown in Fig. 3.31. Plots such as the ones shown in Fig. 3.31 or Fig. 3.32 can be either generated empirically by means of a transient simulation or derived from event timeline analysis, such as the one presented in this section.

Consider Fig. 3.33, where y_0, y_1, and y_2 are the times at which the first, second, and third transition events take place, respectively. Consequently, y_n is the time at which the $(n+1)^{th}$ transition event takes place. Also in Fig. 3.33, T_{Acq} and T_{Trans} are the periods corresponding to f_{Acq} and f_{Trans}, the acquisition and transition frequencies, respectively. Finally, α is a fraction that corresponds to the minimum required pre- and post-transition waveforms, in terms of the acquired frame length. For the 20% requirement discussed in the example earlier (i.e. the transition is considered successful if located within 20% to 80% of acquired waveform), α is simply 0.2.

Given the above, y_n can be expressed in terms of y_0, n, and T_{Trans} as follows.

$$y_n = y_0 + n\,T_{Trans} \tag{3.23}$$

Because of the incoherency of the acquisition and transition events, the first transition can occur anywhere within the first T_{Trans} time period. Thus y_0 can be expressed as in (2.24).

$$y_0 \in [0\,,\ T_{Trans}[\tag{3.24}$$

Also, because f_{Trans} is limited to f_{Acq} on the upper end, as discussed earlier in Section 3.4.2.5.5, T_{Trans} cannot be less than T_{Acq}. But, there is also no point in making

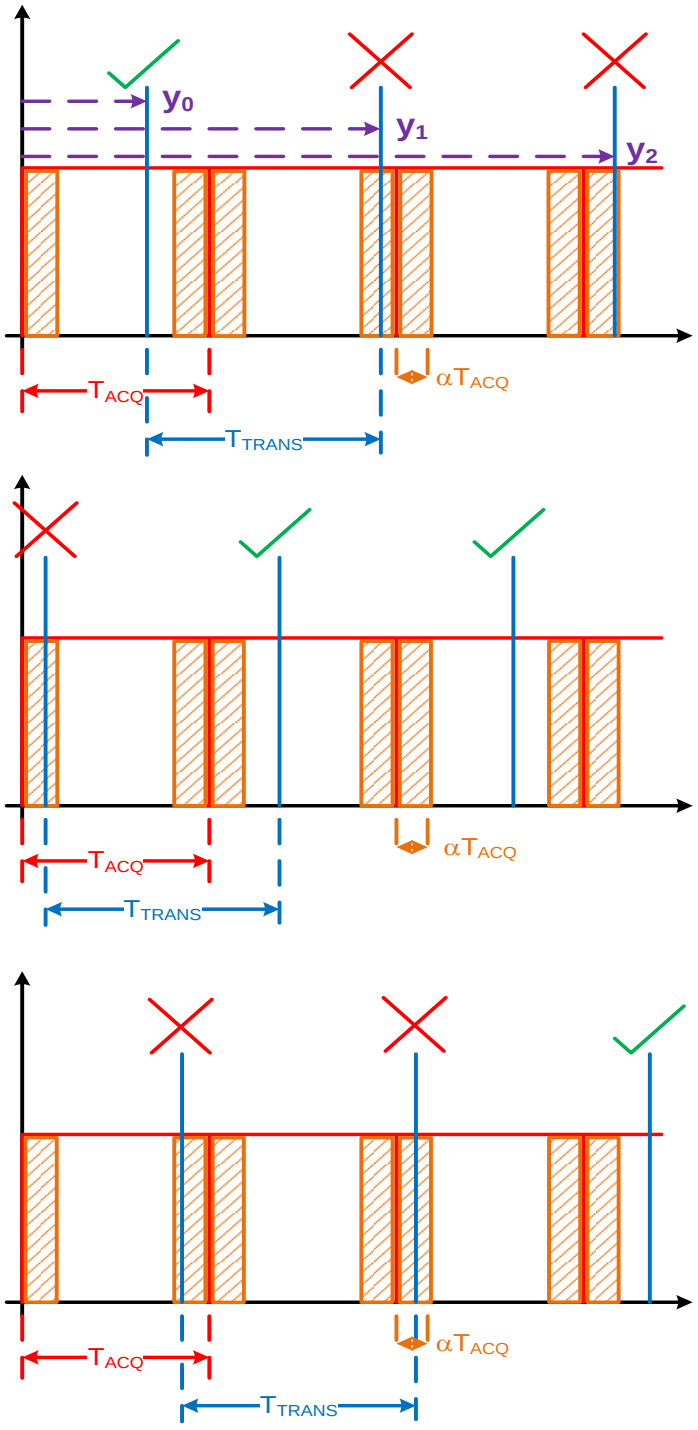

Fig. 3.33: Event timeline showing three examples of various transition-event start phases resulting in success on first acquisition (top), second acquisition (middle), and fourth acquisition (bottom)

T_{Trans} too large, as that makes transition events too spaced out and successful acquisitions will take longer to achieve. In fact, the optimum f_{Trans} is between f_{Acq} and $f_{Acq}/2$. This can be seen in Fig. 3.31, where the worst-case first successful acquisition gets minimized between 1 kHz and 2 kHz, where 2 kHz is the acquisition frequency. Also, as the text beneath Fig. 3.29 describes, at exactly 2 kHz and 1 kHz (and 666.67 Hz, 500 Hz, 400 Hz,..f_{Acq}/n), the system gets into a harmonic race condition, where a transition event start phase, if it results in an unsuccessful acquisition, continues to do so for every acquisition thereafter, resulting in an infinite worst-case first-successful acquisition time. Given that the transition frequencies to be avoided are f_{Acq}, $f_{Acq}/2$, $f_{Acq}/3$, …f_{Acq}/n, it makes sense to limit the search for the optimum frequency to the highest range between f_{Acq} and $f_{Acq}/2$, as expressed in (2.25).

$$\frac{f_{Acq}}{2} \leq f_{Trans} \leq f_{Acq} \;\leftrightarrow\; T_{Acq} \leq T_{Trans} \leq 2\,T_{Acq} \tag{3.25}$$

Given (3.25) and (3.24), one can conclude that depending on T_{Trans}, y_0 can be anywhere in a scaling range from $[0\,,\ T_{Acq}[$, to $[0\,,\ 2\,T_{Acq}[$. Since the acquisition frames, shown in Fig. 3.33 as adjacent red boxes, are divided into three zones each (two orange dashed zones on the frame edges and a clear non-colored zone in the middle), y_0 can be re-expressed to reflect the different zones, as shown in (3.26), where '{ ' reflects the logical OR of the expressed zones. Note that clear or successful zones are inclusive of boundary values, while orange-dashed or unsuccessful zones are exclusive of them.

$$y_0 \in \begin{cases} [0\,,\alpha\,T_{Acq}[\\ [\alpha\,T_{Acq}\,,(1-\alpha)\,T_{Acq}] \\ ](1-\alpha)\,T_{Acq}\,,\mathrm{MIN}(T_{Trans},(1+\alpha)\,T_{Acq})[\\ [\mathrm{MIN}(T_{Trans},(1+\alpha)\,T_{Acq})\,,\mathrm{MIN}(T_{Trans},(2-\alpha)\,T_{Acq})] \\ ]\mathrm{MIN}(T_{Trans},(2-\alpha)\,T_{Acq})\,,\mathrm{MIN}(T_{Trans},2\,T_{Acq})\,[\end{cases} \tag{3.26}$$

To find the worst-case (with respect to transition start phase) first successful acquisition, y_0, the time of the first transition event, has to be assumed not in the clear zone of an acquisition cycle that lie within the first transition period T_{Trans}, as such a condition results from the coincidence of two non-coherent events, and shall not be relied on for finding the worst-case successful acquisition time. Thus to find the worst case first successful acquisition, the second and fourth zones expressed in (2.26) are ignored when evaluating y_0.

Given that y_0 is assumed to be in an unsuccessful zone (an orange dashed zone in Fig. 3.33), it becomes necessary to find out, for a certain T_{Trans}, the value of n that would result in all the unsuccessful zones of y_0 to be mapped to successful zones of y_n or y_k, where k is lower than n. Below, we express the pessimistic, worst-case y_0, as $y_{0_{WC}}$.

$$y_{0_{WC}} \in \begin{cases} [0\ ,\alpha\ T_{Acq}[\\ ](1-\alpha)\ T_{Acq}\ ,\mathrm{MIN}\left(T_{Trans},(1+\alpha)\ T_{Acq}\right)[\\ ]\mathrm{MIN}\left(T_{Trans},(2-\alpha)\ T_{Acq}\right)\ ,\mathrm{MIN}\left(T_{Trans},2\ T_{Acq}\right)[\end{cases} \tag{3.27}$$

Substituting $y_{0_{WC}}$ for y_0 in (3.23) results in y_n as shown below.

$$y_n \in \begin{cases} n\ T_{Trans} + [0\ ,\alpha\ T_{Acq}[\\ n\ T_{Trans} +](1-\alpha)\ T_{Acq}\ ,\mathrm{MIN}\left(T_{Trans},(1+\alpha)\ T_{Acq}\right)[\\ n\ T_{Trans} +]\mathrm{MIN}\left(T_{Trans},(2-\alpha)\ T_{Acq}\right)\ ,\mathrm{MIN}\left(T_{Trans},2\ T_{Acq}\right)[\end{cases} \tag{3.28}$$

The first successfully captured transition, y_n, will be at n that will result in all three zones expressed in (3.28) being in clear zones of acquisition. Clear or success zones of acquisition, similar to the second and fourth expressions in (3.26), can be generalized in the expression below, where m is used to indicate the acquisition number and Z_{SA} stands for zone of successful acquisition; Z_{SA_m} is the zone of success for the m^{th} acquisition.

$$Z_{SA_m} = \left[(m+\alpha)T_{Acq}, (m+1-\alpha)T_{Acq}\right] \tag{3.29}$$

Note that m, and not n, is used to identify the acquisition number, as an n^{th} transition can occur at an m^{th} acquisition, where m and n may be, but are not necessarily equal.

3.4.2.5.7 Examples of Event Timeline Analysis

Considering a few examples of f_{Trans} points taken from Fig. 3.31 helps to crystallize the methodology of finding the worst-case first successful acquisition time and/or the number of first successful acquisition. Starting with the best f_{Trans} found in simulation, given the 20% and 2 kHz f_{Acq} criteria, which is 1430 Hz (found in simulation with 10 Hz resolution sweep; note that actual best frequency is 1428.57 Hz), we first present Table 3.1 below.

Transition Number, n	Zone 1		Zone 2		Zone 3	
	y_n	Z_{SA}	y_n	Z_{SA}	y_n	Z_{SA}
0	[0.0m , 0.1m[	[0.1m , 0.4m][2]	]0.4m , 0.6m[	[0.6m , 0.9m][2]	N/A[1]	N/A[1]
1	[0.7m , 0.8m[	[0.6m , 0.9m]	]1.1m , 1.3m[	[1.1m , 1.4m]	N/A[1]	N/A[1]

[1] Zone 3 is N/A because zones for 1428.57Hz f_{Trans} are limited to 0.7msec, whereas Zone 3 starts at $(2 - \alpha)T_{acq}$ = 0.9msec.

[2] For n = 0, y_n is always picked to be in unsuccessful zones to avoid relying on coincidental success.

Table 3.1: Event timeline analysis for f_{Trans} of 1428.57 Hz

In Table 3.1, y_n is computed from (3.28) for the different values of n for each of the three zones expressed in (3.31). This is expressed in Table 3.1 as Zone 1, Zone 2, and Zone 3, and Z_{SA} is computed from (3.32), where m is chosen so that Z_{SA} corresponds to the same zone as y_n. Only one row after the base, $n = 0$, row was needed for an f_{Trans} of 1428.57 Hz, because success was achieved for $n = 1$, as demonstrated in y_n of each of Zone 1 and Zone 2 lying within their corresponding Z_{SA}. Fig. 3.34 below shows the transient simulation result for the first successful acquisition versus the start phase for f_{Trans} of 1428.57 Hz. The plot is almost indistinguishable from that shown in Fig. 3.32. Note that the short and long top lines in Fig. 3.34 correspond to y_1 (y_n for $n = 1$) for Zone 1 and

Zone 2, respectively, as they range from 0.7 msec to 0.8 msec and from 1.1 msec to 1.3 msec, respectively. The lower lines in Fig. 3.34 belong to the non-considered clear zones for $n = 0$, which are shown in Table 3.1 under Z_{SA} in the first row, ranging from 0.1 msec to 0.4 msec and from 0.6 msec to 0.9 msec for Zone 1 and Zone 2, respectively. Given Table 3.1, the worst-case first successful acquisition time is 1.3 msec, which occurs during the third acquisition, capturing the second transition (or the first considered transition, given actual first transition is ignored).

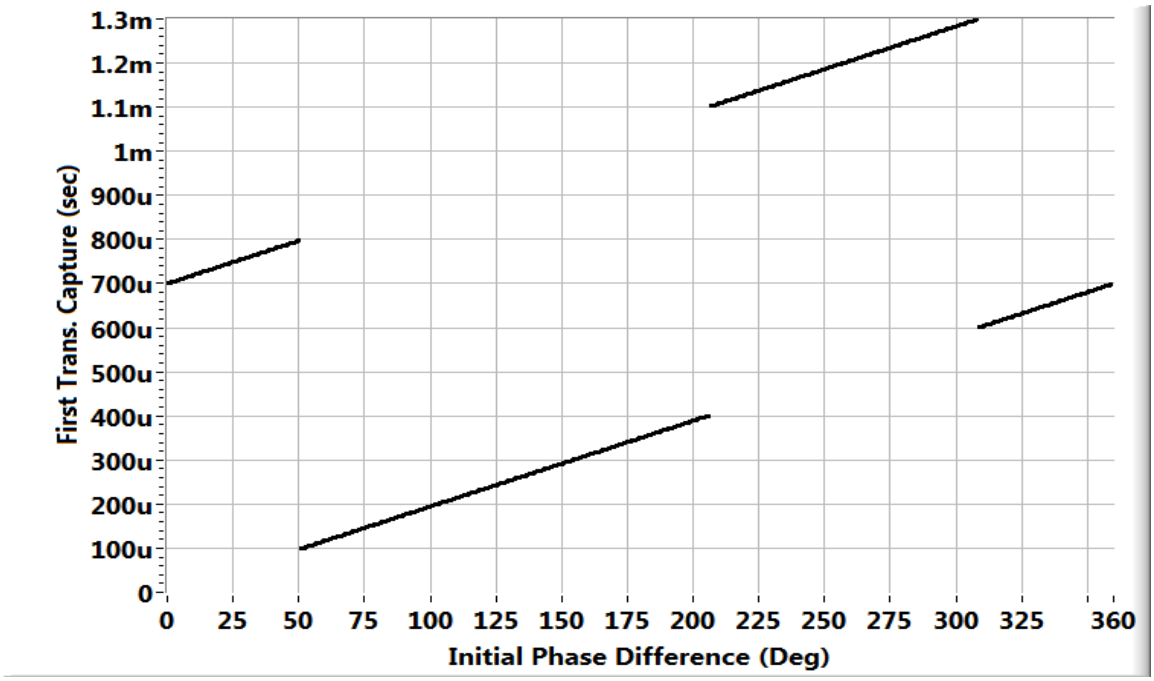

Fig. 3.34: First successful capture time vs. initial phase for 1428.57 Hz

The second example is for one of f_{Trans}= 1900 Hz, an extreme values that come close to the upper edge of the range limited by f_{Acq} and $f_{Acq}/2$. Table 3.2 presents the event timeline analysis for a 1900 Hz f_{Trans} in a similar way to how Table 3.1 does for 1428.57 Hz. This time however, the worst-case time requires analyzing up to the 9th transition to arrive at a successful acquisition. To better understand the table, consider

each zone separately. Starting with Zone 1, go from top to bottom and check for whether the y_n range fits within the Z_{SA} range. For Zone 1, $n = 4$ is the first row that completely satisfies the condition. Note that once the condition is satisfied (for a given zone) at some value of n (call it n_x), then n values above n_x do not matter for that zone. This is because for the given zone, the "first successful acquisition" occurred at or below n_x. In reality, when looking at the simulation plot shown in Fig. 3.35 one notices that even for the row with values of n lower than 4, partial lines exist in the plot, where the corresponding condition is satisfied. Thus, not all the 0.1 msec time (Zone 1), which corresponds to 68.4° for 1900 Hz, is in the range of 2.11 msec to 2.21 msec ($n = 4$). There are lines that correspond to the ranges of n being 3, 2, and 1, in addition to the ignored values corresponding to $n = 0$. Consider $n = 1$, the y_n range of 0.53 msec to 0.63 msec partially satisfies the corresponding Z_{SA} range from 0.6 msec to 0.63 msec. This is why there is a line of values around 0.6 msec, towards the end of Zone 1 (ending with 68.4°). For $n = 1$, the range below 0.6 msec does not pass the success criterion, thus higher levels of n can be the "first successful acquisition" if it is applicable to them. Moving up in n levels happens until the entire zone, Zone 1 in this case, is finished.

Transition Number, n	Zone 1		Zone 2		Zone 3	
	y_n	Z_{SA}	y_n	Z_{SA}	y_n	Z_{SA}
0	[0.0m , 0.1m[	[0.1m , 0.4m][2]	]0.4m , 0.53m[	[0.6m , 0.9m][2]	N/A[1]	N/A[1]
1	[0.53m , 0.63m[	[0.6m , 0.9m]	]0.93m , 1.05m[	[1.1m , 1.4m]	N/A[1]	N/A[1]
2	[1.05m , 1.15m[	[1.1m , 1.4m]	]1.45m , 1.58m[	[1.6m , 1.9m]	N/A[1]	N/A[1]
3	[1.58m , 1.68m[	[1.6m , 1.9m]	]1.98m , 2.11m[	[2.1m , 2.4m]	N/A[1]	N/A[1]
4	[2.11m , 2.21m[	[2.1m , 2.4m]	[2.51m , 2.63m[	[2.6m , 2.9m]	N/A[1]	N/A[1]
5	[2.63m , 2.73m[	[2.6m , 2.9m]	[3.03m , 3.16m[	[3.1m , 3.4m]	N/A[1]	N/A[1]
6	[3.16m , 3.26m[	[3.1m , 3.4m]	[3.56m , 3.68m[	[3.6m , 3.9m]	N/A[1]	N/A[1]
7	[3.68m , 3.78m[	[3.6m , 3.9m]	[4.08m , 4.21m[	[4.1m , 4.4m]	N/A[1]	N/A[1]
8	[4.21m , 4.31m[	[4.1m , 4.4m]	[4.61m , 4.74m[	[4.6m , 4.9m]	N/A[1]	N/A[1]

[1] Zone 3 is N/A because zones for 1900Hz f_{Trans} are limited to 0.526msec, whereas Zone 3 starts at $(2 - \alpha)T_{acq}$ = 0.9msec.

[2] For n = 0, y_n is always picked to be in unsuccessful zones to avoid relying on coincidental success.

Table 3.2: Event timeline analysis for f_{Trans} of 1900 Hz

Following from Fig. 3.35, the line from 68.4° to 273.6° corresponds to the non-considered clear zone, which ranges from 0.1 msec to 0.4 msec. After 273.6°, Zone 2 starts. The first y_n to satisfy the beginning of Zone 2 is y_8, where 4.61 msec clears the lower limit of 4.6 msec. This is why the highest points shown in Fig. 3.35 are around 4.6 msec. However, Zone 2 does not stay at 4.6 msec, and as soon as lower levels satisfy their corresponding conditions, they take over and show up in the plot. For example, level 7 just fails the success range with 4.08 msec being less than 4.1 msec. However, after 0.02 msec, which corresponds to 13.68°, level 7 clears the lower condition and starts showing up in the plot. This is why level 8 only lasts on the plot for exactly 13.68°. The same process continues, going down from one level to another, as seen in Fig. 3.35, from level 8 all the way to level 3, at which point Zone 2 ends.

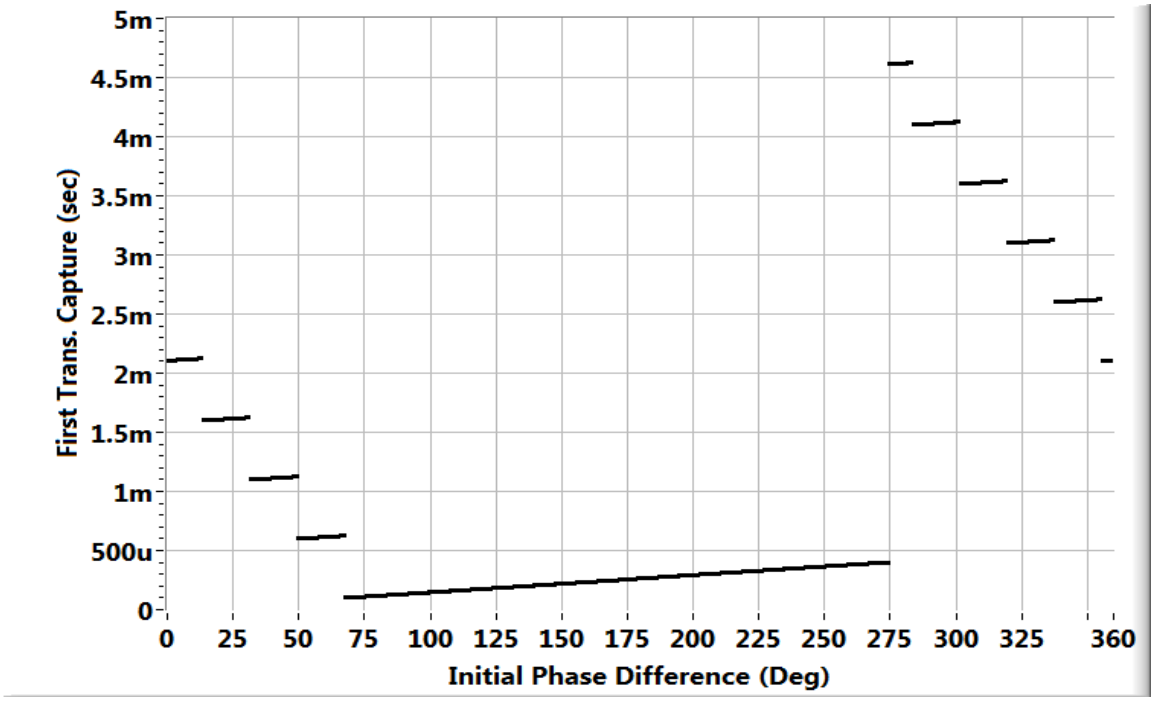

Fig. 3.35: First successful capture time vs. initial phase for 1900 Hz

The third and last example is for an f_{Trans} of 1050 Hz, a frequency that comes close to the lower end of the f_{Acq} to $f_{Acq}/2$ range. Because the period for 1050 Hz is 0.9523 msec, this example actually uses Zone 3, which for an α of 0.2 and f_{Acq} of 2 kHz starts at 0.9 msec. Similar to the previous example, we shall start with Zone 1. The first level to start partially satisfying the corresponding condition is level 3, where 2.86 msec satisfies the success range of 2.6 msec to 2.9 msec. However, level 3 stops satisfying the success condition at 2.9 msec, which is why upper levels get shown on the plot where their conditions are satisfied. Zone 1, 0.1 msec total, is 37.8° for 1050 Hz. After 37.8°, the ignored successful zone starts, from 0.1 msec to 0.4 msec, which ends at 151.2°. Then, Zone 2 starts from level 1, where 1.35 msec satisfies the range of 1.1 msec to 1.4 msec, and then goes in higher levels beyond 1.4 msec, until the maximum level 5 is reached at 5.36 msec at 226.8°. After Zone 2 comes a second ignored success zone, which belongs to the second acquisition, from 0.6 msec to 0.9 msec. Zone 3 starts at 0.9 msec or 340.2°, showing a line from level 1, where the range of y_1 being]1.85 msec , 1.9 msec[satisfies the corresponding Z_{SA} range of [1.6 msec , 1.9 msec].

Transition Number, n	Zone 1		Zone 2		Zone 3	
	y_n	Z_{SA}	y_n	Z_{SA}	y_n	Z_{SA}
0	[0.0m , 0.1m[	[0.1m , 0.4m][1]	]0.4m, 0.6m[	[0.6m , 0.9m][1]	]0.9m , 0.95m[	[0.6m , 0.9m][1]
1	[0.95m , 1.05m[	[1.1m , 1.4m]	]1.35m, 1.55m[	[1.1m , 1.4m]	]1.85m , 1.9m[	[1.6m , 1.9m]
2	[1.90m , 2.00m[	[1.6m , 1.9m]	]2.3m, 2.5m[	[2.1m , 2.4m]	]2.8m , 2.85m[	[2.6m , 2.9m]
3	[2.86m , 2.96m[	[2.6m , 2.9m]	]3.46m, 3.66m[	[3.1m , 3.4m]	]3.76m , 3.81m[	[3.6m , 3.9m]
4	[3.81m , 3.91m[	[3.6m , 3.9m]	[4.21m , 4.41m[	[4.1m , 4.4m]	]4.71m , 4.76m[	[4.6m , 4.9m]
5	[4.76m , 4.86m[	[4.6m , 4.9m]	[5.16m , 5.36m[	[5.1m , 5.4m]	]5.66m , 5.71m[	[5.6m , 5.9m]

[1] For n = 0, y_n is always picked to be in unsuccessful zones to avoid relying on coincidental success.

Table 3.3: Event timeline analysis for f_{Trans} of 1050 Hz

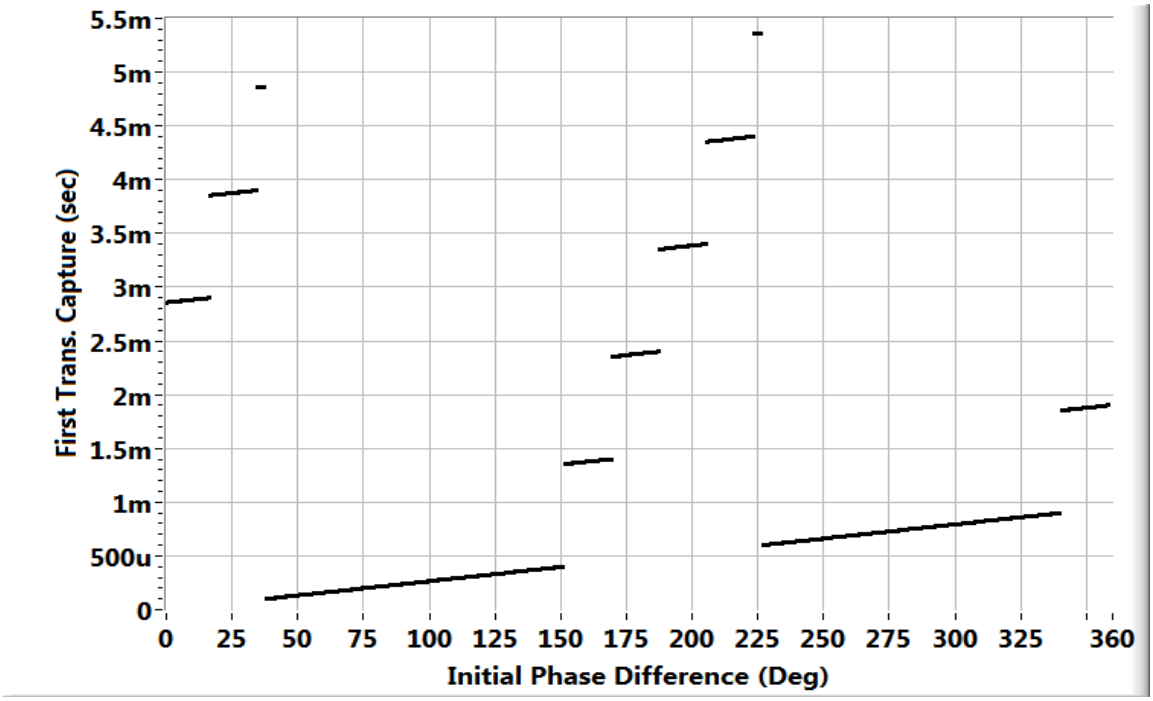

Fig. 3.36: First successful capture time vs. initial phase for 1900 Hz

3.4.3 COHERENT SINE SYNTHESIS

3.4.3.1 Determining the Transition Location

After having a captured frame whose waveform is known to contain a transition, and before a coherent sine wave can be synthesized based on the pre-transition portion of the waveform, the transition location within the captured frame needs to be determined. Since the waveform has already been captured, all processing presented after this point is done "off line" (i.e. not between acquisitions; with no further acquisitions pending the outcome of this processing), and is thus relatively relieved of timing constraints similar to those of the transition detection presented in Section 3.4.2.4. What is known is that the waveform contains an appropriate transition that consists of pre- and post-transition data of at least the desired length, for instance 20% of the entire waveform, but it is not known

where the transition location is between 20% and 80%. One algorithm to determine where the transition location is divides the whole waveform into many smaller concatenated waveforms, where each mini waveform is the length of a couple (say 1, 2, 3, or 4) of baseband single tone cycles (one can speak of a baseband single tone cycle, because the frequency of the baseband signal does not change, whether before or after the transition). The more cycles in a mini waveform the faster the location-pointing algorithm is, but the coarser the location pointed to. Then, starting from the whole waveform beginning and considering each of these mini waveforms with the one after it, sequentially (i.e. mini waveform 0 and mini waveform 1, then mini waveform 1 and mini waveform 2, then mini waveform 2 and mini waveform 3…etc), one can apply the single-tone detection algorithms presented in Section 3.3.2 to each of these mini waveforms and compute the ratios of the resulting amplitudes (i.e. amplitude extracted from mini waveform 1 divided by amplitude extracted from mini waveform 0, then amplitude extracted from mini waveform 2 divided by amplitude extracted from mini waveform 1, and so on) and inverting the ratio if it is less than 1. In all the waveforms except those near the transition location, these ratios are expected to yield approximately unity value. At the transition, the value is expected to be greater than one, as shown in Fig. 3.37. Similarly, the waveform shown in Fig. 3.21 can also be used for the purpose of pointing to the transition location using the algorithm presented above, as each point in the plot shown in Fig. 3.21 represents the RMS value of a "mini waveform". Thus, the ratio of consecutive points of the plot can be considered and processed as discussed above. However, Fig. 3.21 is generated for the purpose of quick transition detection, thus the mini waveform length (referred to as window size earlier) may be optimized for efficient transition detection and not for accurate transition locating. This algorithm locates the transition to within an acceptable resolution of a few cycles (down to 1 cycle) and

ultimately leads to splitting the waveform into three waveform types. Two of the waveforms are large or long, which are the pre- and post- transition waveforms, and one is a short waveform consisting primarily of the transition itself with a few cycles before and after it. Fig. 3.38 shows the entire captured frame containing pre- and post-transition sub-waveforms, while Fig. 3.39 shows the three waveforms as described above, where the ones on the edges are dense and long (in the 100's of µsec) while the one in the center, is short (4 µsec long) and contains the transition itself.

In this example, where the entire waveform is 0.5 msec, the transition occurred at ~ 50% of the waveform length or ~ 250 µsec. Having the pre-transition waveform isolated, one can apply the single tone detection algorithm covered in Section 3.3.2 on the whole pre-transition waveform, thus resulting in a detected frequency, amplitude, and phase value for the pre-transition waveform. The to-be-synthesized waveform should be designed to have the frequency and phase (and amplitude, although it is inconsequential

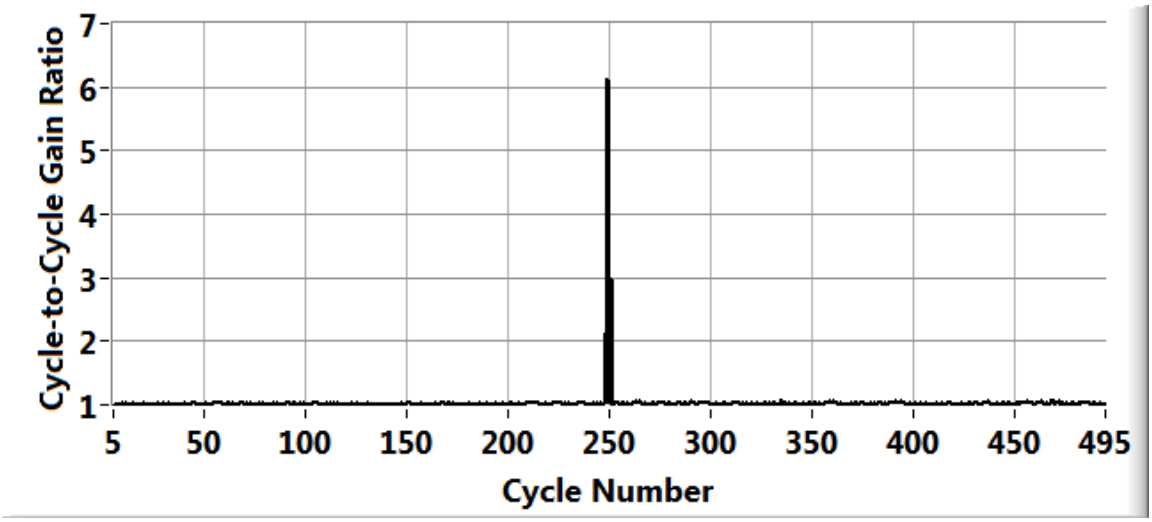

Fig. 3.37: Cycle-to-cycle ratio vs. cycle number pointing to transition location

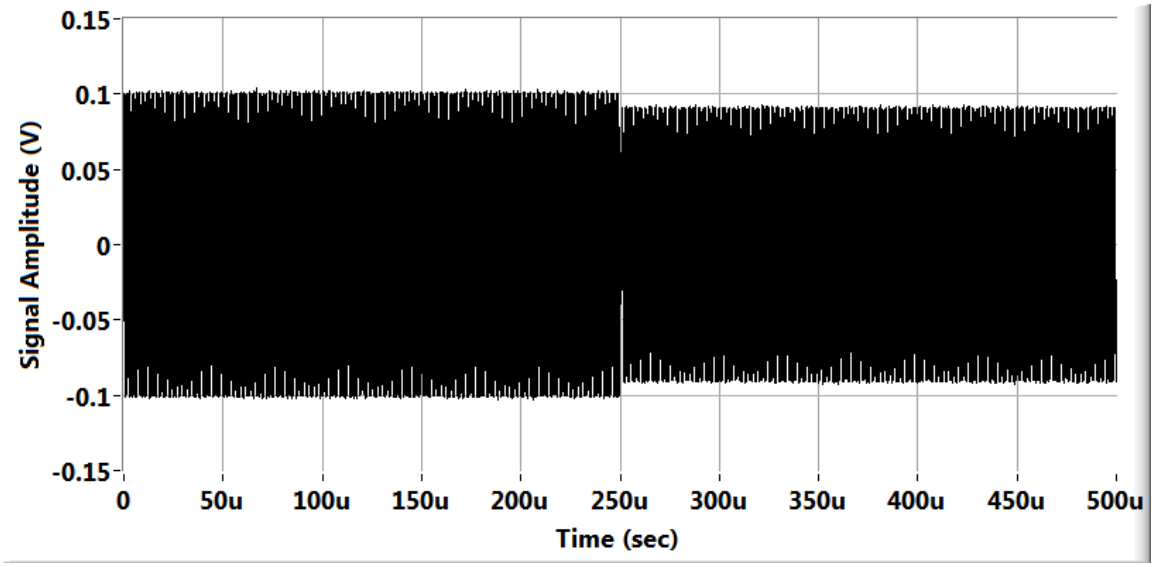

Fig. 3.38: Captured frame containing entire waveform with pre- and post-transition sub-waveforms (for -1 dB transition)

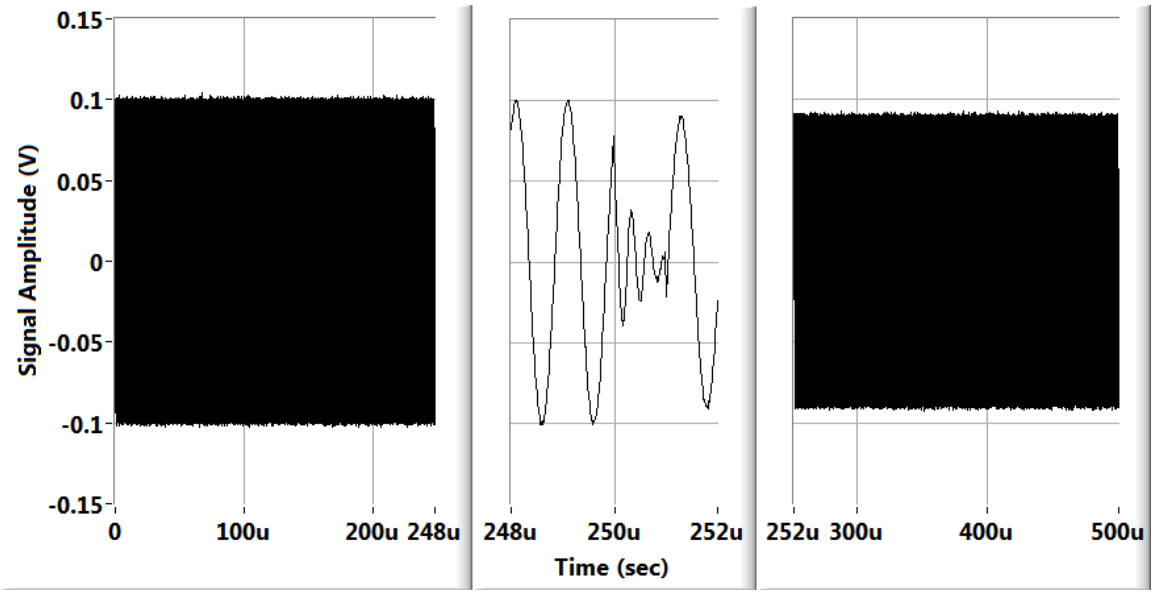

Fig. 3.39: Splitting the waveform into 3 types

except for visual presentation reasons) of the pre-transition waveform, but it is to span the length of the whole capture frame and not just the pre-transition waveform. It is, essentially, a longer version of the pre-transition waveform.

3.4.3.2 Synthesizing Frame-Long Pre-Transition Waveform

Knowing the length of the whole capture frame, either directly in terms of number of samples or indirectly in terms of covered time period and given a sampling rate, one can ultimately know what the total number of points, N, that needs to be synthesized is. And, knowing what the synthesized sine waveform frequency, amplitude, and phase need to be, a loop can be built to generate the waveform points and build them into an array, one point at a time, where the loop index, starts from zero and increases in steps of 1 until it reaches $(N-1)$, and where the output values, Y_{synth}, are expressed as shown in (3.30).

$$Y_{synth} = A_{PT} \sin\left(\frac{2\pi i F_{PT}}{F_{samp}} + \varphi_{PT}\right) \tag{3.30}$$

where, A_{PT}, F_{PT}, and φ_{PT} are the pre-transition waveform extracted amplitude, frequency, and phase, respectively, where i is the loop index, and where F_{samp} is the sampling rate for the captured frame, whose pre-transition portion is being emulated. Showing the original captured frame, which is the one shown in Fig. 3.38, on the same graph as the synthesized waveform Y_{synth}, results in the graph shown in Fig. 3.40.

Notice that while the actual captured frame (black) shows a drop in the peak-to-peak signal level after the transition, the synthesized waveform (red) continues at almost the same level as the pre-transition waveform, albeit for differences due to noise, because the synthesized waveform is mathematical and noise-free. Zooming into the graph shown in Fig. 3.40 and specifically into the neighborhood of the transition, results in the graph

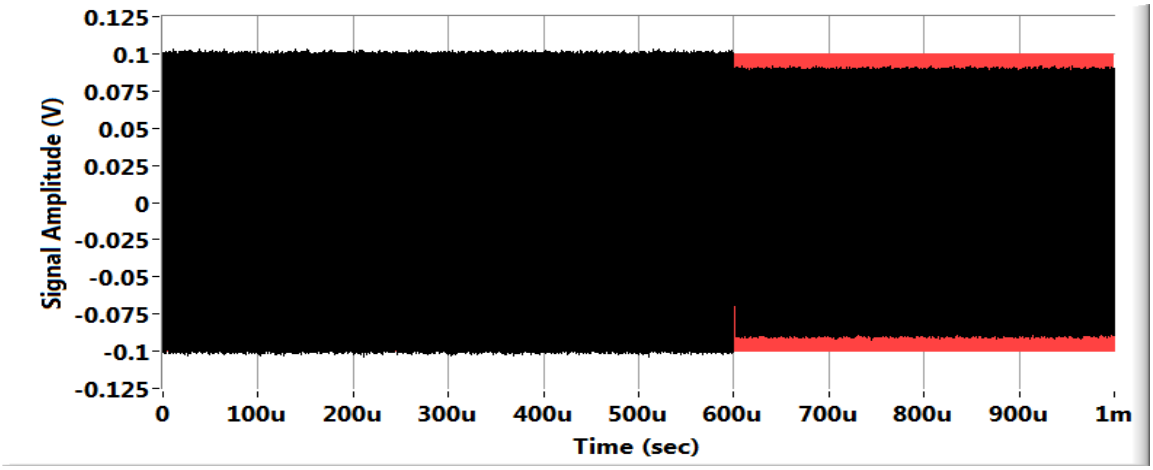

Fig. 3.40: Captured frame with frame-long synthesized pre-trans. waveform

shown in Fig. 3.41. As one can see from Fig. 3.41, the synthesized waveform (red) overlaps and gets hidden under the actual captured frame before the transition, and only appears after the transition, visually presenting itself as a continuation of the pre-transition signal into the post-transition realm and readying the system for the next step of computing the phase shift that the signal undergoes during transition.

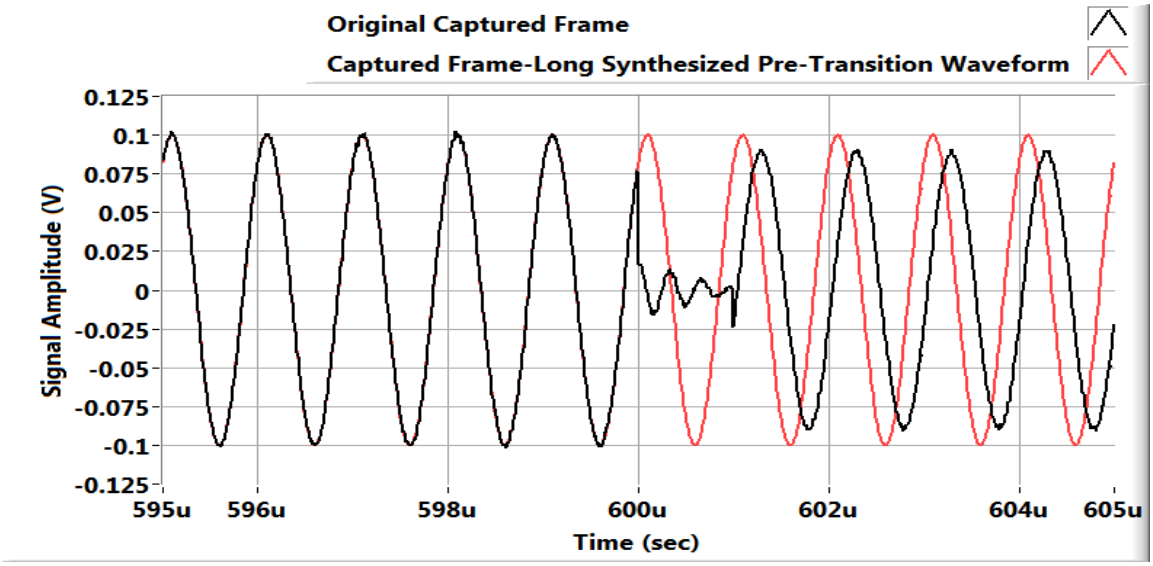

Fig. 3.41: Captured frame with frame-long synthesized pre-trans. Waveform (zoomed in)

3.4.4 PHASE-SHIFT COMPUTATION

3.4.4.1 Two Approaches to Phase-Shift Computation

After having detected a transition and captured a frame containing such a transition, and after pinpointing the location of the transition within the frame and synthesizing a coherent sine wave that is frame-long and based solely on the pre-transition portion of the waveform, the last step of the transient phase shift capture scheme is to consider the post-transition portion of the captured frame, the right-most shown in Fig. 3.39, with an equally-sized portion of the waveform synthesized in Section 3.4.3.2 taken from the waveform's end. Thus, given the size of the post-transition waveform, say containing N_{PT} samples, one can take the last N_{PT} samples of the synthesized waveform as well, and then yield two waveforms that are equal in size, nominally having the same frequency, but one having the phase and amplitude representative of the signal before the transition and one having the phase and amplitude representative of the signal after the transition. The first approach to computing the phase-shift between the two waveforms is FFT-based, whereas the second approach is time domain-based. The next two sections cover both approaches in detail.

3.4.4.2 FFT-Based Phase Shift Computation

Given what has been accomplished thus far, that is having two waveforms of equal length whose frequencies are nominally equal, but whose amplitudes and phases are different and representative of pre- and post-transition portions of the captured frame, it makes most sense to utilize the FFT-based single tone extraction method presented in Section 3.3.2 to extract the single tone information of each waveform. Having the extracted phase information of both waveforms, one can simply take the difference of the two phases and arrive at the phase-shift that the signal undergoes during transition. It

makes sense to utilize this method because it requires no special processing of the waveforms obtained thus far. This is true because coherent synthesis had already taken place, before arriving at the two waveforms herein, where one is a continuation of the pre-transition waveform and the other is the post-transition waveform itself, and most importantly with both considered under the same time period, as if both are captured in one snapshot. While this is the method used throughout the work of this dissertation, another method is discussed next, which utilizes time domain-based signal processing instead of the FFT-based processing done within the single-tone extraction algorithm.

3.4.4.3 Time Domain-Based Phase-Shift Computation

Starting from the fundamentals of this method, consider the expressions of two sine waveforms, which have the same frequency, but different amplitudes and phases: $f_1(t) = A_1 \sin(2\pi ft + \varphi_1)$ and $f_2(t) = A_2 \sin(2\pi ft + \varphi_2)$. Starting from (2.19), one can rewrite the waveform multiplication to become what is shown in (3.31).

$$f_1(t)f_2(t) = A_1A_2 \frac{\cos(\varphi_1 - \varphi_2) - \cos(4\pi ft + \varphi_1 + \varphi_2)}{2} \tag{3.31}$$

Thus, if the two waveforms are multiplied, then the resulting waveform would contain a DC component (non-time dependent) that is proportional to the phase difference of the waveform, in addition to a time dependent component, which is a also a single tone, but of twice the frequency as the original waveforms. If the resulting waveform is integrated over a whole number of cycles of the latter single tone, then the result would be solely dependent on the phase difference between the original waveforms as well as their amplitudes, as the single-tone integration over a whole number of its cycles yields zero. As far as the algorithm implementation is concerned, this means that subsets of the two waveforms (arrays) are taken starting from either side of the arrays, as long as the same

number of samples is considered in both waveforms and as long as that number corresponds to a whole number of half-cycles of the original waveform frequency. Treating the resulting waveform subsets as the new two waveforms, the waveforms then get multiplied with each other, point by point, then multiplied by 2, and then finally all the points of the resulting multiplication are averaged into a single value, which corresponds to $A_1A_2\cos(\varphi_1-\varphi_2)$. The mathematical representation of the algorithm described above is expressed below, starting from (3.32), as derived from (3.31).

$$A_1A_2\cos(\varphi_1-\varphi_2)=2f_1(t)f_2(t)+A_1A_2\cos(4\pi ft+\varphi_1+\varphi_2) \tag{3.32}$$

Integrating both sides of (3.32) from 0 to $\frac{k}{2f}$ and then dividing by $\frac{k}{2f}$, where k is a constant, means taking the average of the expression over a whole number of cycles of the single-tone whose frequency is $2f$. The derivation follows.

$$\begin{aligned}\frac{2f}{k}\int_0^{\frac{k}{2f}} A_1A_2\cos(\varphi_1-\varphi_2)\,dt \\ =\frac{2f}{k}\int_0^{\frac{k}{2f}} 2f_1(t)f_2(t)dt \\ +\frac{2f}{k}\int_0^{\frac{k}{2f}} A_1A_2\cos(4\pi ft+\varphi_1+\varphi_2)\,dt\end{aligned} \tag{3.33}$$

But,

$$\int_0^{\frac{k}{2f}}\cos(4\pi ft+\varphi_1+\varphi_2)\,dt=\frac{\sin(4\pi ft+\varphi_1+\varphi_2)}{4\pi f}\Bigg|_0^{\frac{k}{2f}} \tag{3.34}$$

And,

$$\begin{aligned}\frac{\sin(4\pi ft+\varphi_1+\varphi_2)}{4\pi f}\Bigg|_0^{\frac{k}{2f}} \\ =\frac{1}{4\pi f}[\sin(2\pi k+\varphi_1+\varphi_2)-\sin(\varphi_1+\varphi_2)]\xrightarrow{yields}0\end{aligned} \tag{3.35}$$

From (3.34) and (3.35), it is concluded that the last term of (3.33) is zero, and thus (3.33) can be rewritten as follows.

$$\frac{2f}{k}\int_0^{\frac{k}{2f}} 2f_1(t)f_2(t)dt = \frac{2f}{k}A_1A_2\cos(\varphi_1-\varphi_2)\,t\Big|_0^{\frac{k}{2f}} = A_1A_2\cos(\varphi_1-\varphi_2) \tag{3.36}$$

The result shown in (3.36) summarizes the time domain-based phase-shift computation algorithm, where the two waveforms, $f_1(t)$ and $f_2(t)$, are multiplied by each other and by 2, point-by-point, and then the resulting waveform is averaged over a whole number of half-cycles, to yield a single value constant that is proportional to the phase shift between the waveforms and the waveform amplitudes. To finally compute the phase-shift, the waveform amplitudes are needed. To call for the single tone extraction algorithm at this point, to get a measure of the waveform amplitudes, defies the purpose of the time-domain approach; and it is also meaningless because the single tone extraction algorithm could have been used earlier to extract the phase information to begin with, as described in 3.4.4.2. Consequently, the waveform amplitudes are to be computed in a time-domain approach. Because it is known that each of these waveforms are single tones, one can compute the RMS (Root-Mean-Square) value of each of these waveforms and then multiply the results by $\sqrt{2}$ to arrive at the peak amplitude of the waveforms, A_1 and A_2, as can be seen, going from (3.36) to (3.37) below.

$$\cos(\varphi_1-\varphi_2) = \frac{\frac{2f}{k}\int_0^{\frac{k}{2f}} 2f_1(t)f_2(t)dt}{2\sqrt{\frac{2f}{k}\int_0^{\frac{k}{2f}}[f_1(t)]^2dt}\sqrt{\frac{2f}{k}\int_0^{\frac{k}{2f}}[f_2(t)]^2dt}} \tag{3.37}$$

The RMS of each waveform can be computed, as shown in the denominator on the right side of (3.37), by simply considering the value of each of the points of the waveforms,

squaring the values, averaging them into a single value, and then taking the square-root of the result. Finally, the mathematical expression for the phase-shift can be written as follows, where the numerator is the whole-cycle average of $2f_1(t)f_2(t)$ and the denominator is twice the multiplication of the square roots of the whole-cycle averages of ${f_1}^2(t)$ and ${f_2}^2(t)$.

4 CORE OF THE TEST METHODOLOGY

4.1 Extracting RF Performance Parameters

4.1.1 INTRODUCTION

The accurate computation and extraction of the RF performance parameters, from the basic measurements done at baseband in response to the designed and characterized MTSG signal, remains at the heart of this problem as the challenging and compelling portion of this proposed test methodology and is described below.

4.1.2 SYSTEM ANALYSIS

Let X be the MTSG input to the DUT, which is the summation of many sinusoids and described in (4.1) below,

$$X = \sum_{i=1}^{N} A_i \sin(2\pi i f_{clk} t + \varphi_i) \tag{4.1}$$

where A_i is the amplitude of the sinusoid, φ_i is the phase of the sinusoid, i is the index corresponding to the harmonic number of the sinusoid, and N is the index of the last considered (or last significant) harmonic of f_{clk}. Correctly choosing N is important and will be studied in Sections 4.2.3 and 4.3.4, within the simulation and experimental results sections, respectively.

Let Y be the DUT baseband output, including linear and non-linear gain components as shown in (4.2), with the frequency translation being understood. In (4.2), α_0 represents non-input related output signals (e.g. DC offset, noise, residual spurs…etc), α_1 represents small-signal linear gain, and α_2 and α_3 are the non-linear gain components. Higher order terms are negligible in most practical RF systems, and are not considered in

this analysis. The same equation is expressed in (2.6), but repeated here for ease of reference.

$$Y = \alpha_0 + \alpha_1 X + \alpha_2 X^2 + \alpha_3 X^3 \tag{4.2}$$

The receiver (conversion) gain at the set LO frequency can be computed from α_1 as follows in (4.3), which was also derived earlier in (2.13).

$$Gain\ (dB) = 20Log_{10}(|\alpha_1|) \tag{4.3}$$

The input third order intercept point (IIP3) at the set LO frequency can be computed from α_1 and α_3 as follows in (4.4), [45], and as can also be achieved from (2.29) with the replacement of Z_0 with 50Ω.

$$IIP3\ (dBm) = 10\log_{10}\left(10\left|\frac{4\alpha_1}{3\alpha_3}\right|\right) \tag{4.4}$$

For small X, the primary and most significant component of Y is Y_{ST}, which is the baseband single tone corresponding to down-converted H_j, as described in Section 2.2.3, and whose frequency is $|LO - jf_{clk}|$. The down-conversion of H_j is demonstrated in Fig. 2.3. Expressing Y_{ST} in a similar manner to Y in (4.2) requires the substitution of (4.1) in (4.2) and performing the necessary calculations and trigonometric operations to find the resulting components of $\alpha_1 X$, $\alpha_2 X^2$, and $\alpha_3 X^3$ that appear at Y_{ST}'s baseband frequency of $|LO - jf_{clk}|$. While finding the analytical expression of Y_{ST} in terms of the components generated from a general multitone signal going through a non-linear device is instrumental in determining the parameters α_1, α_2, and α_3 and consequently in computing the Gain and IIP3 of the receiver, it is quite involved due to the large number of combinations among the general set of N MTSG tones that can result in down-converted components at Y_{ST}'s frequency. This occurrence of a large number of components at the same frequency is primarily due to the equal tone spacing inherent to

the proposed MTSG signal, which complicates the analysis, as described in [44]. First, Y_{ST} is expressed as

$$Y_{ST} = \alpha_1(X)_{ST} + \alpha_2(X^2)_{ST} + \alpha_3(X^3)_{ST} \tag{4.5}$$

where $(X)_{ST}$, $(X^2)_{ST}$, and $(X^3)_{ST}$ are the components of X, X^2, and X^3 respectively that line up with H_j and consequently get down-converted to Y_{ST} at a frequency of $|LO - jf_{clk}|$. $(X)_{ST}$, $(X^2)_{ST}$, and $(X^3)_{ST}$ are analyzed next, in Section 4.1.3, where closed-form expression are presented for each.

4.1.3 EXPRESSING MTSG MATRIX COEFFICIENTS

$(X)_{ST}$ is the input component that gets down-converted through linear conversion gain α_1 to Y_{ST} , and thus is simply H_j (the j[th] sinusoid), and it is expressed as follows.

$$(X)_{ST} = A_j \sin\left(2\pi j f_{clk} t + \varphi_j\right) \tag{4.6}$$

$(X^2)_{ST}$ and $(X^3)_{ST}$ are more complicated and analytically intensive, and thus only some representative steps are shown in this section before the final closed forms are presented. Detailed derivations of $(X^2)_{ST}$ and $(X^3)_{ST}$ are presented separately in Sections 4.1.6 and 4.1.6.2, respectively. Also, since all the components of $(X)_{ST}$, $(X^2)_{ST}$, and $(X^3)_{ST}$ are either sines or cosines of $2\pi j f_{clk} t$ with some amplitude and phase, they will all be converted to sines and use the following convention.

$$A \sin(2\pi j f_{clk} t + \varphi) \stackrel{\text{def}}{=} (A\,, \varphi) \tag{4.7}$$

Re-expressing $(X)_{ST}$ in (4.6) in accordance with (4.7) yields

$$(X)_{ST} = (A_j\,, \varphi_j) \tag{4.8}$$

The analysis towards finding $(X^2)_{ST}$ and $(X^3)_{ST}$ assumes that α_2 and α_3 are frequency independent within the receiver bandwidth. For narrowband RF receivers, or broadband RF receivers whose response rolls off within the band of operation, one may consider

mathematically shaping the MTSG response to improve the method's accuracy. This shaping technique applies different attenuation coefficients to the different MTSG tones before using them in computing the matrix coefficients $(X)_{ST}$, $(X^2)_{ST}$, and $(X^3)_{ST}$. The response of the attenuation coefficients versus frequency approximates the inverse of a nominal receiver response. Section 4.2.4 discusses the shaping technique in detail and demonstrates and quantifies the improvement it brings to the proposed methodology.

We start with the calculation of $(X^2)_{ST}$.

$$X^2 = \left[\sum_{i=1}^{N} A_i \sin(2\pi i f_{clk} t + \varphi_i)\right]^2 \tag{4.9}$$

Expanding the expression above results in many components that fall in two forms and they are gathered and expressed in the following two summations $\sum_{i=1}^{N} A_i^2 \sin^2(2\pi i f_{clk} t + \varphi_i)$ and $\sum_{i=1}^{N-1} \sum_{k=i+1}^{N} 2A_i A_k \sin(2\pi i f_{clk} t + \varphi_i) \sin(2\pi k f_{clk} t + \varphi_k)$, but

$$\sin^2(a) = \frac{1 - \cos(2a)}{2} \tag{4.10}$$

and

$$\sin(a)\sin(b) = \frac{\cos(a-b) - \cos(a+b)}{2} \tag{4.11}$$

Expanding (4.9) and then substituting the resulting components in accordance to (4.10) and (4.11), and then considering only the resulting cosine terms whose frequency is jf_{clk} in order to extract $(X^2)_{ST}$ from the general X^2 expression, and finally converting the cosines to sines, we arrive at the closed form expression for $(X^2)_{ST}$ that is shown in (4.12), where the first non-summation term of index $j/2$ exists only for even j.

$$(X^2)_{ST} = \left(-\frac{1}{2}A_{\frac{j}{2}}^2, 2\varphi_{\frac{j}{2}} + \frac{\pi}{2}\right) + \sum_{i=1}^{N-j}\left(A_iA_{j+i}, \varphi_{j+i} - \varphi_i + \frac{\pi}{2}\right) - \sum_{i=1}^{\left\lfloor\frac{j-2}{2}\right\rfloor}\left(A_iA_{j-i}, \varphi_{j-i} + \varphi_i + \frac{\pi}{2}\right) \tag{4.12}$$

A similar procedure for $(X^3)_{ST}$ starts with expressing X^3 as

$$X^3 = \left[\sum_{i=1}^{N} A_i \sin(2\pi i f_{clk} t + \varphi_i)\right]^3 \tag{4.13}$$

Expanding the expression above results in more components than in (4.9) that fall in three forms and they are gathered and expressed in the summations $\sum_{i=1}^{N} A_i^3 \sin^3(2\pi i f_{clk} t + \varphi_i)$, $\sum_{i=1}^{N}\sum_{k=1,k\neq i}^{N} 3A_i^2 A_k \sin^2(2\pi i f_{clk} t + \varphi_i)\sin(2\pi k f_{clk} t + \varphi_k)$, and $\sum_{i=1}^{N-2}\sum_{k=i+1}^{N-1}\sum_{m=k+1}^{N} 6A_iA_kA_m \sin(2\pi i f_{clk} t + \varphi_i)\sin(2\pi k f_{clk} t + \varphi_k)\sin(2\pi m f_{clk} t + \varphi_m)$, but

$$\sin^3(a) = \frac{3\sin(a) - \sin(3a)}{4} \tag{4.14}$$

and

$$\sin^2(a)\sin(b) = \frac{\sin(b)}{2} + \frac{\sin(2a-b) - \sin(2a+b)}{4} \tag{4.15}$$

and

$$\sin(a)\sin(b)\sin(c) = \frac{1}{4}[\sin(a-b+c) + \sin(a+b-c) + \sin(-a+b+c) - \sin(a+b+c)] \tag{4.16}$$

Expanding (4.13) and then substituting the resulting components in accordance to (4.14), (4.15), and (4.16), and then considering only the resulting sine terms whose frequency is jf_{clk} in order to extract $(X^3)_{ST}$ from the general X^3 expression, we arrive at the closed

form expression for $(X^3)_{ST}$ as shown in (4.18), where δ_x has a value 0 for even x and 1 for odd x, as defined in (4.17).

$$\delta_{\mathrm{x}} \stackrel{\text{def}}{=} \left\lceil \frac{x}{2} \right\rceil - \left\lfloor \frac{x}{2} \right\rfloor \tag{4.17}$$

$$\begin{aligned}
&(X^3)_{ST} \\
&= \left(\frac{3}{4}A_j^3\,,\varphi_j\right) - \left(\frac{1}{4}A_{\frac{j}{3}}^3\,,3\varphi_{\frac{j}{3}}\right) + \sum_{i=1,i\neq j}^{N}\left(\frac{3}{2}A_jA_i^2\,,\varphi_j\right) \\
&+ \sum_{i=1,i\neq\left\lfloor\frac{j}{2}\right\rfloor}^{\left\lfloor\frac{N+j}{2}\right\rfloor-\left\lfloor\frac{j}{2}\right\rfloor}\left(\frac{3}{4}A_{i+\left\lfloor\frac{j}{2}\right\rfloor}^2A_{2i-\delta_{\mathrm{j}}}\,,2\varphi_{i+\left\lfloor\frac{j}{2}\right\rfloor}-\varphi_{2i-\delta_{\mathrm{j}}}\right) \\
&- \sum_{i=1}^{\left\lfloor\frac{N-j}{2}\right\rfloor}\left(\frac{3}{4}A_i^2A_{j+2i},2\varphi_i-\varphi_{j+2i}\right) - \sum_{i=1,i\neq\frac{j}{3}}^{\left\lfloor\frac{j-1}{2}\right\rfloor}\left(\frac{3}{4}A_i^2A_{j-2i}\,,2\varphi_i+\varphi_{j-2i}\right) \\
&+ \sum_{k=1}^{j-3}\sum_{i=1}^{\left\lceil\frac{j-k-2}{2}\right\rceil}\left(\frac{3}{2}A_kA_{i+k}A_{j-i}\,,-\varphi_k+\varphi_{i+k}+\varphi_{j-i}\right) \\
&+ \sum_{k=1}^{j-1}\sum_{i=1}^{N-j}\left(\frac{3}{2}A_kA_{i+k}A_{j+i}\,,\varphi_k-\varphi_{i+k}+\varphi_{j+i}\right) \\
&+ \sum_{k=j+1}^{\left\lceil\frac{N+j-1}{2}\right\rceil}\sum_{i=1}^{N+j-2k}\left(\frac{3}{2}A_kA_{i+k}A_{2k+i-j}\,,\varphi_k+\varphi_{i+k}-\varphi_{2k+i-j}\right) \\
&- \sum_{k=1}^{\left\lfloor\frac{j-3}{3}\right\rfloor}\sum_{i=1}^{\left\lceil\frac{j-3k-2}{2}\right\rceil}\left(\frac{3}{2}A_kA_{i+k}A_{j-(i+2k)}\,,\varphi_k+\varphi_{i+k}+\varphi_{j-(i+2k)}\right)
\end{aligned} \tag{4.18}$$

Treating the components of $(X^2)_{ST}$ and $(X^3)_{ST}$ as phasors or complex values and adding them up yields a single phasor value for each of $(X^2)_{ST}$ and $(X^3)_{ST}$, understood as a sine of $2\pi jf_{clk}t$, as in the case of $(X)_{ST}$.

4.1.4 MATRIX EQUATION BUILDING OPTIONS

4.1.4.1 Targeting Complex-Valued Least-Square Regression

Having multiple attenuation levels available at the output of the MTSG, with each corresponding to certain known $(X)_{ST}$, $(X^2)_{ST}$, and $(X^3)_{ST}$ and corresponding to a certain measured Y_{ST}, a least-squares fit of α_1, α_2, and α_3 is possible, as shall be shown in this section. Whereas in [46], the magnitude of both sides of (4.5) is taken to enable the use of real-valued least-square (LS) regression, as shown in detail in the following section, direct complex regression is possible where the baseband tone Y_{ST} is measured as a phasor, as in the final phase-aware form of the methodology presented in this dissertation. Stacking (4.5), as is, for each of the m MTSG levels yields the matrix shown in (4.19). A complex-valued LS regression is then performed to yield α_1, α_2, and α_3. With α_1 and α_3 known, gain and IIP3 can be computed from (4.3) and (4.4), and NF can be found as discussed in Section 2.3.1.2.

In (4.19) below, the number subscript stands for the MTSG level, at which Y_{ST} is measured and, for which $(X)_{ST}$, $(X^2)_{ST}$ and $(X^3)_{ST}$ are computed for a given LO frequency.

$$\begin{bmatrix} Y_{ST\,0} \\ Y_{ST\,1} \\ \vdots \\ Y_{ST\,m} \end{bmatrix} = \begin{bmatrix} (X)_{ST\,0} & (X^2)_{ST\,0} & (X^3)_{ST\,0} \\ (X)_{ST\,1} & (X^2)_{ST\,1} & (X^3)_{ST\,1} \\ \vdots & \vdots & \vdots \\ (X)_{ST\,m} & (X^2)_{ST\,m} & (X^3)_{ST\,m} \end{bmatrix} \begin{bmatrix} \alpha_1 \\ \alpha_2 \\ \alpha_3 \end{bmatrix} \tag{4.19}$$

Alternatively, and as an improvement to the method, one may find α_1 separately, from one of the lowest rows of (4.19) where $(X^2)_{ST}$ and $(X^3)_{ST}$ are negligible due to the low MTSG levels, as $Y_{ST}/(X)_{ST}$, and then (4.19) can be expressed as follows, where $\alpha_1(X)_{ST\,m}$ column joins $Y_{ST\,m}$ column as a known vector.

$$\begin{bmatrix} Y_{ST_0} - \alpha_1(X)_{ST_0} \\ Y_{ST_1} - \alpha_1(X)_{ST_1} \\ \vdots \\ Y_{ST_m} - \alpha_1(X)_{ST_m} \end{bmatrix} = \begin{bmatrix} (X^2)_{ST_0} & (X^3)_{ST_0} \\ (X^2)_{ST_1} & (X^3)_{ST_1} \\ \vdots & \vdots \\ (X^2)_{ST_m} & (X^3)_{ST_m} \end{bmatrix} \begin{bmatrix} \alpha_2 \\ \alpha_3 \end{bmatrix} \tag{4.20}$$

Part of optimizing this measurement system for a given DUT type is to carefully choose the range of possible attenuations. Firstly, given the MTSG signal, the highest attenuation setting, m, should invoke high enough attenuation, such that the non-linearity components at Y_{ST} are minimal. This can be checked by verifying that the measured gain, α_1, from the lower rows of (4.19) as discussed above, matches well with that of single-tone standard measurement method. Secondly, The lowest attenuation setting, 0, should be chosen such that no MTSG level would trigger baseband saturation or clipping, which in turn involves a "hard non-linearity", which would dominate the third order non-linearity we are trying to measure. Additionally, the lowest attenuation setting can be optimally chosen for a nominal DUT during test design stage to minimize the extracted measurements errors.

4.1.4.2 Targeting Real-Valued Least-Square Regression

This section covers the initial procedure used in [46], where the magnitude of both sides of (4.5) is taken to enable the use of real-valued least-square (LS) regression, because only $|Y_{ST}|$ was measured. The method has been improved since to include phase measurements of Y_{ST}, and consequently requires complex least-square regression, as shown in the previous section and as discussed in [47]. The real-valued regression scheme, however, is presented herein for reference. Taking the magnitude of both sides of (4.5) results in nine real terms on the right side, as shown in (4.21).

$$\begin{aligned} |Y_{ST}| = {} & |\alpha_1||(X)_{ST}| + |\alpha_2||(X^2)_{ST}| + |\alpha_3||(X^3)_{ST}| \\ & +2\left(\alpha_{1_r}\alpha_{2_r} + \alpha_{1_i}\alpha_{2_i}\right)\left((X)_{ST_r}(X^2)_{ST_r} + (X)_{ST_i}(X^2)_{ST_i}\right) \\ & +2\left(\alpha_{1_r}\alpha_{3_r} + \alpha_{1_i}\alpha_{3_i}\right)\left((X)_{ST_r}(X^3)_{ST_r} + (X)_{ST_i}(X^3)_{ST_i}\right) \end{aligned} \tag{4.21}$$

$$+2\left(\alpha_{2_r}\alpha_{3_r}+\alpha_{2_i}\alpha_{3_i}\right)\left((X^2)_{ST_r}(X^3)_{ST_r}+(X^2)_{ST_i}(X^3)_{ST_i}\right)$$
$$+2\left(\alpha_{1_r}\alpha_{2_i}-\alpha_{1_i}\alpha_{2_r}\right)\left((X)_{ST_i}(X^2)_{ST_r}-(X)_{ST_r}(X^2)_{ST_i}\right)$$
$$+2\left(\alpha_{1_r}\alpha_{3_i}-\alpha_{1_i}\alpha_{3_r}\right)\left((X)_{ST_i}(X^3)_{ST_r}-(X)_{ST_r}(X^3)_{ST_i}\right)$$
$$+2\left(\alpha_{2_r}\alpha_{3_i}-\alpha_{2_i}\alpha_{3_r}\right)\left((X^2)_{ST_i}(X^3)_{ST_r}-(X^2)_{ST_r}(X^3)_{ST_i}\right)$$

where the subscripts r and i indicate the real and imaginary components of the subscripted parameters. While only the main $|\alpha_1|$, $|\alpha_2|$, and $|\alpha_3|$ are needed, the real-valued least-square regression on the matrix equation built from stacking (4.21) for various attenuation levels results in also solving for other "unknowns". The main rectangular matrix is clearly more complicated, contains nine unknowns, and can possibly run into singularity issues if some of its columns have inter-dependencies.

4.1.5 SOLVING THE LINEAR MATRIX EQUATION

Solving for (4.19), (4.20), or the stacked matrix equation, whose rows correspond to (4.21) for various MTSG attenuation settings, is essentially solving a linear system of equations, as shown in (4.22), where $Y_{m\times 1}$ represents the known vector of m elements, $A_{m\times n}$ the input m-by-n matrix, and $X_{n\times 1}$ the set of n elements in the solution vector.

$$Y_{m\times 1} = A_{m\times n}\, X_{n\times 1} \tag{4.22}$$

Since there are more attenuation levels (up to 63, per the hardware scheme discussed in Section 3.2.1) than there are unknowns (2 or 3, depending on whether (4.19) or (4.20) is used), then $m > n$, and consequently the system has more equations than unknowns, and it is called over-determined. Generally, the solution that satisfied $AX = Y$ may not exist, which is why a least-square regression is done to find the solution that minimizes $\|AX - Y\|$. Linear equation solvers, whether real- or complex-valued, exist in various software packages, such as the one included in LabVIEW™, which is also used in the experimental work of this dissertation, [48].

4.1.6 FULL DERIVATION OF MATRIX COEFFICIENTS

In this section, we provide details on the analysis leading to (4.12) and (4.18), starting with (4.12), discussed in Section 4.1.6.1 and followed by (4.18), discussed in Section 4.1.6.2.

4.1.6.1 Full Derivation of $(X^2)_{ST}$

We start by expanding on the transition from (4.9) to (4.12) using (4.10) and (4.11). The $[\sum_{i=1}^{N} A_i \sin(2\pi i f_{clk} t + \varphi_i)]^2$ term in (4.9) expands into two types of terms, a $\sin^2(\,)$ and a $\sin(\,)\sin(\,)$ terms, as shown in (4.23).

$$\left[\sum_{i=1}^{N} A_i \sin(2\pi i f_{clk} t + \varphi_i)\right]^2 = \sum_{i=1}^{N} {A_i}^2 \sin^2(2\pi i f_{clk} t + \varphi_i) + \sum_{k=1}^{N-1} \sum_{i=k+1}^{N} 2A_k A_i \sin(2\pi k f_{clk} t + \varphi_k) \sin(2\pi i f_{clk} t + \varphi_i) \tag{4.23}$$

The $\sin^2(\,)$ term in (4.23) yields, according to (4.10), a DC component as well as a $\sin(\,)$ component whose frequency is double what is in the $\sin^2(\,)$ term. Thus, for the $\sin^2(\,)$ term to yield a component that lands at H_j, it will need to be resulting from a term whose frequency is exactly half that of H_j, when j is even. Consequently, the first non-summation term of (4.12) comes from,

$${A_{\frac{j}{2}}}^2 \sin^2\left(2\pi \frac{j}{2} f_{clk} t + \varphi_{\frac{j}{2}}\right) = -\frac{1}{2} {A_{\frac{j}{2}}}^2 \cos\left(2\pi j f_{clk} t + 2\varphi_{\frac{j}{2}}\right) \tag{4.24}$$

where $-\frac{1}{2}{A_{\frac{j}{2}}}^2 \cos\left(2\pi j f_{clk} t + 2\varphi_{\frac{j}{2}}\right)$ is expressed as $\left(-\frac{1}{2}A_{\frac{j}{2}}^2, 2\varphi_{\frac{j}{2}} + \frac{\pi}{2}\right)$ per the definition in (4.7), and where the $\frac{\pi}{2}$ reflects the conversion from a cosine to a sine, per (4.29).

The $\sin(\,)\sin(\,)$ term in (4.23) yields according to (4.11) the cosines of the difference and sum, as shown below.

$$\sum_{k=1}^{N-1}\sum_{i=k+1}^{N} 2A_kA_i \sin(2\pi k f_{clk}t + \varphi_k)\sin(2\pi i f_{clk}t + \varphi_i)$$
$$= \sum_{k=1}^{N-1}\sum_{i=k+1}^{N} A_kA_i\{\cos[2\pi(k-i)f_{clk}t + \varphi_k - \varphi_i] - \cos[2\pi(k+i)f_{clk}t + \varphi_k + \varphi_i]\} \quad (4.25)$$

Treating the two cosine terms separately, and considering only the terms where $|k-i| = j$ and $|k+i| = j$, respectively, we present the following analysis to arrive at the $\sin(\,)\sin(\,)$ terms of (4.25) that show up at H_j. Note that the acceptable sign of the absolute value operand is based on i being greater than k, since the summation of i starts with $k+1$. We start by the first cosine term below.

$$\left\{\sum_{k=1}^{N-1}\sum_{i=k+1}^{N} A_kA_i \cos[2\pi(k-i)f_{clk}t + \varphi_k - \varphi_i]\right\}_{@\,H_j,\ where\ |k-i|=j \xrightarrow{yields} i=k+j}$$
$$= \sum_{k=1}^{N-1} A_kA_{k+j}\cos\left[-2\pi j f_{clk}t + \varphi_k - \varphi_{k+j}\right] \quad (4.26)$$

However, to maintain the highest considered harmonic at N we change the $N-1$ limit of the summation constant k to $N-j$, so that the highest tone in (4.26), A_{k+j}, is A_N when $k = N-j$. Moreover, we replace the summation index k with i, and we invert the sign of the cosine operand, per (4.27), to yield the result shown in (4.28).

$$\cos(-\alpha) = \cos(\alpha) \quad (4.27)$$

$$\left\{\sum_{k=1}^{N-1} A_kA_{k+j}\cos\left[-2\pi j f_{clk}t + \varphi_k - \varphi_{k+j}\right]\right\}_{with\ N\ highest}$$
$$= \sum_{i=1}^{N-j} A_iA_{j+i}\cos\left[2\pi j f_{clk}t - \varphi_i + \varphi_{j+i}\right] \quad (4.28)$$

Changing the cosine term to a sine term according to (4.29), and using the definition in (4.7) we yield the term in (32), which forms the second, first summation, term of (4.12).

$$\cos(\alpha) = \sin\left(\alpha + \frac{\pi}{2}\right) \tag{4.29}$$

$$\sum_{i=1}^{N-j} A_i A_{j+i} \sin\left[2\pi j f_{clk} t - \varphi_i + \varphi_{j+i} + \frac{\pi}{2}\right] = \sum_{i=1}^{N-j} \left(A_i A_{j+i}\,, \varphi_{j+i} - \varphi_i + \frac{\pi}{2}\right) \tag{4.30}$$

We now consider the second cosine term in the summation shown in (4.25), when $|k+i| = j$.

$$\left\{\sum_{k=1}^{N-1} \sum_{i=k+1}^{N} -A_k A_i \cos[2\pi(k+i) f_{clk} t + \varphi_k + \varphi_i]\right\}_{@\, H_j,\ where\ |k+i|=j \xrightarrow{yields} i=j-k} = \sum_{k=1}^{N-1} -A_k A_{j-k} \cos\left[2\pi j f_{clk} t + \varphi_k + \varphi_{j-k}\right] \tag{4.31}$$

For i to be greater than k, we write $j - k > k$, thus $k < \frac{j}{2}$, which in general, for all integer k, is expressed as $k < \left\lceil \frac{j}{2} - 1 \right\rceil$ or $k < \left\lceil \frac{j-2}{2} \right\rceil$. And, similar to the first cosine term, we replace the summation index k with i, we convert the cosine to a sine according to (4.29), and we use the definition in (4.7) to arrive at the final form of the second cosine term in (4.25), presented in (4.32), and shown as the last, second summation, term in (4.12).

$$\left\{\sum_{k=1}^{N-1} -A_k A_{j-k} \cos\left[2\pi j f_{clk} t + \varphi_k + \varphi_{j-k}\right]\right\}_{i=j-k>k} = -\sum_{i=1}^{\left\lfloor\frac{j-2}{2}\right\rfloor} \left(A_i A_{j-i}\,, \varphi_{j-i} + \varphi_i + \frac{\pi}{2}\right) \tag{4.32}$$

This concludes the derivation of (4.12).

4.1.6.2 Full Derivation of $(X^3)_{ST}$

Below we provide details on the analysis leading to (4.18) by expanding on the transition from (4.13) to (4.18) using (4.14), (4.15), and (4.16). The $[\sum_{i=1}^{N} A_i \sin(2\pi i f_{clk} t + \varphi_i)]^3$ term in (4.13) expands into three types of terms, $N \sin^3(\,)$ terms, $N(N-1) \sin^2(\,)\sin(\,)$ terms, and $N!/[3!\,(N-3)!]\ \sin(\,)\sin(\,)\sin(\,)$ terms, as shown in (4.33).

$$\begin{aligned}\left[\sum_{i=1}^{N} A_i \sin(2\pi i f_{clk} t + \varphi_i)\right]^3 &= \sum_{i=1}^{N} A_i^3 \sin^3(2\pi i f_{clk} t + \varphi_i) \\ &+ \sum_{k=1}^{N} \sum_{\substack{i=1 \\ i\neq k}}^{N} 3A_k^2 A_i \sin^2(2\pi k f_{clk} t + \varphi_k) \sin(2\pi i f_{clk} t \\ &+ \varphi_i) \\ &+ \sum_{l=1}^{N-2} \sum_{k=l+1}^{N-1} \sum_{i=k+1}^{N} 6A_l A_k A_i \sin(2\pi l f_{clk} t \\ &+ \varphi_l) \sin(2\pi k f_{clk} t + \varphi_k) \sin(2\pi i f_{clk} t + \varphi_i)\end{aligned} \tag{4.33}$$

The $\sin^3(\,)$ term in (4.33) yields, according to (4.14), two $\sin(\,)$ components, one at the same frequency of the $\sin^3(\,)$ and one at three times that frequency. Thus, for the $\sin^3(\,)$ term to yield a component that lands at H_j, it will need to be resulting from either

a term at H_j itself or a term at a third of the frequency of H_j, if j is divisible by three. Consequently, the first non-summation terms of (4.18) come from,

$$\left\{A_j^3 \sin^3\left(2\pi j f_{clk} t + \varphi_j\right) + A_{\frac{j}{3}}^3 \sin^3\left(2\pi \frac{j}{3} f_{clk} t + \varphi_{\frac{j}{3}}\right)\right\}_{@\, H_j} = \frac{3}{4} A_j^3 \sin\left(2\pi j f_{clk} t + \varphi_j\right) - \frac{1}{4} A_{\frac{j}{3}}^3 \sin\left(2\pi j f_{clk} t + 3\varphi_{\frac{j}{3}}\right) \tag{4.34}$$

where $\frac{3}{4} A_j^3 \sin\left(2\pi j f_{clk} t + \varphi_j\right) - \frac{1}{4} A_{\frac{j}{3}}^3 \sin\left(2\pi j f_{clk} t + 3\varphi_{\frac{j}{3}}\right)$ is expressed as $\left(\frac{3}{4} A_j^3, \varphi_j\right) - \left(\frac{1}{4} A_{\frac{j}{3}}^3, 3\varphi_{\frac{j}{3}}\right)$ per the definition in (4.7).

The $\sin^2(\,)\sin(\,)$ term in (4.33) expands according to (4.15) to three $\sin(\,)$ terms, as shown below.

$$\sum_{k=1}^{N} \sum_{\substack{i=1 \\ i \neq k}}^{N} 3A_k^2 A_i \sin^2(2\pi k f_{clk} t + \varphi_k) \sin(2\pi i f_{clk} t + \varphi_i) = \sum_{k=1}^{N} \sum_{\substack{i=1 \\ i \neq k}}^{N} 3A_k^2 A_i \left[\frac{1}{2}\sin(2\pi i f_{clk} t + \varphi_i) + \frac{1}{4}\sin(2\pi(2k-i) f_{clk} t + 2\varphi_k - \varphi_i) - \frac{1}{4}\sin(2\pi(2k+i) f_{clk} t + 2\varphi_k + \varphi_i)\right] \tag{4.35}$$

Starting with the first term, i has to be equal to j for all values of k, except for $k = j$.

$$\left\{\sum_{k=1}^{N} \sum_{\substack{i=1 \\ i \neq k}}^{N} 3A_k^2 A_i \frac{1}{2}\sin(2\pi i f_{clk} t + \varphi_i)\right\}_{i=j, i \neq k} = \sum_{\substack{k=1 \\ k \neq j}}^{N} 3A_k^2 A_j \frac{1}{2}\sin\left(2\pi j f_{clk} t + \varphi_j\right) \tag{4.36}$$

Replacing the summation variable k with i and using the definition in (4.7), (4.36) can be rewritten as $\frac{3}{2}A_j \sum_{i=1,i\neq j}^{N}\left(A_i^2, \varphi_j\right)$.

For the second term of (4.35), $|2k-i|$ has to be equal to j; thus, $i = 2k \pm j$ for all values of k, except for $k = i$, which translates to the condition $k \neq \mp j$. The second term is thus composed of two summations. Starting with the summation corresponding to $i = 2k - j$, we express it as follows, where δ_x is as defined in (4.17).

$$\left\{\sum_{k=1}^{N}\sum_{\substack{i=1\\ i\neq k}}^{N}\frac{3}{4}A_k^2 A_i \sin(2\pi(2k-i)f_{clk}t + 2\varphi_k - \varphi_i)\right\}_{i=2k-j,i\neq k} = \sum_{k=1+\left\lfloor\frac{j}{2}\right\rfloor,k\neq j}^{\left\lfloor\frac{N+j}{2}\right\rfloor}\frac{3}{4}A_k^2 A_{2k-j}\sin\left(2\pi j f_{clk}t + 2\varphi_k - \varphi_{2k-j}\right) \tag{4.37}$$

The start point for k is based on making $2k - j \geq 1 \xrightarrow{yields} k \geq \left\lceil\frac{j+1}{2}\right\rceil$, which can also be expressed as $k \geq 1 + \left\lfloor\frac{j}{2}\right\rfloor$. The upper limit for k is based on ensuring that $2k - j \leq N \xrightarrow{yields} k \leq \left\lfloor\frac{N+j}{2}\right\rfloor$. Replacing the index k with an index i, such that $i = k - \left\lfloor\frac{j}{2}\right\rfloor$, yields an index start and end limits of 1 and $\left\lfloor\frac{N+j}{2}\right\rfloor - \left\lfloor\frac{j}{2}\right\rfloor$, respectively, and changes the subscripts k and $2k - j$ inside the summation to $i + \left\lfloor\frac{j}{2}\right\rfloor$ and $2\left(i + \left\lfloor\frac{j}{2}\right\rfloor\right) - j = 2i - \delta_j$, respectively, as presented as the second summation in (4.18).

Note that the condition $k \neq j$ translates as $i \neq j - \left\lfloor\frac{j}{2}\right\rfloor = \left\lceil\frac{j}{2}\right\rceil$ for i. We continue with the second term of (4.35) for the condition $i = 2k + j$ while ignoring the trivial exception $k \neq -j$.

$$\left\{\sum_{k=1}^{N}\sum_{\substack{i=1\\ i\neq k}}^{N}\frac{3}{4}A_k^2A_i\sin(2\pi(2k-i)f_{clk}t+2\varphi_k-\varphi_i)\right\}_{i=2k+j} = \sum_{k=1}^{\left\lfloor\frac{N-j}{2}\right\rfloor}\frac{3}{4}A_k^2A_{2k+j}\sin\left(-2\pi jf_{clk}t+2\varphi_k-\varphi_{2k+j}\right) \tag{4.38}$$

The upper limit for k is based on ensuring that $2k+j\le N \xrightarrow{yields} k\le\left\lfloor\frac{N-j}{2}\right\rfloor$. Replacing the summation index k with index i yields the third summation term of (4.18).

For the third term of (4.35), $|2k+i|$ has to be equal to j, thus $i=j-2k$, for all values of k, less $k=i$, which translates to the condition $k\neq\frac{j}{3}$.

$$\left\{\sum_{k=1}^{N}\sum_{\substack{i=1\\ i\neq k}}^{N}-\frac{3}{4}A_k^2A_i[\sin(2\pi(2k+i)f_{clk}t+2\varphi_k+\varphi_i)]\right\}_{i=j-2k,k\neq\frac{j}{3}} = -\sum_{k=1,k\neq\frac{j}{3}}^{\left\lfloor\frac{j-1}{2}\right\rfloor}\frac{3}{4}A_k^2A_{j-2k}\sin\left(2\pi jf_{clk}t+2\varphi_k+\varphi_{j-2k}\right) \tag{4.39}$$

The upper limit for k is based on ensuring that $j-2k\ge 1 \xrightarrow{yields} k\le\left\lfloor\frac{j-1}{2}\right\rfloor$. Replacing the index k with index i yields the fourth summation term of (4.18), and concludes the derivation for the terms of (4.35), which completes the derivation for the second term of (4.33), the $\sin^2(\,)\sin(\,)$ term.

In (4.40), the third and last term of (4.33), the $\sin(\,)\sin(\,)\sin(\,)$ term, expands according to (4.16) to four sine terms. Because $l\neq k\neq i\neq 0$, it can be shown that for a given set of l, k, and i, only one of $(l-k+i)$, $(l+k-i)$, $(-l+k+i)$, or $(l+k+i)$ can be equal to j. For example, if $(l-k+i)=j$, then $(l+k-i)=j-2(i-k)$, $(-l+k+i)=j-2(l-k)$, and $(l+k+i)=j+2k$.

$$\sum_{l=1}^{N-2}\sum_{k=l+1}^{N-1}\sum_{i=k+1}^{N} 6A_lA_kA_i \sin(2\pi l f_{clk}t+\varphi_l)\sin(2\pi k f_{clk}t + \varphi_k)\sin(2\pi i f_{clk}t+\varphi_i)$$
$$= \sum_{l=1}^{N-2}\sum_{k=l+1}^{N-1}\sum_{i=k+1}^{N} \frac{3}{2}A_lA_kA_i[\sin(2\pi(l-k+i)f_{clk}t + \varphi_l - \varphi_k + \varphi_i) + \sin(2\pi(l+k-i)f_{clk}t + \varphi_l + \varphi_k - \varphi_i) + \sin(2\pi(-l+k+i)f_{clk}t - \varphi_l + \varphi_k + \varphi_i) - \sin(2\pi(l+k+i)f_{clk}t + \varphi_l + \varphi_k + \varphi_i)] \quad (4.40)$$

We start with the term corresponding to $l+k+i=j$, and rewrite the summation as follows.

$$\left\{\sum_{l=1}^{N-2}\sum_{k=l+1}^{N-1}\sum_{i=k+1}^{N} -\frac{3}{2}A_lA_kA_i \sin(2\pi(l+k+i)f_{clk}t+\varphi_l+\varphi_k+\varphi_i)\right\}_{l+k+i=j}$$
$$= \sum_{l=1}^{\left\lfloor\frac{j-3}{3}\right\rfloor}\sum_{k=1}^{\left\lceil\frac{j-3l-2}{2}\right\rceil} -\frac{3}{2}A_lA_{k+l}A_{j-(k+2l)} \sin\left(2\pi j f_{clk}t+\varphi_l+\varphi_{k+l}+\varphi_{j-(k+2l)}\right) \quad (4.41)$$

In (4.41), the summation indices are shifted. Whereas in the left side of the equation k starts at $(l+1)$, it starts at 1 in the right side of the equation, with the offset l being accounted for by replacing k with $k+l$ everywhere in the equation. Thus, the condition $l+k+i=j$ becomes $l+(k+l)+i=j \xrightarrow{yields} i=j-(k+2l)$. The upper limit for l is determined based on the highest indices summation $l+(l+1)+(l+2)=j \xrightarrow{yields} l=\frac{j-3}{3}$, and generally for a j that is a non-multiple of 3, the upper limit for l is $l=\left\lfloor\frac{j-3}{3}\right\rfloor$. The upper limit for k is determined based on the condition that the index $j-(k+2l)$ is greater than the index $k+l$, which is written as follows: $j-k-2l > k+l \xrightarrow{yields} k<\frac{j-3l}{2}$. For all integer values of j and l, we write the condition as $k \leq$

$\left\lceil\frac{j-3l}{2}\right\rceil - 1 = \left\lceil\frac{j-3l-2}{2}\right\rceil$. The result in (4.41), with a replacement of the summation variable l with k, and k with i, forms the last shown term of (4.18).

The term that corresponds to $-l + k + i = j$ expands as shown below in (4.42).

$$\begin{aligned}&\left\{\sum_{l=1}^{N-2}\sum_{k=l+1}^{N-1}\sum_{i=k+1}^{N}\frac{3}{2}A_lA_kA_i\sin(2\pi(-l+k+i)f_{clk}t-\varphi_l+\varphi_k\right.\\&\left.\qquad+\varphi_i)\right\}_{-l+k+i=j}\\&=\sum_{l=1}^{j-3}\sum_{k=1}^{\left\lceil\frac{j-l-2}{2}\right\rceil}\frac{3}{2}A_lA_{k+l}A_{j-k}\sin\big(2\pi jf_{clk}t-\varphi_l+\varphi_{k+l}\\&\qquad+\varphi_{j-k}\big)\end{aligned}\tag{4.42}$$

The indices in (4.42) are shifted as in (4.41). The condition $k + l < j - k \xrightarrow{yields} l < j - 2k$ indicates that for a minimum k of 1, $l < j - 2 \xrightarrow{yields} l \leq j - 3$, hence the upper limit of l is $j - 3$. The same condition above indicates that $k < \frac{j-l}{2} \xrightarrow{yields} k \leq \left\lceil\frac{j-l}{2}\right\rceil - 1 = \left\lceil\frac{j-l-2}{2}\right\rceil$, hence the upper limit for k is $\left\lceil\frac{j-l-2}{2}\right\rceil$. The result in (4.42), with a replacement of the summation variable l with k, and k with i, forms the first double summation term of (4.18).

The term that corresponds to $l - k + i = j$ expands as shown below in (4.43).

$$\begin{aligned}&\left\{\sum_{l=1}^{N-2}\sum_{k=l+1}^{N-1}\sum_{i=k+1}^{N}\frac{3}{2}A_lA_kA_i\sin(2\pi(l-k+i)f_{clk}t+\varphi_l-\varphi_k+\varphi_i)\right\}_{l-k+i=j}\\&=\sum_{l=1}^{j-1}\sum_{k=1}^{N-j}\frac{3}{2}A_lA_{k+l}A_{j+k}\sin\big(2\pi jf_{clk}t+\varphi_l-\varphi_{k+l}+\varphi_{j+k}\big)\end{aligned}\tag{4.43}$$

The indices in (4.43) are shifted as in (4.41) and (4.42). The condition $k + l < j + k \xrightarrow{yields} l < j$ indicates that the upper limit of l is $j - 1$. The condition $j + k \leq N \xrightarrow{yields} k \leq N - j$ indicates that the upper limit for k is $N - j$. The result in (4.43), with a

replacement of the summation variable l with k, and k with i, forms the second double summation term of (4.18). Finally, the term that corresponds to $l + k - i = j$ expands as shown below in (4.44).

$$\begin{aligned}&\left\{\sum_{l=1}^{N-2}\sum_{k=l+1}^{N-1}\sum_{i=k+1}^{N}\frac{3}{2}A_lA_kA_i\sin(2\pi(l+k-i)f_{clk}t+\varphi_l+\varphi_k-\varphi_i)\right\}_{l+k-i=j}\\&\quad=\sum_{l=j+1}^{\left\lceil\frac{N+j-1}{2}\right\rceil}\sum_{k=1}^{N+j-2l}\frac{3}{2}A_lA_{k+l}A_{2l+k-j}\sin\big(2\pi jf_{clk}t+\varphi_l+\varphi_{k+l}\\&\quad-\varphi_{2l+k-j}\big)\end{aligned}\tag{4.44}$$

The indices in (4.44) are shifted as in (4.41), (4.42), and (4.43). The condition $k + l < 2l + k - j \xrightarrow{yields} l > j$ indicates that the lower limit of l is $j + 1$. The condition $2l + k - j \leq N \xrightarrow{yields} l \leq \frac{N+j-k}{2}$ indicates that for a minimum k of 1, $l \leq \frac{N+j-1}{2}$, hence the upper limit for l is $\left\lceil\frac{N+j-1}{2}\right\rceil$. The same latter condition dictates that $k \leq N + j - 2l$, which sets the upper limit for k to $N + j - 2l$. The result in (4.44), with a replacement of the summation variable l with k, and k with i, forms the third double summation term of (4.18). This concludes the derivation for the third and last term of (4.33), which also completes the derivation for (4.18).

4.1.7 ON COMPUTING THE MATRIX COEFFICIENTS

In the previous sections, Sections 4.1.3 and 4.1.6, the matrix coefficients $(X)_{ST}$, $(X^2)_{ST}$, and $(X^3)_{ST}$ are computed from the spectral components of the MTSG signal. An equivalent time domain-based approach allows the computation of the matrix coefficients from the time-domain description of the MTSG signal. In the time-domain approach, the non-linearity is applied to the time domain signal before the Fourier transform is applied to it. Thus, $F\{X(t)\} \rightarrow [(X)_{ST}]$, $F\{X^2(t)\} \rightarrow [(X^2)_{ST}]$, and $F\{X^3(t)\} \rightarrow [(X^3)_{ST}]$, where $F\{X\}$ is the Fourier of X, and where $[(X)_{ST}]$, $[(X^2)_{ST}]$, and $[(X^3)_{ST}]$ are the arrays

consisting of $(X)_{ST}$, $(X^2)_{ST}$, and $(X^3)_{ST}$ at all the harmonic frequencies, respectively. However, whereas the spectral approach shown in the previous section presents the expressions of $(X)_{ST}$, $(X^2)_{ST}$, and $(X^3)_{ST}$ in terms of elementary functions, it is not possible to do so in the time-domain approach without making assumptions about the MTSG time-domain signal shape. The spectral approach presented above makes no assumptions about the MTSG signal shape and consequently models all the amplitudes and phases of the signal harmonics as arbitrary and independent. The expression forms presented in Section 4.1.3 and derived in detail in Section 4.1.6 are considered closed-form expressions for finite N, which is the case in this methodology, as is discussed in more detail in the simulation and experimental sections that follow.

4.2 Simulation Results

4.2.1 SYSTEM MODELING

A transient simulation was used to verify and validate the proposed test methodology, where the system components have been modeled to represent the actual ones used in the experimental setup discussed in Section 4.3. The MTSG was modeled to reflect a pulse-width of 75 psec and a signal rise-time of 50 psec, and a low-pass filter was added to the model as a bandwidth limiter, whose parameters were empirically tuned to approximate the response seen in the hardware bandwidth limiter used in the experimental setup. The DUT receiver was modeled as a multistage memory-less system and included an LNA, a mixer, a TIA with a single-pole, three bi-quad stages, and a PGA stage, all with specific gains (GM for mixer and Z for TIA), NF, and IIP3 parameters closely approximating the real DUT used in Section 4.3. The proposed test methodology was fully implemented in simulation in a manner that emulates the experimental setup.

Additionally, a standard measurement test bench was also simulated and used as a reference.

4.2.2 DETAILED RESULTS ON MODELED DUT

The modeled DUT was tested in simulation using both the standard measurement methods (i.e. single-tone test for gain and NF, and two-tone test for IIP3) and the MTSG proposed method, and the results compared as shown in Fig. 4.1. Fig. 4.2 shows the details of the MTSG-based measurement simulation at 650 MHz. Y_{ST}'s amplitude, as well as its phase referenced to the phase corresponding to the first MTSG level, is measured for all MTSG levels, and then a complex LS regression is applied to find the complex parameters α_1 and α_3 and consequently extract gain and IIP3 at 650 MHz. Fig. 4.2c presents both the MTSG-Based extracted measurements as well as the corresponding standard measurement values for gain and IIP3 at 650 MHz.

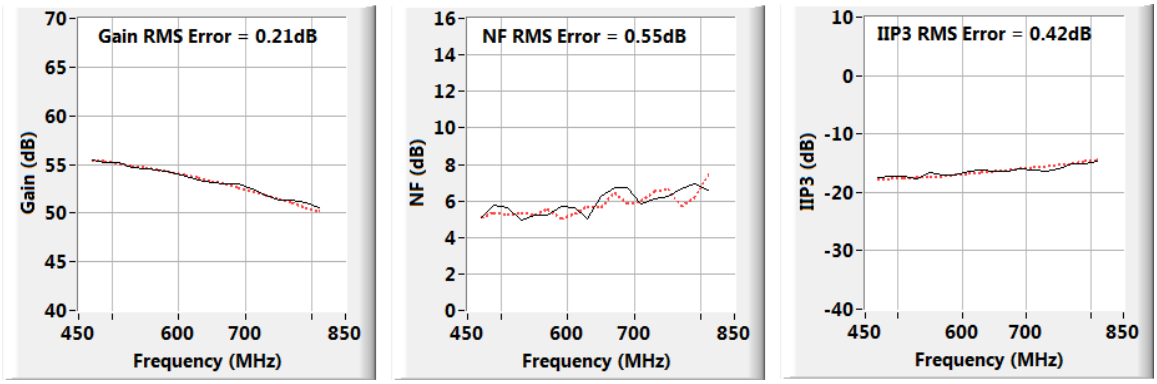

(a) (b) (c)

Fig. 4.1: Comparison of MTSG-based (solid) and standard (dashed) results
(a) Gain (b) Noise Figure (c) Input 3rd Order Intercept Point

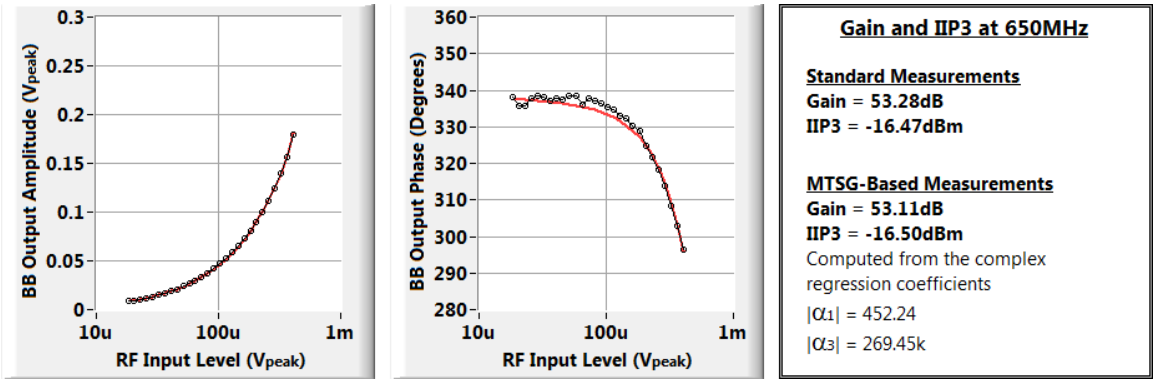

(a) (b) (c)

Fig. 4.2: Simulated MTSG-based measurement (points) and LS regression (plain) of the complex baseband signal Y_{ST} for LO frequency 650 MHz (a) Y_{ST} amplitude vs. H_j amplitude (b) Y_{ST} amplitude vs. H_j amplitude (c) Extracted parameters

4.2.3 PROPER CHOICE OF N

Another aspect of the proposed method is the proper choice of N where N is first defined in (4.1). Considering the analysis involved in the proposed methodology, covered in Sections 4.1.2 and 4.1.3, one can easily see how the choice of N can impact the resulting extracted parameters. For this reason, it is important to provide guidance as to how to properly choose N.

An empirical study on the proper choice of N was carried out as part of the MTSG-based measurement simulation on this DUT, whose results are presented in Fig. 4.3, and was then redone with the experimental data, which is presented in Section 4.3. Fig. 4.3a shows the cumulative power in the harmonics considered versus N. Expectedly, as N increases, the cumulative power of the considered harmonics approach 100%, which indicates that with the proper choice of N, the remaining harmonics can contribute very little to the total power of the signal. Fig. 4.3b shows the RMS error in extracted IIP3 values versus N. The general trend by which the error decreases as we

consider more harmonics of the MTSG is as expected. Fig. 4.3c combines the information shown in Fig. 4.3a and Fig. 4.3b to present the IIP3 RMS error versus the considered cumulative power of the MTSG. Based on the results of this study, an acceptable RMS error can be achieved when the computations account for around 90% of the MTSG signal power, which corresponds to all MTSG tones up to the 90th harmonic in the case of the simulated MTSG.

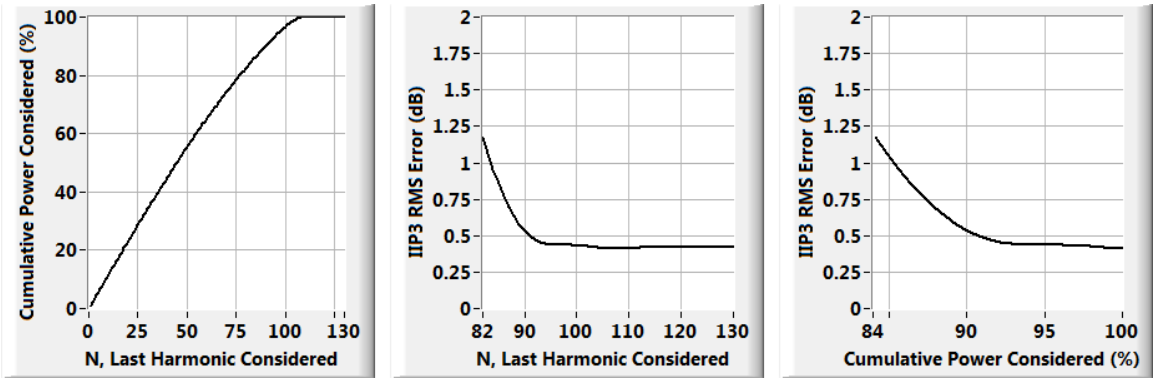

(a) (b) (c)

Fig. 4.3: Results of the study on the proper choice of N (a) Cumulative power vs. N (b) IIP3 RMS error vs. N (c) IIP3 RMS error vs. Cumulative Power

For MTSG hardware whose response far exceeds the DUT's bandwidth, characterization of the MTSG hardware can be made more efficient (i.e. N can be limited) by using a low-pass filter (LPF) as part of the test system. This also makes the offline computation of the matrix in (4.19) or (4.20) more efficient. For Section 4.3 on experimental results, a discrete LPF (Mini-Circuits SLP-1000+), with a bandwidth of ~1 GHz was used, as the used DUT's bandwidth of operation is limited to 800 MHz.

4.2.4 THE EFFECT OF MTSG SHAPING

As touched on briefly in Section 4.1.3, the methodology's analysis assumes that α_3 is frequency independent within the receiver bandwidth. Thus, predicted IIP3 can be more flat and less accurate than that measured using standard methods. MTSG shaping can be implemented to mitigate this problem. MTSG shaping involves mathematically shaping the known MTSG response for linearity computation purposes, in such a way to exaggerate the tones where the linearity of the DUT is expected to be better. Since the physical MTSG hardware does not change, the measured response Y_{ST} does not change either, and hence using a higher input tone level in the computation yields better linearity. Analytically, starting from (4.5) and multiplying the input signal X with a frequency-dependent coefficient k (i.e. a shaping filter) results in having different extracted DUT parameters α_1, α_2, and α_3 because the measured output Y_{ST} is unchanged. We denote the new DUT parameters with a subscript k to yield the form in (4.45).

$$Y_{ST} = \alpha_{1_k}(kX)_{ST} + \alpha_{2_k}((kX)^2)_{ST} + \alpha_{3_k}((kX)^3)_{ST} \tag{4.45}$$

The matrix coefficients $(kX)_{ST}$, $((kX)^2)_{ST}$, and $((kX)^3)_{ST}$ can be calculated from (4.6), (4.12), and (4.18) respectively, and hence α_{1_k} and α_{3_k} can be found per (4.19) or (4.20). For designing k for a given DUT, using a filter whose response trend is the inverse of a nominal DUT response trend is often sufficient. Tuning k to minimize the IIP3 error for the nominal receiver can also be done. Fig. 4.4a shows the simulated nominal DUT response having approximately 5.5 dB of roll-off. The k designed in the case of the simulated DUT is a high-pass filter composed of two cascaded first order filters whose 3 dB point is at 800 MHz. The response of k is shown in Fig. 4.4b having approximately 6 dB gain increase over the same bandwidth as the nominal DUT gain. The response shown in Fig. 4.4b has a trend that approximates the inverse of the response

trend shown in Fig. 4.4a, ignoring the absolute level of either response. The absolute level of k does affect the outcome when solving for α_{1_k} and α_{3_k}, and thus it needs to be accounted for when computing α_1 and α_3 from α_{1_k} and α_{3_k}, respectively. Given that measured Y_{ST} is unchanged, the first, second, and third order components of Y_{ST} are also unchanged. Hence,

$$\alpha_{1_k}(kX)_{ST} = \alpha_1(X)_{ST} \tag{4.46}$$

and

$$\alpha_{3_k}((kX)^3)_{ST} = \alpha_3(X^3)_{ST}. \tag{4.47}$$

Therefore, when computing α_1 from α_{1_k} and α_3 from α_{3_k} the ratio of their respective coefficients, i.e. $(kX)_{ST}/(X)_{ST}$ and $((kX)^3)_{ST}/(X^3)_{ST}$, should be known. Considering (4.6) it follows that $(kX)_{ST}/(X)_{ST}$ is k itself, whose response is shown in Fig. 4.4b. $((kX)^3)_{ST}/(X^3)_{ST}$ is more challenging and requires the separate computation of $((kX)^3)_{ST}$ and $(X^3)_{ST}$ from (4.18) and taking the ratio of the two. The computed response of $((kX)^3)_{ST}/(X^3)_{ST}$ is shown in Fig. 4.4c. Whereas α_1 can be computed as $\alpha_{1_k}(kX)_{ST}/(X)_{ST}$ or $k\alpha_{1_k}$, α_3 is computed as $\beta\alpha_{3_k}$, where β is a constant equal to $((kX)^3)_{ST}/(X^3)_{ST}$ evaluated at the peak of the response in the band of operation. The difference in the treatment of α_1 and α_3 is due to that α_{1_k} is accurately computed, as a frequency dependent parameter, at each frequency, whereas α_{3_k} is not. In the use case presented in this section, the $((kX)^3)_{ST}/(X^3)_{ST}$ response peaks around -29.3 dB or ~ 0.034.

Fig. 4.5a and Fig. 4.5b show the MTSG simulated IIP3 measurement with and without shaping used (solid lines) in comparison to IIP3 simulated measurement using the reference standard two-tone method (dashed lines). The non-shaped MTSG measured

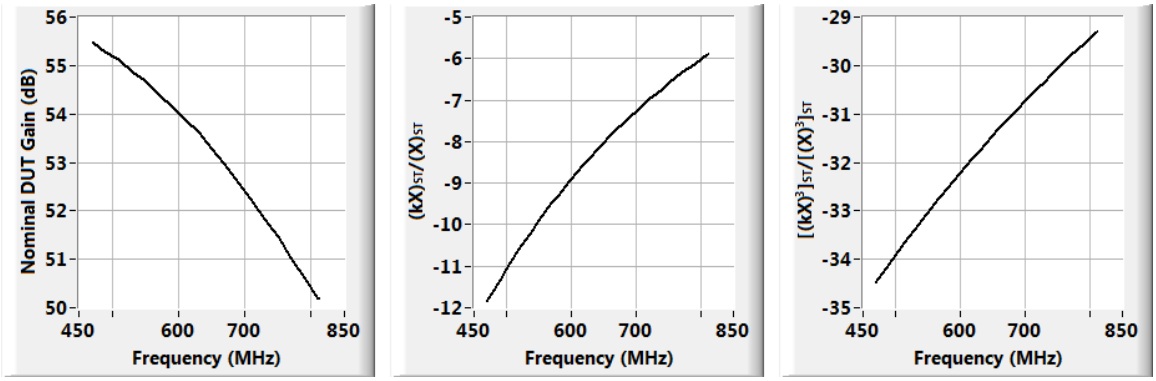

(a) (b) (c)

Fig. 4.4: Design of shaping filter *k* and its effect on matrix elements (a) Nominal DUT response (b) Change in coefficient of α_1 (c) Change in coefficient of α_3

IIP3 reflects a more flat, less accurate response. As one can see, the MTSG measured IIP3 follows the actual IIP3 trend versus frequency more closely when shaping is used. Fig. 4.5c shows the error between the MTSG measured IIP3 and the standard measured IIP3 for each of two cases, without (solid line) and with (dashed line) MTSG shaping used. The error in the case where shaping is used is more flat across the frequency range and is limited to less than 1 dB in magnitude, whereas the error in the case where shaping is not used is tilted, such that it is positive for lower frequencies and negative for higher frequencies, and ranges up to ~ 1.5 dB in magnitude. The RMS error, considering the whole band, is 0.42 dB when shaping is used and 0.95 dB when shaping is not used.

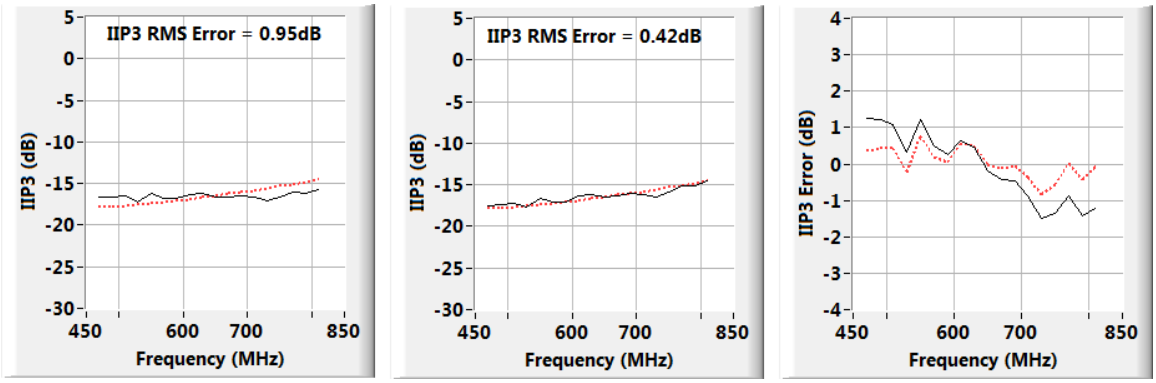

(a) (b) (c)

Fig. 4.5: MTSG IIP3 measurements without and with shaping compared to standard measurements and the IIP3 error in each (a) IIP3 measurement without shaping (b) IIP3 with shaping (c) IIP3 error (MTSG – Standard)

4.2.5 MONTE-CARLO: RESULTS ON DUT VARIATION

The DUT modeled and simulated in this section is based on an actual DUT tested in Section 4.3. To account for part-to-part variation and its impact on the effectiveness of the proposed approach, a Monte-Carlo simulation was performed to test variations of the modeled DUT, where the various block parameters are altered and nominal as well as corner cases are selected to represent the DUT population. It is worth noting that the k designed for MTSG shaping is kept the same for all DUTs and is based on the nominal DUT.

Fig. 4.6 shows the RF performance of the selected DUT population as measured using standard methods. These measurements form the reference for the MTSG measurements done on the same population of DUTs. Fig. 4.7 shows the error involved in measuring the RF performance parameters using the proposed MTSG-based approach for the same DUT population. The simulation results show an overall RMS error of 0.235 dB for gain, 0.640 dB for NF, and 0.882 dB for IIP3.

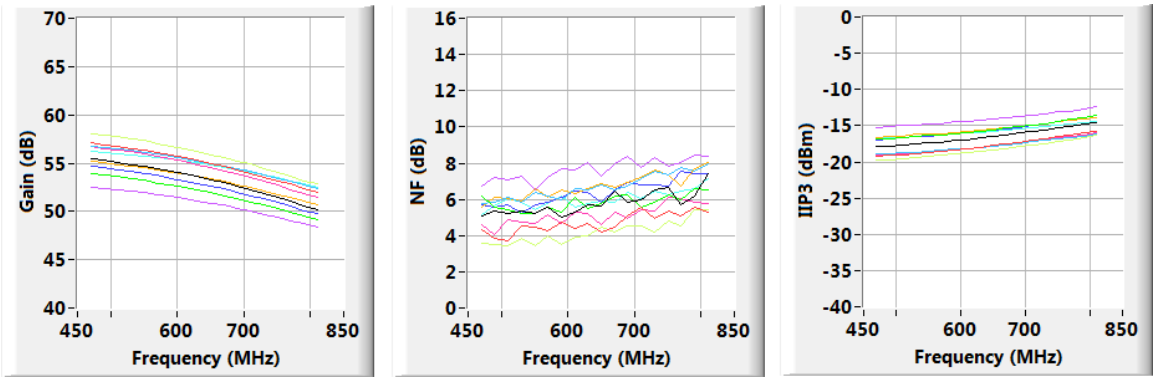

(a) (b) (c)

Fig. 4.6: RF performance of DUT population (a) Gain (b) NF (c) IIP3

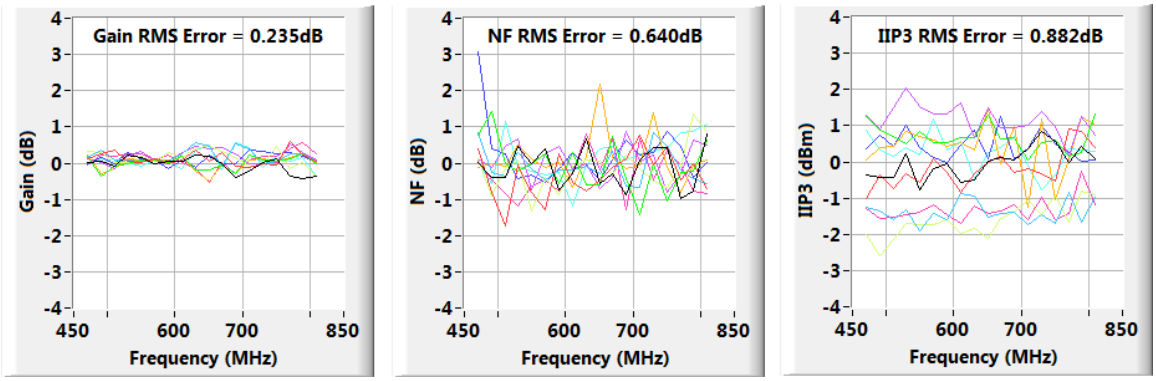

Fig. 4.7: MTSG measurements error for DUT population (a) Gain error (b) NF error (c) IIP3 error

4.3 Experimental Results

4.3.1 Setup Description and MTSG Characterization

The proposed test method was fully-automated on a 65nm UHF receiver test bench, where MTSG hardware resided on a test board, shown in Fig. 4.8, and the signal processing was coded in LabVIEW™. BIST aspects of and the tested receiver's die photomicrograph are presented in [49]. The tone amplitude and phase of a few MTSG

units were characterized versus frequency and output attenuations, and saved as calibration data for DUT testing. Results presented in Fig. 4.9 (also shown earlier in Section 3.2.3) demonstrate MTSG performance characterization data and show that part-to-part differences in tone levels seen on two tested units are relatively small (0.33 dB RMS). As also mentioned in earlier in Section 3.2.3.2, the delay designed for this experimental setup of the MTSG was implemented via a difference of controlled trace lengths. Fig. 4.8b shows a zoomed-in image of the MTSG delay implementation, where the trace length difference is illustrated and shown to be ~ 490 mils, which on the shown board corresponds to ~75 psec of delay.

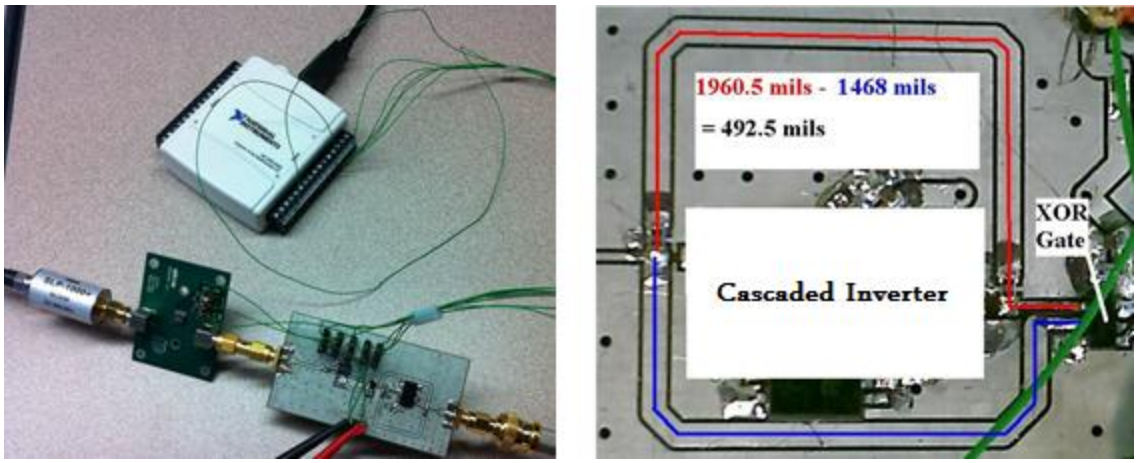

(a) (b)

Fig. 4.8: MTSG experimental setup (a) MTSG hardware setup (b) Trace-delay implementation of MTSG

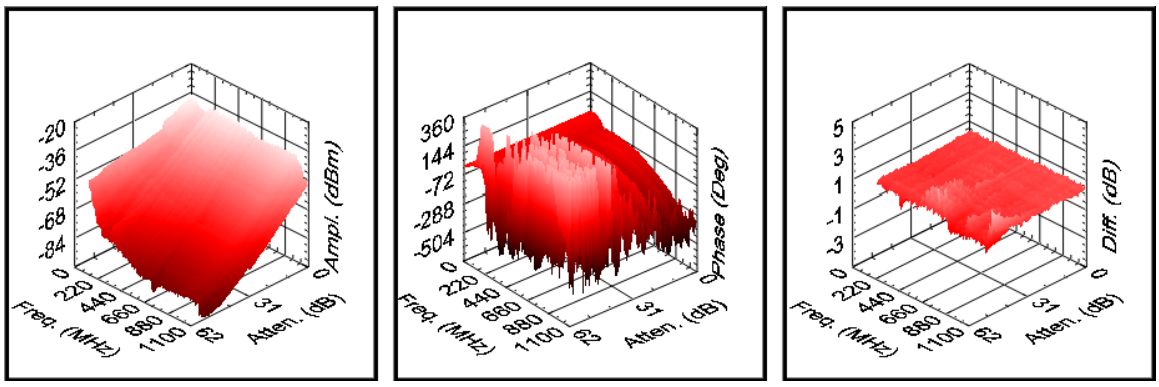

(a) (b) (c)

Fig. 4.9: MTSG characterization data and part-to-part differences (a) MTSG tone amplitude (b) MTSG tone phase (c) part-to-part amplitude differences

4.3.2 On Y_{ST} Phase Measurement

An ideal attenuator has no phase shift associated with it. However, a practical attenuator introduces phase shift at higher attenuation levels. This phase shift, if not measured, can be a source of error in the complex regression done on (4.19) or (4.20) to find α_1 and α_3, because the phase of Y_{ST} at the various attenuation levels will be assumed to be the same when it is not. While the first two of the three intermediate measurements discussed in detail in Section 3.3 are done at static MTSG levels, the third, measuring the phase-shift seen on the down-converted baseband tone, Y_{ST}, as the MTSG levels change, needs to be performed during the MTSG level transition itself. If the MTSG level is swept from 62 dB to 0 dB, for instance, then the goal is to ultimately know what the Y_{ST} amplitude is at each of these MTSG levels and what the Y_{ST} phase at each of these levels is relative to the Y_{ST}'s phase at 62 dB attenuation.

Once the baseband signal is acquired during an MTSG level transition, as shown in Fig. 4.10, signal processing is employed to find the phase shift induced by the MTSG level change. The custom signal processing developed for this purpose synthesizes a

signal that is synchronous to and based on pre- transition Y_{ST}. The synthesized signal continues unchanged after the transition, and thus the phase-shift can be measured between the synthesized signal and post-transition Y_{ST}. The phase measurement method is discussed in detail in Section 3.4. Fig. 4.10a and Fig. 4.10b show sample captured transitions between 25 dB and 0 dB MTSG levels, going-up and going-down, respectively, at 650 MHz. The thick (black) trace is the real signal Y_{ST} undergoing transition and the thin (red) trace is the synthesized signal that is synchronous and equal to pre-transition Y_{ST}. As expected, the phase-shift seen in both cases is approximately equal in magnitude and opposite in sign. Fig. 4.10c provides a big picture 3D summary of the phase-shifts measured for all MTSG levels relative to attenuation of 62 dB, at all frequencies.

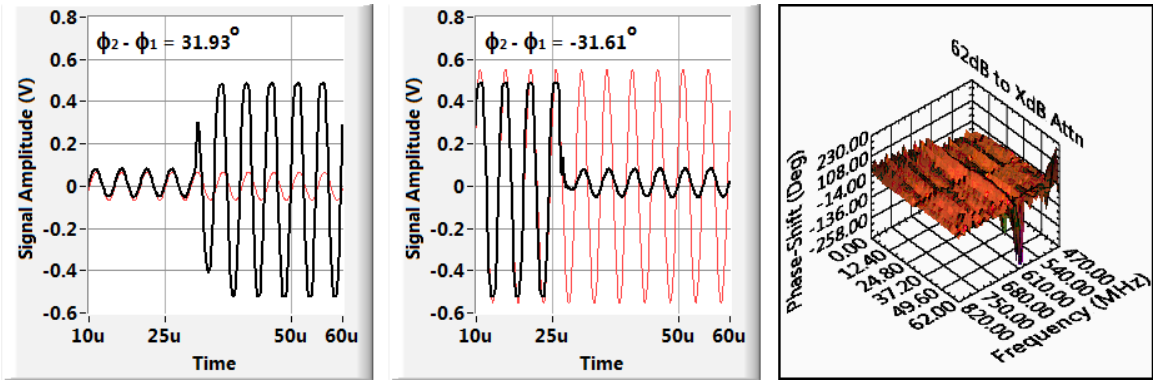

(a) (b) (c)

Fig. 4.10: Y_{ST} phase-shift ($\Delta\phi$) due to MTSG transition, sample up and down transition @ 650 MHz, and a summary 3D graph (a) 25dB-to-0dB ($\Delta\phi$) @ 650 MHz (b) 0dB-to-25dB ($\Delta\phi$) @ 650 MHz (c) 62dB-to-XdB Y_{ST} $\Delta\phi$

4.3.3 RF PARAMETER EXTRACTION AND RESULT COMPARISON

Fig. 4.11 presents the measurement results from testing the 65nm UHF DUT receiver and shows that the phase-aware MTSG-based measurement performs fairly well compared to standard RF measurement methods. The method and the results, published in [47], reflect an improvement of at least 1 dB on the central IIP3 measurement over the amplitude-only regression methodology, briefly discussed earlier in Section 4.1.4.2 and published in [46]. Fig. 4.11a, b, and c show the gain, NF, and IIP3 responses measured with a RMS error across the frequency range of only 0.38 dB, 0.74 dB, and 0.95 dB respectively.

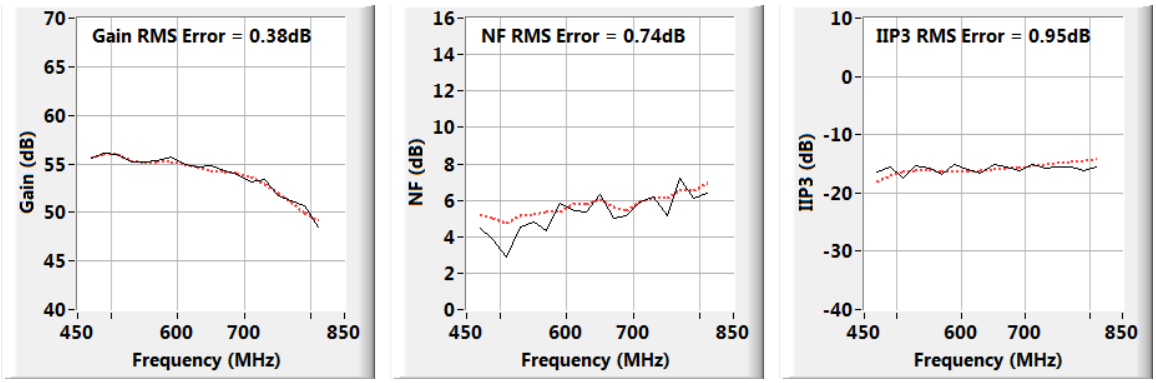

(a) (b) (c)

Fig. 4.11: Comparison of MTSG-based (solid) and standard (dashed) results (a) Gain (b) NF (c) IIP3

4.3.4 PROPER CHOICE OF *N*

As mentioned earlier in Section 4.1.2, the section on experimental results studies the proper choice of N. Fig. 4.12 presents the results of the hardware measurement-based study on the proper choice of N, similar to the ones presented in Section 4.2.3 based on simulation data. The measurement data seems to agree with the simulation data on the

percentage of harmonic power needed to be accounted for in order to achieve the settled IIP3 RMS error. Fig. 4.12b shows that the IIP3 RMS error settles close to its final value after the 90th harmonic is considered, which is shown in Fig. 4.12c to correspond to around 90% of the harmonic power content of the signal. The residual RMS error, observed to a lesser extent in Section 4.2.3, can be attributed to a few sources, some of which relate to inherent assumptions made using this methodology. Limiting the DUT non-linear model to 3rd order (i.e. assuming 4th, 5th…order non-linearity is zero), is one example. Moreover, while the MTSG shaping technique attempts to mitigate the frequency-independence assumption concerning the model's non-linear coefficients, the designed shaping filter is generally not perfect and can have residual errors.

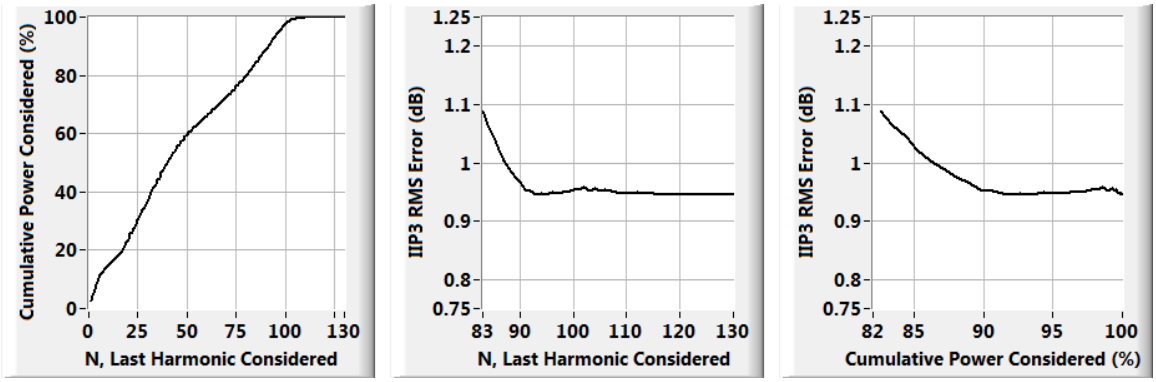

(a) (b) (c)

Fig. 4.12: Results of the study on the proper choice of *N* (a) Cumulative power vs. *N* (b) IIP3 RMS error vs. *N* (c) IIP3 RMS error vs. Cumulative Power

4.4 On Measuring Gain-Related Parameters

In exactly the same way the gain of the DUT can be measured at high attenuation levels, as discussed in Section 4.1.4.1 towards writing (4.20), other DUT parameters, such as baseband filter-related parameters or IQ imbalance parameters can be measured using the MTSG signal and basic baseband processing. Such measurements are almost free to obtain given the system in-place, including the signal generation and the basic measurement blocks available. Below we address a few of the relevant measurements.

4.4.1 BASEBAND FILTER-RELATED MEASUREMENTS

4.4.1.1 Traditional Method

All baseband filter parameters (filter 3 dB BW, filter rejection…etc) can be computed once a filter response is measured. To measure the filter response of a receiver, traditionally, a single-tone signal generator is used. The input frequency of the single tone, initially parked at a frequency corresponding to or close to a specific channel center, and thus appearing at or close to DC in baseband, is swept across the filter bandwidth, with the DUT settings, including LO frequency, kept the same. This results in the baseband signal moving across the baseband frequency of the filter, where at each location or frequency, the gain (absolute or relative to the first measurement) can be computed to yield the filter response. While technically the response measured as such includes an RF component to it, resulting from the roll-off of the RF response superimposed over the baseband response, it is typically very minimal across the baseband filter bandwidth (a few MHz), especially compared to the inherent baseband filter response itself. This traditional method, also assumes that the amplitude of the used RF signal at the DUT's input is constant as the frequency is swept. This is also typically a

fair assumption, given that the frequency sweep of the RF signal is very small (a few MHz for an RF signal that is at a few hundreds of MHz or a few GHz).

4.4.1.2 MTSG Method

The only change in measuring the baseband filter-related parameters in this methodology lies in the measurement of the filter response itself. All the computation of the various filter parameters remain the same. For measuring the filter response at a given channel using the MTSG signal, the DUT LO is tuned close to the single tone component of the MTSG that is close to or at the center of the channel. Then, instead of tuning the input signal away from the LO, the DUT LO itself is tuned away from the input "single-tone", since it is non-tunable. The resulting baseband single tone output gets swept across the baseband filter bandwidth, where measuring the gain at each location results in the filter response, in the same manner it was found in Section 4.4.1.1. Note that when extracting the single-tone information at baseband in order to compute the absolute or relative gain, the baseband frequency search window will have to be defined properly. As the LO is tuned away from the specific RF tone used, it gets closer to the neighboring tone within the MTSG signal. Thus as the resulting output tone moves higher in frequency along the baseband bandwidth, another tone may appear at lower frequency at potentially higher level. The baseband search window has to always correspond to the known location of the expected tone. With the filter response found, say normalized to its gain at low frequency (e.g. 10 kHz or 100 kHz), the 3 dB filter BW can be found by tracing the filter response and looking for the frequency point resulting in closest loss to 3 dB. The filter ripple can be found by taking the filter peak response below the 3 dB BW and comparing it to the filter minimum response within the 3 dB BW. The filter rejection

at specific frequencies can also be assessed directly from the normalized filter response at those frequencies.

4.4.2 RESIDUAL SIDEBAND / IQ-IMBALANCE MEASUREMENTS

Measuring the IQ imbalance of a receiver, traditionally requires a single tone at the desired RF frequency and baseband processing of the I and Q outputs, just as if a gain measurement is performed. The I and Q signals, baseband single tones for a single-tone RF input, ideally have the same amplitude and a 90° phase-shift between them. Keeping the baseband processing the same, to look for amplitude imbalance and phase-shift deviation from 90°, and simply replacing the RF input with the proposed MTSG signal (at a high or proper attenuation level), one would be able to do the same measurement with no change to the procedure.

4.5 Conclusion

In this dissertation, we have demonstrated that the phase-aware MTSG method, a digitally-assisted RF receiver test method, requiring minimal RF equipment during test and relying instead on baseband signal processing, can extract RF performance parameters like gain with under 0.5 dB RMS error, and NF and IIP3 with a RMS errors of under 1 dB. The proposed test methodology calls for a basic digital-based comb generator circuit with level selection (MTSG), whose characteristics and performance are measured and known, and from which DUT-independent matrix elements $(X)_{ST}$, $(X^2)_{ST}$, and $(X^3)_{ST}$ can be computed during post-processing. Testing of DUTs can then proceed by characterizing the DUT's baseband response to the MTSG signal, including the down-converted single-tone (Y_{ST}), at the desired test frequencies and for the various MTSG

levels. Having the DUT baseband response and the MTSG matrix, the DUT parameters (α_1 and α_3) can be computed, and consequently, a measure of Gain, NF, and IIP3 can be determined.

The proposed approach can significantly reduce the test overhead in an RF system by enabling fast and less expensive digital and baseband testers to perform specialized RF tests. From a short-term cost perspective, it is clear that using a basic digital/baseband tester helps reduce the initial investment cost. This can be important if initial single up-front investment capital is limited, as in the case of some start-up companies. However, when discussing the general and longer term cost impact, tester cost is evaluated over the expected number of years of service and results in test time cost on the tester valued in (cost/sec). Test cost on a basic digital/baseband tester can be as low as 1 cent/sec. On an RF tester, it ranges from 4 to 6 cents/sec or more. This means that actual test time using this methodology can be 4 times longer and still be cost effective. Moreover, adding more sites per tester can be explored. Adding more sites on an RF tester translates to more RF test equipment/channels on the tester, which in turn translates to higher tester cost. While this is also true on digital baseband testers, the additional cost of adding more baseband channels is not as nearly expensive as adding RF channels. Thus, adding test sites can make the cost ratio of this method of using a digital/baseband tester, to using standard methods using RF testers even smaller.

References

[1] A. K. Lu and G. W. Roberts, "An Oversampling-Based Analog Multitone Signal Generator," *IEEE Transactions on Circuits and Systems II,* vol. 45, no. 3, pp. 391-394, March 1998.

[2] Keyzer, J. et al., "Digital Generation of RF Signals for Wireless Communications with Band-Pass Delta-Sigma Modulation," in *Microwave Symposium Digest, 2001 IEEE MTT-S International*, Pheonix, AZ, USA, 2001.

[3] M. Negreiros, A. Souza, L. Carro, and A. A. Susin, "RF Digital Signal Generation Beyond Nyquist," in *Proceedings of the 25th IEEE VLSI Test Symposium (VTS'07)*, Berkeley, CA, USA, 2007.

[4] M. Negreiros, L. Carro, and A. A. Susin, "Digital Generation of Signals for Low Cost RF BIST," in *Proceedings of the 12th IEEE European Test Symposium (ETS'07)*, Freiburg, Germany, 2007.

[5] H. H. Hsieh and L. H. Lu, "Integrated CMOS Power Sensor for RF BIST Applications," in *Proceedings of the 24th IEEE VLSI Test Symposium (VTS'06)*, Berkeley, CA, USA, 2006.

[6] C. Zhang, R. Gharpurey, and J. A. Abraham, "Built-In Test of RF Mixer Using RF Amplitude Detectors," in *Proceedings of the 8th International Symposium on Quality Electronic Design (ISQED'07)*, San Jose, CA, USA, 2007.

[7] S. S. Akbay and A. Chatterjee, "Feature Extraction Based Built-In Alternate Test of RF Components Using a Noise Reference," in *Proceedings of the 22nd IEEE VLSI Test Symposium (VTS'04)*, Napa Valley, CA, USA, 2004.

[8] A. Halder, S. Bhattacharya, and A. Chatterjee, "Automatic Multitone Alternate Test Generation for RF Circuits Using Behavioral Models," in *Proceedings of the ITC International Test Conference*, Charlotte, NC, USA, 2003.

[9] S. Cherubal, R. Voorakaranam, A. Chatterjee, J. Mclaughlin, J. L. Smith, and D. M. Majernik, "Concurrent RF Test Using Optimized Modulated RF Stimuli," in *Proceedings of the 17th International Conference on VLSI Design (VLSID'04)*, Mumbai, India, 2004.

[10] P. N. Variyam, S. Cherubal, and A. Chatterjee, "Prediction of Analog Performance Parameters Using Fast Transient Testing," *IEEE Transactions on Computer-Aided Design of Integrated Circuits,* vol. 21, no. 3, pp. 349-361, March 2002.

[11] R. Voorakaranam, S. Cherubal, and A. Chatterjee, "A Signature Test Framework for Rapid Production Test of RF Circuits," in *Proceedings of the Design Automation and Test in Europe*, Paris, France, 2002.

[12] A. Halder, A. Chatterjee, "Specification Based Digital Compatible Build-In Test of Embedded Analog Circuits," in *Proceedings of the 10th Asian Test Symposium*,

Kyoto, Japan, 2001.

[13] A. Banerjee, S. K. Devarakond, V. Natarajan, S. Sen, and A. Chatterjee, "Optimized Digital Compatible Pulse Sequences for Testing of RF Front End Modules," in *Proceedings of the 16th IEEE Mixed-Signals, Sensors and Systems Test Workshop (IMS3TW)*, Montepellier - La Grande Motte, France, 2010.

[14] E. S. Erdogan and S. Ozev, "A Packet Based 2x-Site Test Solution for GSM Transceivers with Limited Tester Resources," in *Proceedings of the 27th IEEE VLSI Test Symposium (VTS'09)*, Santa Cruz, CA, USA, 2009.

[15] F. G. Stremler, Introduction to Communications Systems, Third ed., Addison Wesley Publishing Company, 1990.

[16] Aeroflex-Weinschel, "Weinschel 1593 Broadband Resistive Power Splitter Datasheet," 03 04 2009. [Online]. Available: http://www.aeroflex.com/ams/weinschel/pdfiles/wmod1593.pdf.

[17] Anritsu, "Selection of Anritsu Power Meters and Sensors," Anritsu, [Online]. Available: http://www.anritsu.com/en-US/Products-Solutions/Test-Measurement/RF-Microwave/Power-Meters-and-Sensors/index.aspx. [Accessed 01 03 2012].

[18] Rohde & Schwarz, "Rohde & Schwarz Power Meters and Voltmeters Selection," Rohde & Schwarz, 2012. [Online]. Available: http://www2.rohde-schwarz.com/en/products/test_and_measurement/power_volt_meter/?ls_id=1147&&WT.mc_id=www2.rohde-schwarz.com/ad/nrp. [Accessed 01 03 2012].

[19] National Instruments, "National Instruments RF Power Meter Selection," National Instruments, 2012. [Online]. Available: http://sine.ni.com/nips/cds/view/p/lang/en/nid/208934. [Accessed 01 03 2012].

[20] Maxim, "Three Methods of Noise Figure Measurement, Application Note 2875," 21 November 2003. [Online]. Available: www.maxim-ic.com/an2875.

[21] Agilent Technologies, "Noise Figure Measurement Accuracy - The Y-Factor Method, Application Note 57-2," 5 May 2010. [Online]. Available: cp.literature.agilent.com/litweb/pdf/5952-3706E.pdf.

[22] M. A. Zeidan, "Method for Measuring Spectral Noise Densities Beyond Instrument Capability with Deterministic Confidence Level". Austin, TX, USA. Patent US7315172, 1 January 2008.

[23] D. Krafcsik, F. Ali, and S. Bishop, "Broadband, Low-Loss 5- and 6-Bit Digital Attenuators," in *Proceedings of the Microwave Symposium Digest*, Orlando, FL, USA, 1995.

[24] R. K. Setty, "Digital Step Attenuators Offer Precision and Linearity," *RF Design,* pp. 34-42, August 2005.

[25] S. Natarajan, M. A. Beuer, and S. K. Gupta, "Process Variations and Their Impact on Circuit Operation," in *Proceedings of the 1998 International Symposium on Defect and Fault Tolerance in VLSI Systems*, Austin, TX, USA, 1998.

[26] S. Tuuna, E. Nigussie, J. Isoaho, and H. Tenhunen, "Analysis of Delay Variation in Encoded On-Chip Bus Signaling under Process Variation," in *Proceedings of 21st International Conference on VLSI Design*, Hyderabad, India, 2008.

[27] Texas Instruments, "SN74LVC1G86-EP Single 2-Input Exclusive-OR Gate," July 2007. [Online]. Available: www.ti.com/lit/ds/symlink/sn74lvc1g86-ep.pdf.

[28] MA-COM, "MAATSS0002 5-Bit Digital Attenuator Specification," [Online]. Available: www.macomtech.com/datasheets/MAATSS0002.pdf.

[29] Peregrine Semiconductor, "PE43703 Product Specification," 2009. [Online]. Available: www.psemi.com/pdf/datasheets/pe43703ds.pdf.

[30] Brian C. Wadell, Transmission Line Design Handbook, Artech House Antennas and Propagation Library, 1991.

[31] National Instruments, "Extract Single Tone Information VI," June 2011. [Online]. Available: http://zone.ni.com/reference/en-XX/help/371361H-01/lvwave/extract_single_tone_info/. [Accessed 24 04 2012].

[32] National Instruments, "Scaled Time Domain Window VI," June 2011. [Online]. Available: http://zone.ni.com/reference/en-XX/help/371361H-01/lvanls/scaled_time_domain_window/. [Accessed June 2012].

[33] C. Wallenhauer, C. Technol., S. AG, B. Gottlieb, A. Kappel, T. Schwebel, J. Rucha and T. Luth, "Accurate Load Detection Based on a New Piezoelectric Drive Principle Employing Phase-Shift Measurement," *Journal of Microelectromechanical Systems,* vol. 16, no. 2, pp. 344 - 350, 10 April 2007.

[34] D. M. Purcaru, I. Purcaru, C. Gordan, E. Niculescu and S. Nedelcut, "Application of Fourier Method in Energetics, for Root-Mean-Square Value and Phase Shift Measurement," in *IEEE International Conference on Automation, Quality and Testing, Robotics*, Cluj-Napoca, 2008.

[35] S. Poujouly, B. Journet and D. Miller, "Laser Range Finder Based on Fully Digital Phase-Shift Measurement," in *Proceedings of the 16th IEEE Instrumentation and Meaurement Technology Conference*, Venice, 1999.

[36] T. Y. Wu, "The Accurate Measurement of Microwave Phase-Shift Using A Dual-Channel Heterodyne System," in *Microwave Conference, 2009. APMC 2009, Asia Pacific*, Singapore, 2009.

[37] T. Y. Wu, "Accurate Measurement of Microwave Phase-Shift from 2 to 18 GHz using Heterodyne Receiver," *IET Electronic Letters,* vol. 47, no. 14, pp. 802 - 804, 7 July 2011.

[38] T. Y. Wu, "Accurate Meaurement of Millimetre-Wave Phase-Shift from 220 to 325 GHz using Dual-Channel System," *IET Electronic Letters,* vol. 48, no. 1, pp. 31 - 33, 5 January 2012.

[39] T. Kawakami, "Microwave Attenuation and Phase-Shift Measurement Using Stepped Phase Modulation," *IEEE Transactions on Instrumentation and Measurement,* vol. 27, no. 1, pp. 33 - 38, March 1978.

[40] C. F. Augustine, "A Simple Method for Precise Phase Shift Measurement," in *G-MTT Symposium Digest*, 1965.

[41] L.-S. Yin, "A Precise Method of Phase Shift Measurement for Large Microwave System," in *Microwave Conference, 1981. 11th European*, Amsterdam, 1981.

[42] B. D. Hernandez, L. M. Rivas, L. Burtseva, O. Sergiyenko and V. Tyrsa, "Method for Phase-Shift Measurement Using Farey Fractions," in *Multiconference on Electronics and Photonics*, Guanajuato, 2006.

[43] J. Dunsmore and J. Ericsson, "A Novel Method for Measuring Phase and Group Delay of Mixers without a Reference Mixer," in *75th Microwave Measurements Conference*, Anaheim, 2010.

[44] T. H. Lee, The Design of CMOS Radio-Frequency Integrated Circuits, Second ed., Cambridge University Press, 2003.

[45] J. C. Pedro and N. B. de Carvalho, "On the Use of Multitone Techniques for Assessing RF Components' Intermodulation Distortion," *IEEE Transactions on Microwave Theory and Techniques,* vol. 47, no. 12, pp. 2393-2402, December 1999.

[46] M. A. Zeidan, G. Banerjee, R. Gharpurey, and J. A. Abraham, "Multitone Digital Signal Based Test for RF Receivers," in *Proceedings of the 28th IEEE VLSI Test Symposium (VTS'10)*, Santa Cruz, CA, USA, 2010.

[47] M. A. Zeidan, G. Banerjee, R. Gharpurey and J. A. Abraham, "Phase-Aware Multitone Digital Signal Based Test for RF Receivers," *IEEE Transactions on Circuits and Systems I (TCAS-I),* no. 99, pp. 1 - 14 (early access articles), 5 April 2012.

[48] National Instruments, "Solve Linear Equations VI," June 2011. [Online]. Available: http://zone.ni.com/reference/en-XX/help/371361H-01/gmath/solve_linear_equations/#instance2. [Accessed June 2012].

[49] G. Banerjee, M. Behera, M. A. Zeidan, R. Chen, and K. Barnett, "Analog/RF Build-In-Self-Test Subsystem for a Mobile Broadcast Video Receiver in 65-nm CMOS," *IEEE Journal of Solid-State Circuits,* vol. 46, no. 9, pp. 1998-2008, September 2011.

Vita

Mohamad A. Zeidan was born in the Lebanese capital Beirut, to Mr. Amin and Mrs. Nabila Zeidan. He graduated second-in-class from Hariri High School-II, Elementary-Math section, in 1996, and then from The American University of Beirut, where he received a B.E. degree in Computer and Communications Engineering with distinction in 2001. In summer of 2000, Mohamad did a hardware internship with National Instruments (NI) in Austin, Texas, after which he received an offer to join after graduation. He joined NI full-time in 2001, as one of the first engineers at NI to work in the high-frequency measurements group, in the R&D department, on the design and development of RF instruments. He worked on the design of NI PXI-5660 VSA, NI PXI-5670 VSG, and NI PXI-5690 Pre-amplifier. In the meantime, Mohamad worked part-time on and received a M.S.E. degree in Electrical Engineering from The University of Texas at Austin (UT-Austin) in 2005. In 2006, he joined Qualcomm Incorporated as a RF ASIC development engineer, where he worked on developing custom test benches including hardware load-boards and chip-specific characterization suites that tied system-level optimization to low-level RFIC circuit design. Mohamad resumed part-time study towards a PhD degree at UT-Austin in 2008. In late 2010, he re-joined NI to work on the design of a key high-end RF instrument that redefined RF instrumentation, the NI PXIe-5644R (www.rfredefined.com), for which the term VST was coined. Mohamad received his Doctor of Philosophy degree from UT-Austin (under the supervision of Dr. Jacob A. Abraham and Dr. Ranjit Gharpurey) in 2012.

Email: mohamad.zeidan@utexas.edu

This dissertation was typed by the author.